OLD DOMINION UNIVERSITY RESEARCH FOUNDATION

DEPARTMENT OF MECHANICAL ENGINEERING AND MECHANICS
SCHOOL OF ENGINEERING
OLD DOMINION UNIVERSITY
NORFOLK, VIRGINIA

AEROTHERMODYNAMIC ENVIRONMENT OF A TITAN AEROCAPTURE VEHICLE

By

S. N. Tiwari, Principal Investigator

and

H. Chow

Final Report
For the period November 4, 1980 - November 3, 1981

Prepared for the
National Aeronautics and Space Administration
Langley Research Center
Norfolk, Virginia

Under
Research Grant NAG1-120
J. N. Moss, Technical Monitor
Space Systems Division

January 1982

DEPARTMENT OF MECHANICAL ENGINEERING AND MECHANICS
SCHOOL OF ENGINEERING
OLD DOMINION UNIVERSITY
NORFOLK, VIRGINIA

AEROTHERMODYNAMIC ENVIRONMENT OF A TITAN AEROCAPTURE VEHICLE

By

S. N. Tiwari, Principal Investigator

and

H. Chow

Final Report
For the period November 4, 1980 - November 3, 1981

Prepared for the
National Aeronautics and Space Administration
Langley Research Center
Norfolk, Virginia 23665

Under
Research Grant NAG1-120
J. N. Moss, Technical Monitor
Space Systems Division

Submitted by the
Old Dominion University Research Foundation
P.O. Box 6369
Norfolk, Virginia 23508-0369

January 1982

PRECEDING PAGE BLANK NOT FILMED

TABLE OF CONTENTS

LIST OF TABLES

LIST OF FIGURES

PRECEDING PAGE BLANK NOT FILMED

FOREWORD

This report summarizes the work completed during the period November 4, 1980 to November 3, 1981 on the research project titled "Analysis of Aerothermodynamic Environment of an Aerocapture Vehicle." The work was supported by the NASA/Langley Research Center (Aerothermodynamics Branch of the Space Systems Division) through research grant NAG1-120. The grant was monitored by Dr. James N. Moss of the Space System Division.

AEROTHERMODYNAMIC ENVIRONMENT OF A TITAN AEROCAPTURE VEHICLE

By

S. N. Tiwari[1] and H. Chow[2]

SUMMARY

The extent of convective and radiative heating for a Titan entry vehicle is investigated. The flow in the shock layer is assumed to be axisymmetric, steady, viscous, and compressible. It is further assumed that the gas is in chemical and local thermodynamic equilibrium and tangent slab approximation is used for the radiative transport. The effect of slip boundary conditions on the body surface and at the shock wave are included in the analysis of high-altitude entry conditions.

The implicit finite-difference technique is used to solve the viscous shock-layer equations for a 45-degree sphere cone at zero angle of attack. Different compositions for the Titan's N_2 + CH_4 atmosphere are assumed, and results are obtained for the entry conditions specified by the Jet Propulsion Laboratory. The results indicate that the heating rate, in general, increases with increasing N_2 concentration. Both convective and radiative heating increase with increasing initial entry velocity. The radiative heating increases, but the convective heating decreases with increasing body nose radius. The amount of CN concentration in the shock-layer gas determines the extent of radiative heating to the body. Radiative heating will be important for free-stream gas composition with N_2 concentration between 50% and 90%. For the atmospheric compositions of 99.5% N_2 + 0.5% CH_4 and 98% N_2 + 2% CH_4, the radiative heating hear the stagnation region is insignificant in comparison to the convective heating. The results indicate that the effect of the slip conditions is important when the altitudes are higher than 402.595 km. Therefore, both the body and shock slip conditions should be included in analyzing the aerothermal environment of the Titan aerocapture vehicle at higher entry altitudes.

[1]Eminent Professor, Department of Mechanical Engineering and Mechanics, Old Dominion University, Norfolk, Virginia 23508.

[2]Graduate Research Assistant, Department of Mechanical Engineering and Mechanics, Old Dominion University, Norfolk, Virginia 23508.

LIST OF SYMBOLS

B_ν	Planck blackbody radiative function, erg/cm^2
C_f	skin friction coefficient
C_i	mass fraction of species i, ρ_i/ρ
C_ℓ	mass fraction of element ℓ
C_p	equilibrium specific heat mixture, $\sum_i C_i\, C_{p,i}$
$C_{p,i}$	specific heat of species i, $C^*_{p,i}/C^*_{p,\infty}$
D_{ij}	multicomponent diffusion coefficients
$\underline{D}_{ij}$	binary diffusion coefficients
F^*	free energy of mixture
F^*_i	free energy of species i
H	total enthalpy of mixture, H^*/V^{*2}_∞
h	enthalpy of mixture, $\sum_i C_i\, h_i$ (also Planck constant)
h_i	enthalpy of species i, h^*_i/V^{*2}_∞
I_ν	specific intensity, erg/cm^2
J_i	diffusion mass flux of species i, $J^*_i\, R^*_N/\mu^*_{ref}$
J_ℓ	diffusion mass flux of species ℓ
K	thermal conductivity of mixture, $K^*/\mu^*_{ref}\, C^*_{p,\infty}$
K^*_i	thermal conductivity of species i
L/D	lift/drag
Le_{ij}	Lewis number, $\rho^*\, C^*_p\, D_{ij}/K^*$

LIST OF SYMBOLS (Cont'd)

Le	binary Lewis number, $\rho^* C_p^* \underline{D}_{ij}/K^*$
M^*	molecular weight of species i
N	number of reacting species
n	coordinate measured normal to the body, n^*/R_N^*
P	pressure, $P^*/(\rho_\infty^* V_\infty^{*2})$
Pr	Prandtl number, $\mu^* C_p^*/K^*$
$q_{c,w}$	wall heat-transfer rate, $q^*/(\rho_\infty^* V_\infty^{*3})$
q_r	net radiant heat flux, $q_r^*/(q_\infty^* V_\infty^{*3})$
q_r^+	adiative heat flux toward shock
q_r^-	radiative heat flux toward body
R^*	universal gas constant
r	radius measured from axis of symmetry to a point on the body surface, r^*/R_N^*
R_b	radius of the body
Re	Reynolds number, $\rho_\infty^* V_\infty^* R_N/\mu_\infty^*$
R_N^*	body nose radius
S	coordinate along the body surface, S^*/R_N^*
St	Stanton number, $q_{c,n}/(H_\infty - H_w)$
T	temperature, $T^*/V_\infty^{*2}/C_{p\infty}^*)$
t	optical coordinate
V_∞^*	free-stream velocity
U_E	initial entry velocity

LIST OF SYMBOLS (Cont'd)

u	velocity component tangent to body surface, u^*/V_∞^*
v	velocity component normal to body surface, v^*/V_∞^*
x_i	mole fraction of species i
α	shock angle
α_ν	extinction coefficient
β	ballistic coefficient, $W/(C_D A)$
γ	inertial entry angle
$\delta_{i\ell}$	number of atoms of ℓth element in species i
ϵ	Reynolds number parameter, $[\mu_{ref}^*/(\rho_\infty^* V_\infty^* R_N)]^{1/2}$
ϵ_ν	surface emittance
η	transformed n coordinate, n/n_s
ϕ	body angle
κ	body curvature, κ^*/R^*_N
κ_ν	spectral absorption coefficient
μ	viscosity of mixture, μ^*/μ_{ref}^*
μ_{ref}^*	reference viscosity
ξ	coordinate measured along the body surface, $\xi = S$
ρ	density of mixture, ρ^*/ρ_∞^*
τ	optical thickness
ν	frequency

<u>Subscripts</u>

i	ith species

LIST OF SYMBOLS (Concl'd)

s	shock value
∞	free-stream condition
$*$	dimensional quantity
$'$	total differential
$''$	shock-oriented velocity components

1. INTRODUCTION

The importance of aerobraking and aerocapture for planetary missions has been emphasized in the recent years. It has been pointed out that aerobraking for circularizing orbits and aerocapture could more than double science payload on some planetary spacecraft and make possible new missions, such as a Saturn orbiter dual probe mission, where the probes would enter the atmospheres of both Saturn and its satellite Titan.

The aerobraking technique uses the aerodynamic drag of the spacecraft during successive passes through the upper atmosphere to circularize a highly elliptical orbit. The aerocapture concept, on the other hand, uses the aerodynamic drag to place the spacecraft in a closed planetary orbit from a hyperbolic flyby trajectory in a single atmospheric entry pass. It is accomplished through an aerodynamically controlled atmospheric entry during which the vehicle's in-plane lift-to-drag ratio is varied to maintain a constant drag. The aerocapture not only offers significant gains in payload and choice of orbits, but also significantly decreases interplanetary cruise time; and this concept completely eliminates the fuel-costly retropropulsion module for planetary orbiter mission.

An aerocapture mission is possible for any atmosphere-bearing celestial body. The feasibility of using aerocapture vehicles has been emphasized recently for both inner and outer planetary missions (refs. 1-6). Originally, the aerocapture study was undertaken for a Mars sample return mission (refs. 3,6). The aerocapture missions under present consideration are the Mars surface sample return (MSSR), Saturn orbiter dual probe (SO2P), and Titan orbiter (TO) missions.

For missions to outer planets, use of the aerocapture concept in a convenient atmosphere-bearing satellite of the target planet has been emphasized. It has been proposed to use the atmosphere of Titan for braking into a Saturn orbit (ref. 4). The use of Titan's atmosphere would minimize the entry speed requirement for aerocapture and this, in turn, would minimize the thermal protection requirements of the aerocapture vehicle. The Titan's aerocapture concept (for Saturn orbital mission) is expected to cut the interplanetary cruise travel time to Saturn from 8 to 3.5 years. A Titan orbiter mission using anything other than aerocapture is presently impractical (ref. 4). For Titan's aerocapture mission, the need for high-performance entry vehicle geometries and high-performance thermal protection systems has been stressed (refs. 4,5). In partial support of this need, it is essential to provide a complete analysis of the aerothermodynamic environment of the Titan aerocapture vehicle.

The optimum lift/drag (L/D) ratio required for the aerocapture control accuracy is 1.0 to 2.0. The combination of high volumetric efficiency, low ballistic coefficient, and aerocapture control accuracy has led to choosing biconics as the entry vehicle geometry for the aerocapture missions (ref. 4).

In order to investigate the aerothermodynamic environment of a Titan aerocapture vehicle, it is essential to know the composition of Titan's atmosphere. Prior to the Voyager 1 mission (November 1980), there was a controversy regarding Titan's atmospheric composition. The problem is still not completely resolved, but it is now evident (ref. 7) that Titan, the largest moon in the solar system, is wrapped essentially in a dense atmosphere of nitrogen vapors (rather than methane, the best guess before Voyager 1). Thus, a realistic composition for Titan's atmosphere would include a fairly high concentration of nitrogen.

The main objective of this study is to determine the extent of convective and radiative heating to the aerocapture vehicle under different entry conditions. This essentially can be accomplished by assessing the heating rate in stagnation and windward regions of an equivalent body. The equivalent body configuration considered for this study is a 45-degree sphere cone at zero angle of attack. Different compositions for the Titan's $N_2 + CH_4$

atmosphere have been asumed, and the study has been conducted for various entry trajectories suggested by the Jet Propulsion Laboratory (JPL). Specific obectives of this study, therefore, are as follows:

1. For a given free-stream atmospheric composition, determine the important chemical species in the shock-layer gas for different pressure and temperature conditions.

2. Investigate the effect of the free-stream gas composition on the stagnation-point shock temperature and convective and radiative heating rates.

3. Investigate the effect of different entry velocities on the stagnation-point shock temperature and convective and radiative heating rates.

4. Determine the effect of body nose radius on the stagnation-point convective and radiative heating rates.

5. Determine the variation of the shock temperature and enthalpy and convective and radiative heating rates along the body for different free-stream atmospheric compositions.

6. Investigate the influence of CN concentration in the shock layer on the convective and radiative heating rates along the body.

7. Investigate the effect of shock as well as body slip conditions on the entire shock-layer flow phenomena and determine the extent of convective and radiative heating rates under these conditions.

Basic formulation of the entire problem is presented in Chapter 2, and boundary conditions are given in Chapter 3. The information on the thermodynamic and transport properties are given in chapter 4, and Chapter 5 discusses the chemical compositons. The radiative transport model for this study is described in Chapter 6. The physical conditions and data sources are given in Chapter 7. The method of solution is duscussed in Chapter 8, and all results are presented in Chapter 9.

2. BASIC FORMULATION

As discussed in the Introduction, the aerocapture technique transfers the spacecraft into a closed, stable orbit from a hyperbolic flyby trajectory in a single pass (fig. 1). This requires a high level of technology, but offers a significant gain in the payload and choice of orbits. The Titan aerocapture concept for the Saturn orbital mission is shown in figure 2. For such missions, use of the biconics as the entry vehicle configuration (fig. 3) has been suggested (ref. 4). The preliminary assessment of the aerothermodynamic environment of an aerocapture vehicle can be made by investigating the flow field around an equivalent body. The equivalent body configuration considered for this study is a 45-degree sphere cone at zero angle of attack.

The physical model and coordinate system considered for the equivalent body are shown in figure 4. The flow conditions for a radiating and reacting multicomponent gas mixture in the shock layer are considered axisymmetric, steady, viscous, and compressible. It is further assumed that the gas is in chemical and local thermodynamic equilibrium and the tangent slab approximation is used for the radiative transport.

The conservation equations for a reacting multicomponent gas mixture can be found in the literature (refs. 8,9). The viscous shock-layer equations that are valid uniformly throughout the shock-layer region are formulated in exactly the same manner as the viscous shock-layer equations for a one-component gas presented by Davis (ref. 10). In order to obtain the viscous shock-layer equations, the conservation equations are written in a boundary-layer coordinate system as shown in figure 4 and are nondimensionalized by variables which are of order one in the boundary layer. The same set of equations is then written in variables which are of order one in the inviscid region outside the boundary layer. Terms are kept in each set of equations up to second order in the inverse square root of Reynolds number. The two sets of equations are combined so that terms up to second order in both the inner and outer regions are retained. In this way, a set of

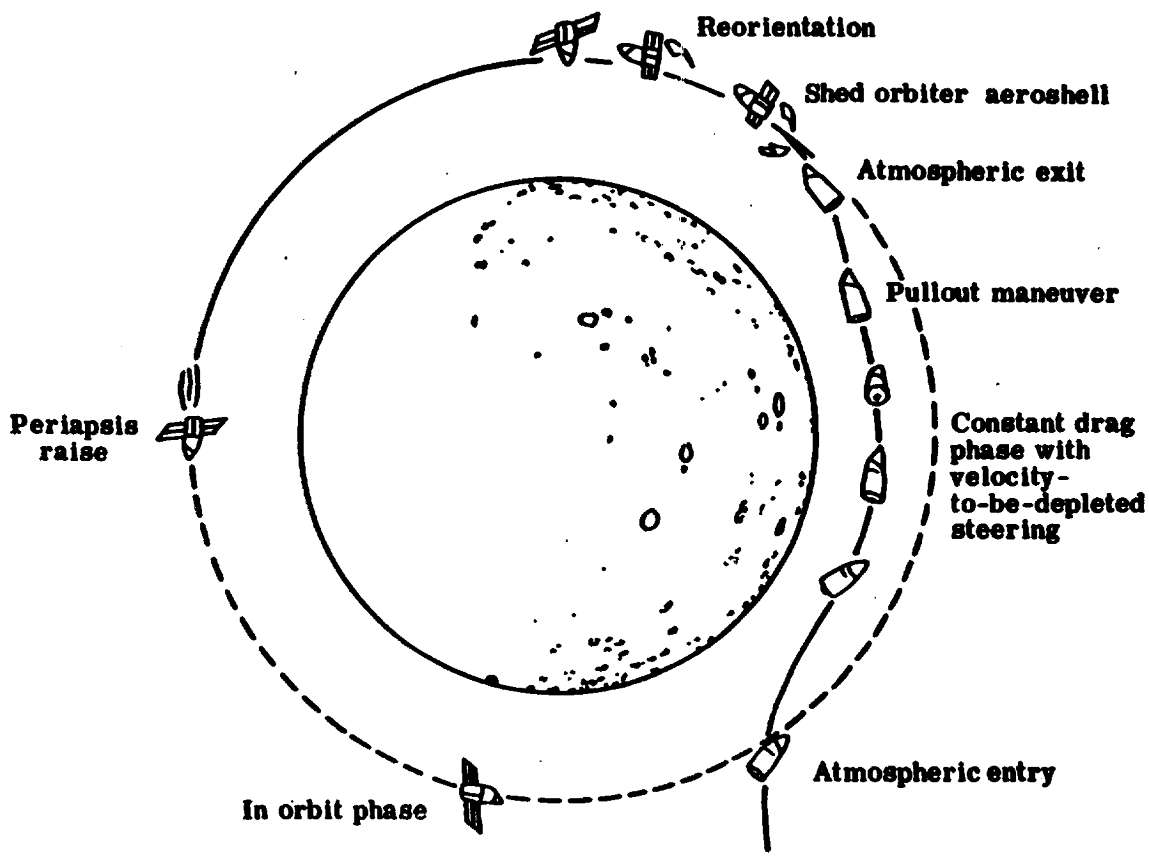

Figure 1. Aerocapture trajectory.

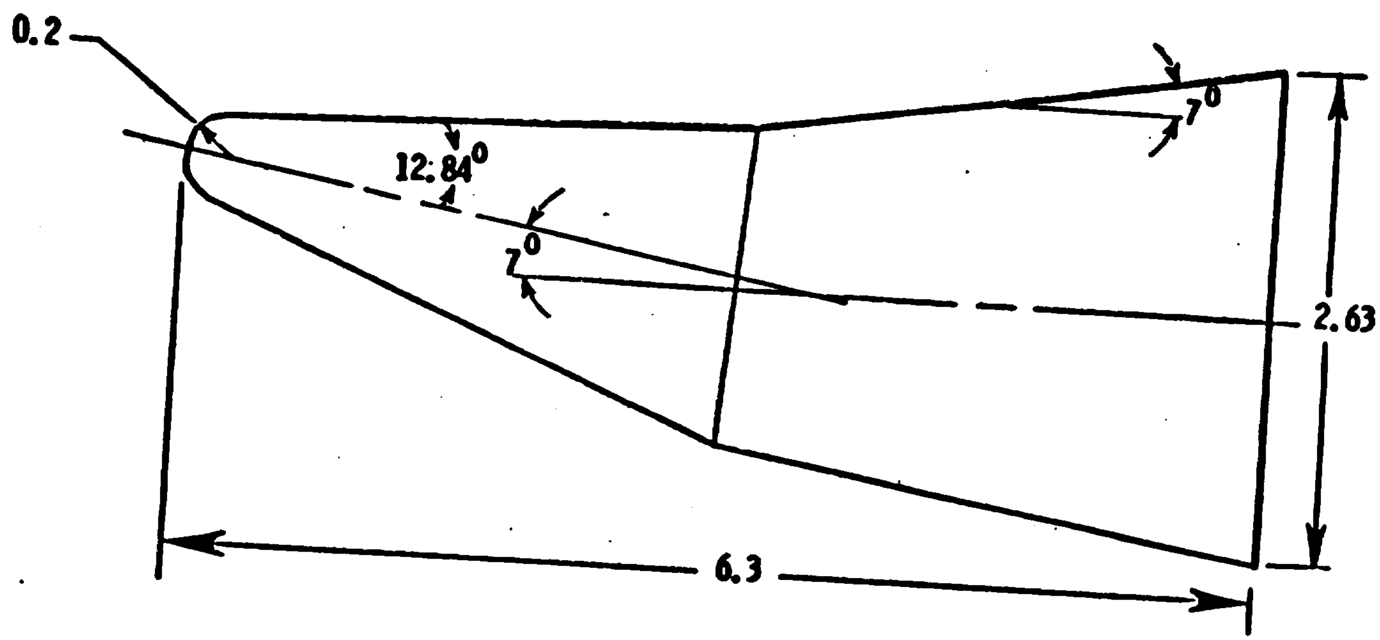

Figure 2. Titan aerocapture vehicle configuration.

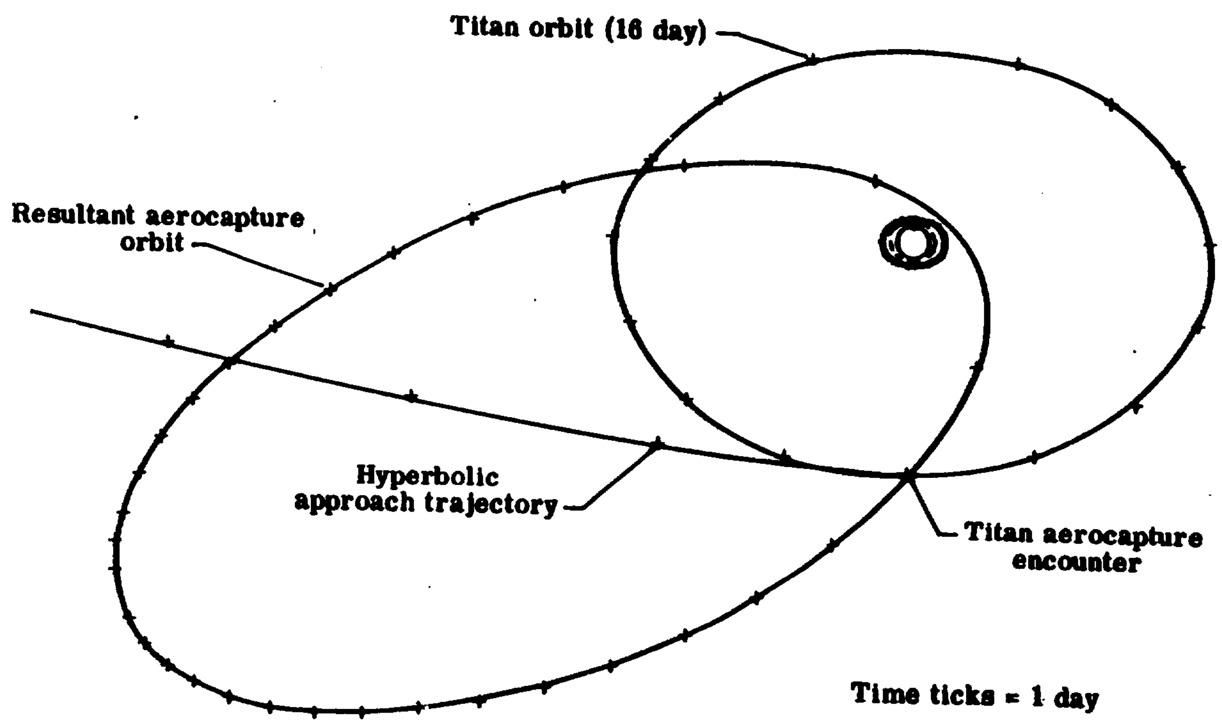

Figure 3. Titan aerocapture for Saturn orbit.

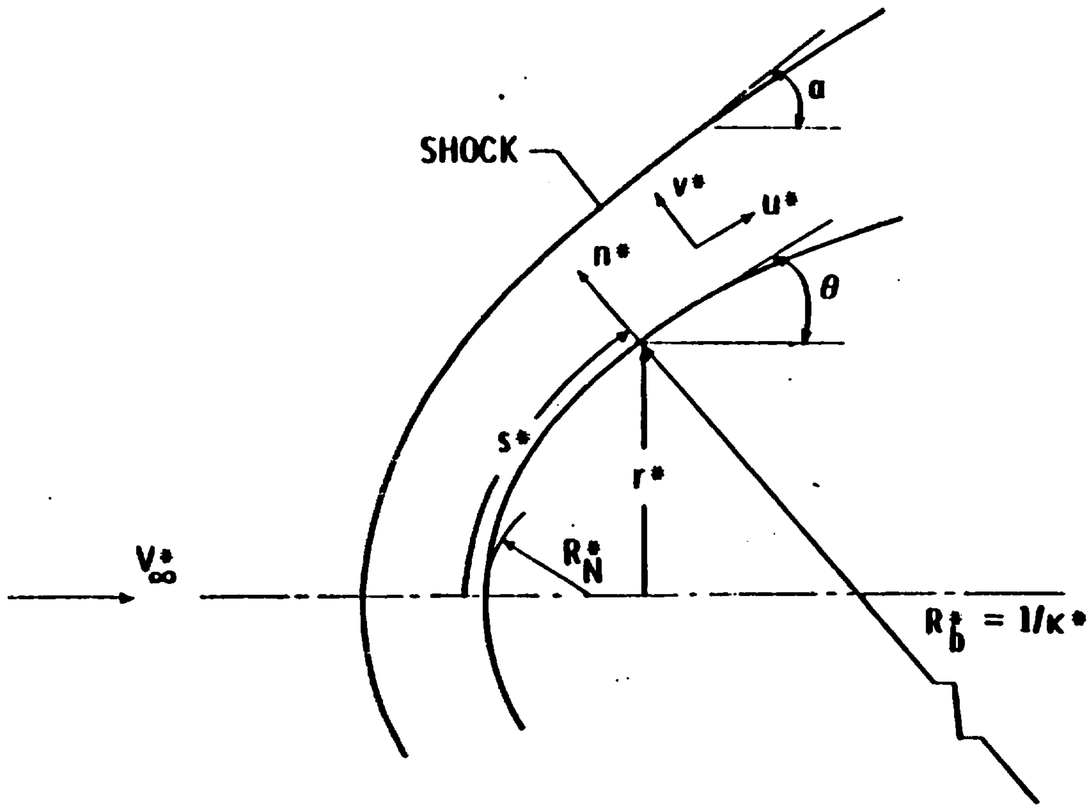

Figure 4. Coordinate system.

equations uniformly valid to second order in the entire shock layer is obtained. The nondimensional form of the viscous shock-layer equations that are applicable in the present case can be written as (refs. 11, 12):

Continuity:

$$\left(\frac{\partial}{\partial s}\right) \zeta\rho\mu + \left(\frac{\partial}{\partial n}\right)\left(\Gamma\zeta\rho v\right) = 0 \tag{2.1}$$

s-momentum:

$$\rho\left[\left(\frac{u}{\Gamma}\right)\left(\frac{\partial u}{\partial s}\right) + v\left(\frac{\partial u}{\partial n}\right) + \frac{uv\kappa}{\Gamma} + \Gamma^{-1}\left(\frac{\partial p}{\partial s}\right)\right]$$

$$= \varepsilon^2\left[\left(\frac{\partial}{n}\right)(\mu\psi) + \mu\left(\frac{2\kappa}{\Gamma} + \frac{\cos\theta}{\zeta}\right) + \psi\right] \tag{2.2}$$

n-momentum:

$$\rho\left[\left(\frac{u}{\Gamma}\right)\left(\frac{\partial v}{\partial s}\right) + v\left(\frac{\partial v}{\partial n}\right) - \frac{u^2\kappa}{\Gamma}\right] + \frac{\partial p}{\partial n} = 0 \tag{2.3}$$

Energy

$$\rho\ \frac{u}{\Gamma}\left[\left(\frac{\partial H}{\partial s}\right) + v\left(\frac{\partial H}{\partial n}\right)\right] - v\left(\frac{\partial p}{\partial n}\right) + \frac{\rho\kappa u^2 v}{\Gamma}$$

$$= \varepsilon^2\left[\frac{\partial\phi}{\partial n} + \left(\frac{\kappa}{\Gamma} + \frac{\cos\theta}{\zeta}\right)\phi\right] - \mathrm{div}\ \underset{\sim}{q}_r \tag{2.4}$$

Species continuity:

$$\rho\left[\left(\frac{u}{\Gamma}\right)\left(\frac{\partial C_i}{\partial s}\right) + v\left(\frac{\partial C_i}{\partial n}\right)\right] = -\left\{\left(\frac{\varepsilon^2}{\Gamma\zeta}\right)\left(\frac{\partial}{\partial n}\right)[\Gamma\zeta J_i]\right\} \tag{2.5}$$

State:

$$P = \rho T\left[\frac{R^*}{\left(\bar{M}^*\ C^*_{p,\infty}\right)}\right] \tag{2.6}$$

where

$$\Gamma = 1 + n\,\kappa, \zeta = r + n \cos\theta \tag{2.7a}$$

$$\varepsilon = \frac{\mu^*_{ref}}{\left(\rho^*_\infty V^*_\infty R_N\right)^{1/2}}, \quad \psi = \frac{\partial u}{\partial n} - \frac{u\kappa}{\Gamma} \tag{2.7b}$$

$$\phi = \left(\frac{\mu}{Pr}\right)\left[\frac{\partial H}{\partial n} - \sum_{i=1}^{N} h_i \left(\frac{\partial C_i}{\partial n}\right) - \left(\frac{Pr}{\mu}\right)\sum_{i=1}^{N} h_i J_i \right.$$

$$\left. + (Pr - 1)\mu\left(\frac{\partial u}{\partial n}\right) - \frac{Pr\kappa u^2}{\Gamma}\right] \tag{2.7c}$$

$$H = h + \frac{u^2}{2} \tag{2.7d}$$

$$\overline{M}^* = \frac{1}{\sum\limits_{i}^{N} \left(\frac{C_i}{M^*_i}\right)} \tag{2.7e}$$

The terms used to nondimensionalize the above equations are defined as:

$u^* = uV^*_\infty$ $\qquad$ $v^* = vV^*_\infty$

$T^* = \dfrac{TV^{*2}_\infty}{C^*_{p,\infty}}$ $\qquad$ $p^* = p\,\rho_\infty^*\,V^{*\,2}_\infty$

$$\rho^* = \rho\, \rho^*_\infty \qquad \mu^* = \mu \mu^*_{ref}$$

$$K^* = K \mu^*_{ref} C^*_p \qquad C^*_p = C_p C^*_{p,\infty}$$

$$h^* = h V^{*2}_\infty \qquad w^*_i = w^*_i * \frac{V^*_\infty}{R^*_N}$$

$$J^*_i = \frac{J_i \mu^*_{ref}}{R_N} \qquad s^* = s R^*_N$$

$$n^* = n R_N^* \qquad r^* = r R^*_N$$

$$q_r = \frac{q_r}{\rho^*_\infty V^{*3}_\infty} \qquad K^* = \kappa R^*_N$$

$$Pr = \frac{C^*_p \mu^*}{K^*} \qquad Le_{ij} = \rho^* C_p^* \frac{D_{ij}}{K^*} \tag{2.8}$$

The set of governing equations presented above [eqs. (2.8)] has a hyperbolic-parabolic nature, where the hyperbolic nature comes from the normal equation. If the shock layer is assumed to be thin, then the normal momentum equation can be expressed as

$$\frac{\rho u^2 \kappa}{\Gamma} = \frac{\partial p}{\partial n} \tag{2.9}$$

When equation (2.3) is replaced with equation (2.9), then the resulting set of equations is parabolic. These equations can, therefore, be solved by using numerical methods similar to those used in solving boundary-layer problems (refs. 10,13). After an initial iteration using equation (2.9), the final flow-field solution is obtained by replacing equation (2.9) with equation (2.3); thus, the thin shock-layer approximation is removed.

Since there are no nuclear reactions, the elemental mass fractions remain fixed and unchanged during chemical reactions. The relation between the elemental and species mass fractions is given by

$$C_\ell = \sum_{i=1}^{N} \delta_{i\ell} \left(\frac{M_\ell^*}{M_i^*}\right) C_i \tag{2.10}$$

The elemental continuity equations for the elements can be obtained by multiplying equation (2.5) by $\delta_{i\ell}\left(\frac{M_\ell^*}{M_i^*}\right)$ and summing over i. The resulting elemental continuity equation is

$$\rho \left[\left(\frac{u}{\Gamma}\right)\left(\frac{\partial C_\ell}{\partial s}\right) + v\left(\frac{\partial C_\ell}{\partial n}\right)\right] = -\left(\frac{\varepsilon^2}{\Gamma \zeta}\right)\left\{\left(\frac{\partial}{\partial n}\right)\left[\Gamma \zeta J_\ell\right]\right\} \tag{2.11}$$

where

$$J_\ell = \sum_{i=1}^{N} \delta_{i\ell}\left(\frac{M_\ell^*}{M_i^*}\right) J_i \tag{2.12}$$

Use of the elemental mass fraction reduces the number of equations to be solved. Therefore, equation (2.5) is replaced with (2.11) for equilibrium flow.

The mas flux due to concentration gradients can be written as

$$J_i = -\left(\frac{\mu}{Pr}\right) \sum_{K=1}^{N} \overline{b}_{iK}\left(\frac{\partial C_K}{\partial n}\right) \tag{2.13}$$

where

$$\bar{b}_{iK} = \begin{cases} Le_i, & i = K \\ Le_i - \left\{ \left(\frac{M_i}{M}\right) Le_{iK} + 1 - \left(\frac{M_i}{M_K}\right) \sum_{j=1}^{N} Le_{ij} C_j \right\}, & i \neq K \end{cases} \tag{2.14}$$

and

$$Le_i = \frac{\sum_{\substack{j=1 \\ j \neq 1}}^{N} \left(\frac{C_j}{M_j}\right)}{\sum_{\substack{j=1 \\ j \neq i}}^{N} \frac{C_j}{M_j L_{ij}}} \tag{2.15}$$

The relative mass flux for the elements can be written as

$$J_\ell = -\left(\frac{\mu}{Pr}\right) \left[L \left(\frac{\partial C_\ell}{\partial n}\right) + \sum_{k=1}^{N} B_{\ell K} \left(\frac{\partial C_k}{\partial n}\right) \right] \tag{2.16}$$

where

$$B_{\ell K} = \sum_{i=1}^{N} \delta_{i\ell} \left(\frac{M^*_\ell}{M^*_i}\right) \Delta b_{iK} \tag{2.17}$$

$$\Delta b_{iK} = \left\{ \begin{array}{ll} Le_i - L, & i = k \\ \bar{b}_{iK}, & i \neq K \end{array} \right\} \tag{2.18}$$

and L is an arbitrary constant. For binary diffusion, equations (2.13) and (2.16) reduce, respectively, to

$$J_i = -\left(\frac{\mu}{Pr}\right) Le \left(\frac{\partial C_i}{\partial n}\right) \tag{2.19}$$

$$J_\ell = -\left(\frac{\mu}{Pr}\right) Le \left(\frac{\partial C_\ell}{\partial n}\right) \tag{2.20}$$

The heat transferred to the wall due to conduction and diffusion is referred to here as the convective heat flux and is given by the relation (ref. 13):

$$q_{c,w} = -\epsilon^2 \left[K\left(\frac{\partial T}{\partial n}\right) + \left(\mu \frac{Le}{Pr}\right) \sum_{i=1}^{N} \frac{\partial C_i}{\partial n} h_i\right] \tag{2.21}$$

In this study, the Lewis and Prandtl numbers are taken to be 1.1 and 0.72, respectively.

The convective heat transfer is also described by a dimensionless parameter called Stanton number. The Stanton number is given by

$$St = \frac{q_{c,w}}{\left(H_\infty - H_w\right)} \tag{2.22}$$

The skin friction coefficient for such flows is given by

$$C_f = 2\epsilon^2 \left[\mu \left(\frac{\partial u}{\partial n}\right)\right]_w \tag{2.23}$$

In order to solve the preceding set of governing equations, it is essential to specify appropriate boundary conditions at the body surface and at the shock. These are discussed in detail in the next chapter.

3. BOUNDARY CONDITIONS

3.1. Introduction

Specific boundary conditions used at the body surface and the bow shock are presented here. Since both the slip and no-slip conditions have been used in this study, they will be discussed separately in this chapter.

3.2. No-Slip Boundary Conditions

At the body surface (wall), no velocity slip and no temperature jump are assumed. Consequently the velocities at the surface are

$$v = 0 \tag{3.1}$$

$$u = 0 \tag{3.2}$$

The wall temperature for this study is specified as

$$T_w = \text{constant} \tag{3.3}$$

The surface total enthalpy is given as

$$H = \sum_{i=1}^{N} h_i C_i \tag{3.4}$$

The Rankine-Hugoniot relations are used to determine the flow properties immediately behind the shock. The nondimensional shock relations are as follows (refs. 10-13):

Continuity:

$$\rho_s v''_s = -\sin\alpha \tag{3.5}$$

Momentum:

$$u''_s = \cos \alpha \tag{3.6}$$

$$p_s = \frac{1}{\gamma_\infty M_\infty^2} + \sin^2\alpha \quad 1 - \frac{1}{\rho_s} \tag{3.7}$$

Energy:

$$h_s = \frac{1}{M_\infty^2 (\gamma_\infty - 1)} + \frac{\sin^2\alpha}{2} \quad 1 - \frac{1}{\rho_s^{\,2}} \tag{3.8}$$

State:

$$p_s = \frac{\rho_s T_s R^*}{\bar{M}^*_s C^*_{\rho,\infty}} \tag{3.9}$$

Enthalpy:

$$h_s = \sum_{i=1}^{N} h_i C_i \tag{3.10}$$

where α is shown in figure 4 and u''_s and v''_s are velocity components expressed in a shock-oriented coordinate system. The transformations used to express u''_s and v''_s in terms of the body-oriented coordinate system u_s and v_s are

$$u_s = u''_s \sin(\alpha + \beta) + v''_s \cos(\alpha + \beta) \tag{3.11}$$

and

$$v_s = -u''_s \cos(\alpha + \beta) + v''_s \sin(\alpha + \beta) \tag{3.12}$$

where the angle β is indicated in figure 4.

3.3. Slip Boundary Conditions

In low Reynolds number hypersonic flows, such as high-altitude or low-density flows, the velocity and temperature of the wall are no longer the same as that of the gas immediately adjacent to the wall; these phenomena are referred to as the velocity slip and temperature jump, respectively. The slip flow boundary conditions have been derived by various investigations (refs. 14-17). Shidlovskiy (ref. 14) has shown that at the body surface the velocity slip and temperature jump conditions are of the same order as the Knudsen number. The Knudsen number K_n is defined as the ratio of the particle's mean free path ℓ and the characteristic dimension L of the body. These boundary conditions assume an impermeable surface and zero macroscopic velocity normal to the surface. They also assume that the mean free path ℓ, although small, is large enough so that there is no interaction between incident and reflected molecules at the surface. Thus, for the transitional range, in order to be consistent with the Navier-Stokes equations of motion, a linear relation between the conditions at the wall and flow should be assumed. That this can be done is a semi-macroscopic argument which leads to simple expressions for the velocity slip and temperature jump as (refs. 14, 17):

$$u = \varepsilon^2 A_1 \left(\frac{\mu}{p}\right)\left(\frac{p}{\rho}\right)^{1/2}\left(\frac{\partial u}{\partial n}\right) \tag{3.13}$$

$$v = 0 \tag{3.14}$$

$$T = T_w + \varepsilon^2 A_2 \left(\frac{u}{p}\right)\left(\frac{p}{\rho}\right)^{1/2}\left(\frac{\partial T}{\partial n}\right) \tag{3.15a}$$

$$h = h_w + \varepsilon^2 A_2 \left(\frac{\mu}{p}\right)\left(\frac{p}{\rho}\right)^{1/2}\left(\frac{\partial h}{\partial n}\right) \tag{3.15b}$$

where A_1 and A_2 are constants and are given by

$$A_1 = [(2 - \sigma_1)/\sigma_1]\ \left(\frac{\pi}{2}\right)^{1/2}$$

$$A_2 = [(2 - \sigma_2)/\sigma_2]\ \left(\frac{15}{8}\right)\left(\frac{\pi}{2}\right)^{1/2}$$

The terms σ_1 and σ_2 are slip and thermal accommodation coefficients, respectively, and are dependent on the nature of the surface and fluid. However, in actual flight conditions, both σ_1 and σ_2 are expected to be 1.

The boundary conditions used at the shock are the modified Rankine-Hugoniot or "shock slip" conditions, and these are written as (refs. 10, 13):

$$\rho_s v''_s = -\sin\alpha \tag{3.16}$$

$$u''_s = \cos\alpha - \left(\frac{\varepsilon^2\mu_s}{\sin\alpha}\right)\left(\frac{\partial u''_s}{\partial n}\right) \tag{3.17}$$

$$p_s = p_\infty + \sin^2\alpha\left(1 - \frac{1}{\rho_s}\right) \tag{3.18}$$

$$h_s = h_\infty - \left(\frac{\varepsilon^2\mu_s}{Pr\sin\alpha}\right)\left(\frac{\partial h}{\partial n}\right) + \frac{1}{2}[u''_s - \cos\alpha)^2 + \sin^2\alpha - v''^2_s] \tag{3.19}$$

$$u''_s\sin(\alpha + \beta) + v''_s\cos(\alpha + \beta) = u_s \tag{3.20}$$

$$-u''_s\cos(\alpha + \beta) + v''_s\sin(\alpha + \beta) = v_s \tag{3.21}$$

As mentioned above, slip boundary conditions are used in investigating the shock-layer flow phenomena at relatively high entry altitudes.

4. THERMODYNAMIC AND TRANSPORT PROPERTIES

Thermodynamic properties for specific heat, enthalpy, and free energy and transport properties for viscosity, thermal conductivity, and diffusion coefficients are required for each species considered. Since the multicomponent gas mixtures are considered to be mixtures of thermally perfect gases, the thermodynamic and transport properties for each species are calculated by using the local static temperature. The general expressions for total enthalpy, specific enthalpy, and specific heat at constant pressure are given, respectively, by

$$H = h + \frac{u^2}{2} \tag{4.1}$$

$$h = \sum_{i=1}^{N} h_i C_i \tag{4.2}$$

$$C_p = \sum_{i=1}^{N} C_i C_{p,i} \tag{4.3}$$

For each species, the values for the thermodynamic properties, as a function of temperature, are obtained by using polynomial curve fits. The following polynomial equations are used:

Specific heat:

$$\frac{C^*_{p,i}}{R^*} = a_1 + a_2 T^* + a_3 T^{*2} + a_4 T^{*2} + a_5 T^{*4} \tag{4.4}$$

Enthalpy:

$$\frac{h^*_i}{R^* T^*} = a_1 + \frac{a_2 T^*}{2} + \frac{a_3 T^{*2}}{3} + \frac{a_4 T^{*3}}{4} + \frac{a_5 T^{*4}}{5} + \frac{a_6}{T^*} \tag{4.5}$$

Free energy:

$$\frac{F_i^{*o}}{R^*T^*} = a_1(1 - \log_e T^*) - \frac{a_2T^*}{2} - \frac{a_3T^{*2}}{6} - \frac{a_4T^{*3}}{12}$$

$$- \frac{a_5T^{*4}}{20} + \frac{a_6}{T^*} - a_7 \tag{4.6}$$

where F_i^{*0} is the free energy of species at one atmospheric pressure. The development of these curve fits and the values of polynomial constants a_1 to a_7 are given in table 1 and are available in reference 18.

For the mixture, viscosity and thermal conductivity are obtained by using the semi-empirical formula of Wilke (ref. 8) as

$$\mu = \sum_{i=1}^{N} \left[\frac{x_i \mu_i}{\left(\sum_{j=1}^{N} x_j \phi_{ij} \right)} \right] \tag{4.7}$$

$$K = \sum_{i=1}^{N} \left[\frac{x_i K_i}{\left(\sum_{j=1}^{N} x_j \phi_{ij} \right)} \right] \tag{4.8}$$

where

$$\phi_{ij} = \frac{\left[1 + \left(\mu_i/\mu_j\right)^{1/2} \left(M_j/M_i\right)^{1/4}\right]^2}{\left\{\sqrt{8}\left[1 + M_i/M_j\right]\right\}^{1/2}} \tag{4.9}$$

The general relations for the viscosity and the thermal conductivity are given as

$$\mu_i = b_1 + b_2\, T^* + b_3\, T^{*2} \tag{4.10}$$

$$K_i = C_1 + C_2 T^*$$ (4.11)

The coefficients b_1, b_3, C_1, and C_2 for different species used in this study are given in table 2, where the value of T^* is in degrees K.

5. CHEMICAL COMPOSITION

Analyses of chemically reacting flows are usually simplified by assuming the chemical equilibrium behavior of the gas mixture. In this study, the chemical reactions are confined to a system of carbon, hydrogen, and nitrogen. The Aerotherm Chemical Equilibrium (ACE) computer program was used to determine various chemical species under different free-stream atmospheric compositions.

At the initiation of this study, the atmospheric conditions of Titan were not defined clearly. Therefore, different atmospheric compostions were assumed for a parametric study. Voyager 1 data reveals that Titan's atmosphere primarily consists of nitrogen molecules (ref. 7). Thus, a realistic case would be to assume a very high concentration of nitrogen in the free-stream gas mixture. However, to study the effect of free-stream gas composition on heating of the entry vehicle, different gas compositions are assumed.

The equilibrium chemical composition is determined by using a free energy minimization analysis as developed in reference 19. As mentioned above, the ACE computer program was used to determine various chemical species for different pressure, temperature, and free-stream conditions.

For initial study, 68 chemical species for the carbon-hydrogen-nitrogen system were included in the matrix of calculations for a given free-stream atmospheric compostion. The matrix was

Pressure: 0.1, 0.5, 1.0 and 0.5 atm)

Temperature: 2,000 K to 10,000 K in 500 K increments

Composition: 90% N_2 + 10% Ch_4, 50% N_2 + 50% CH_4, 10% N_2 + 90% CH_4

For different free-stream gas compositions, the variation in mole fraction of different species, as a function of temperature is illustrated in figures 5(a) to (d) for different pressures. There are about 20 chemical species shown in these figures. However, concentrations of some species are less than 0.05 percent for the range of temperature considered. Therefore, for this study, 17 chemical species (N_2, N, N^+, C_3, C_2, C, C^+, C_4H, C_3H, C_2H_2, C_2H, CN, H_2, H, H^+, HCN, and E^-) were considered for the shock-layer gas mixture.

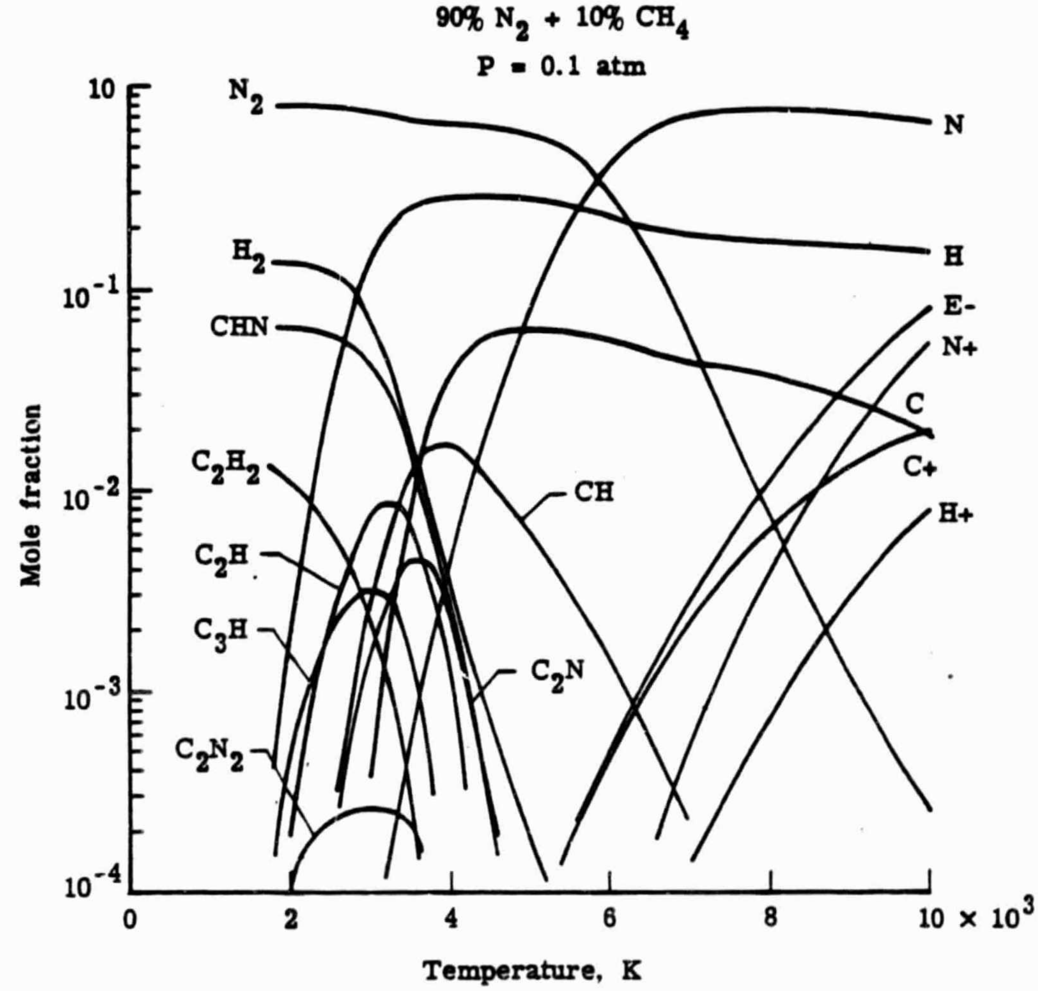

(a)

Figure 5. Variation in mole fraction of different species for p = 0.1 atm and 90% N_2 + 10% CH_4.

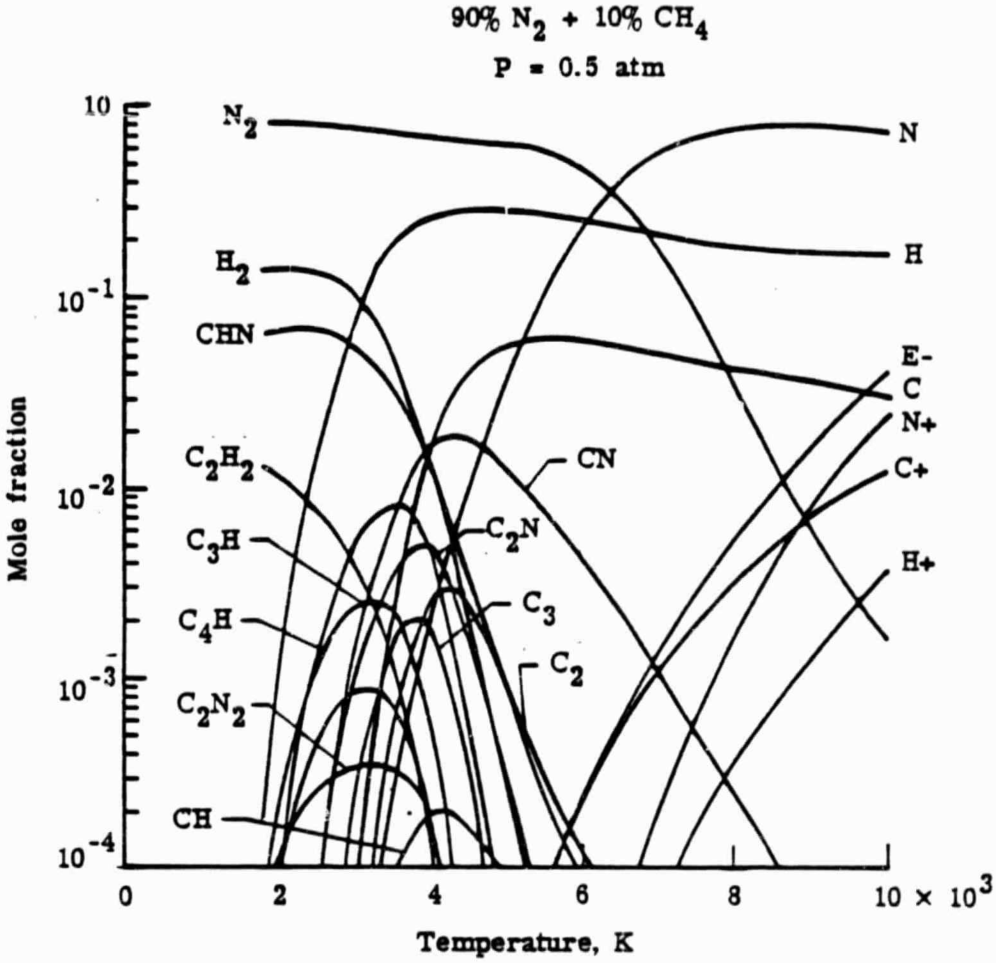

(b)

Figure 5. (Continued.)

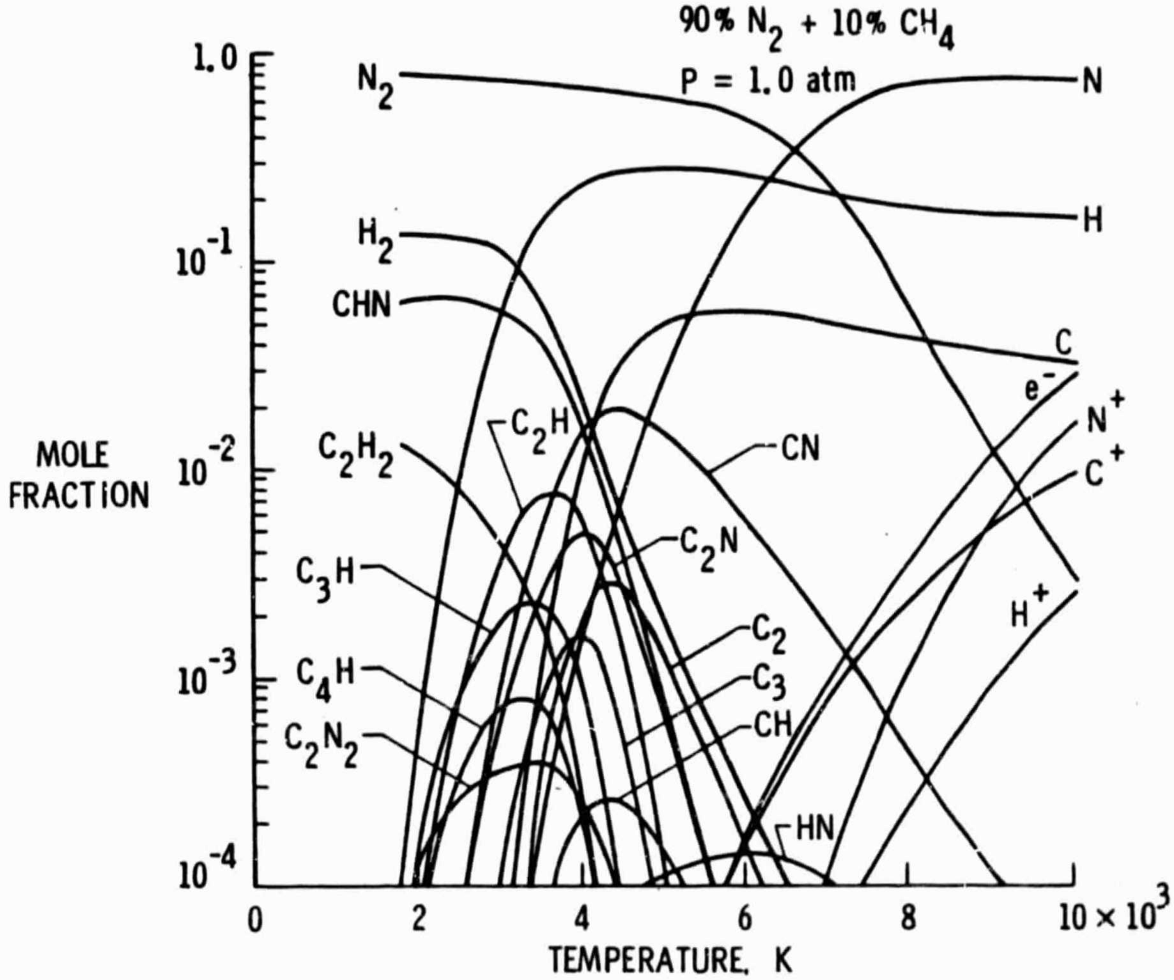

(c)

Figure 5. (Continued.)

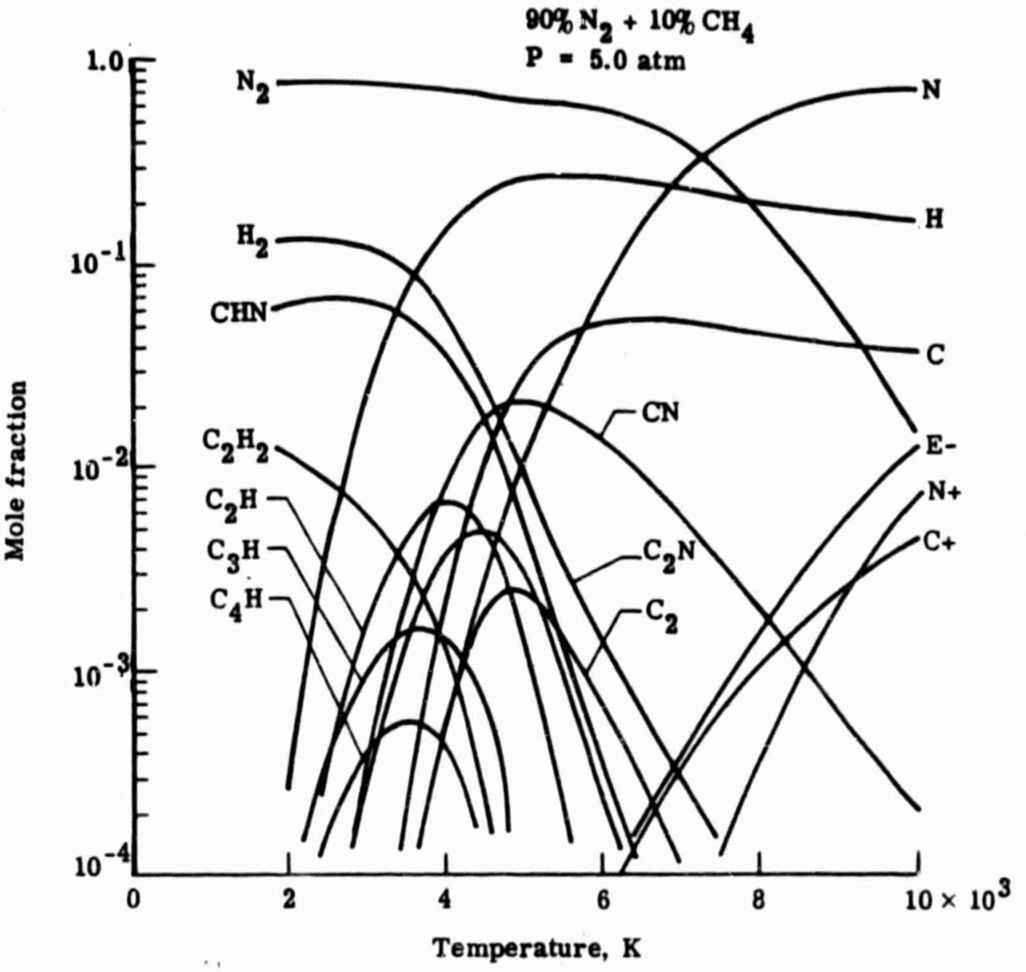

(d)

Figure 5. (Concluded.)

6. RADIATION TRANSPORT MODEL

An appropriate expression for the radiative flux, q_r, is needed for the solution of the energy equation presented in Chapter 2. This requires a suitable transport model and a meaningful spectral model for variation of the absorption coefficient of the gas.

In the present analysis the "tangent slab" assumption for radiative transfer has been used. This implies that the radiative energy transfer along the body is negligible in comparison to that transferred in the direction normal to the body. It should be noted the tangent slab approximation is used only for radiative transport and not for other flow variables. For a nonscattering medium and diffuse nonreflecting bounding surfaces, a one-dimensional expression for the spectral radiative flux is given by (refs. 20, 21):

$$q_{r\nu}(\tau_\nu) = 2\pi \left\{\varepsilon_\nu[B_\nu(0)E3(\tau_\nu) - B_\nu(\tau_{o\nu})E3(\tau_{o\nu} - \tau_\nu)] + \int_0^{\tau_\nu} B_\nu(t)E2(\tau_\nu - t)dt - \int_{\tau_\nu}^{\tau_{o\nu}} B_\nu(t)E2(t - t_\nu)dt\right\} \tag{6.1}$$

where

$$\tau_\nu = \int_0^y \alpha_\nu(y')dy'$$

$$E_n(t) = \int_0^1 \exp\left(\frac{-t}{\mu}\right)\mu^{n-2}d\mu$$

$$B_\nu = \left(\frac{h\nu^3}{c^2}\right)\left[\exp\left(\frac{h\nu}{KT}\right) -1\right]$$

The quantities $B_\nu(0)$ and $B_\nu(\tau_{0\nu})$ represent the radiosities of the body surface and shock respectively. The expression of total radiative flux is given by

$$q_r = \int_0^\infty q_{r\nu}(\tau_\nu)d\nu \tag{6.2}$$

In the shock layer, the radiative energy from the bow shock usually is neglectd in comparison to the energy absorbed and emitted by the gas layer. The expression for net radiative flux in the shock layer, therefore, is given by combining equations (6.1) and (6.2) as

$$q_r = 2\int_0^\infty \Big[q_\nu(0)E_3(\tau_\nu) + \int_0^{\tau_\nu} B_\nu(t)E_2(\tau_\nu - t)dt$$

$$- \int_{\tau_r}^{\tau_{0\nu}} B_\nu(t)E_2(t - \tau_\nu)dt\Big]d\nu \tag{6.3}$$

where $q_\nu(0) = \epsilon_\nu \pi B_\nu(T_s)$.

In this equation, the first two terms on the right represent the radiative energy transfer towards the bow shock while the third term represents the energy transfer towards the body. Upon denoting these contributions by q_r^+ and q_r^-, equation (6.3) can be written as

$$q_r = q_r^+ - q_r^- \tag{6.4}$$

The radiative flux, q_r is calculated with the radiative transport code RAD (ref. 22) which accounts for detailed nongray radiation absorption and emission processes. The chemical species considered for determining the radiative transport are N, N_2, N^+, N^-, N_2^+, H, H_2, H^-, e^-, C, C^-, C^+, C_2, C_3, and CN.

7. PHYSICAL CONDITIONS AND DATA SOURCE

As mentioned earlier, the entry body considered for this study is a 45-degree sphere cone at a zero degree angle of attack (fig. 4). The body temperature is assumed to be 2,000 K and, for most cases, the body nose radius is taken to be 0.2 m. The free-stream atmospheric compositions are assumed as 99.5% N_2 + 0.5% CH_4, 98% N_2 + 2% CH_4, 90% N_2 + 10% CH_4, 75% N_2 + 25% CH_4, 50% N_2 + 50% CH_4, 25% N_2 + 75% CH_4, and 10% N_2 + 90% CH_4. The high nitrogen concentration cases will be the realistic compositions for the Titan's atmosphere.

For the Titan aerocapture mission, entry trajectories have been generated by JPL. The altitude history for an aerocaputre vehicle is illustrated in figure 6 for two different (shallow and steep) entry angles. The entry trajectories and free-stream conditions used in this study are given in tables 3 to 9.

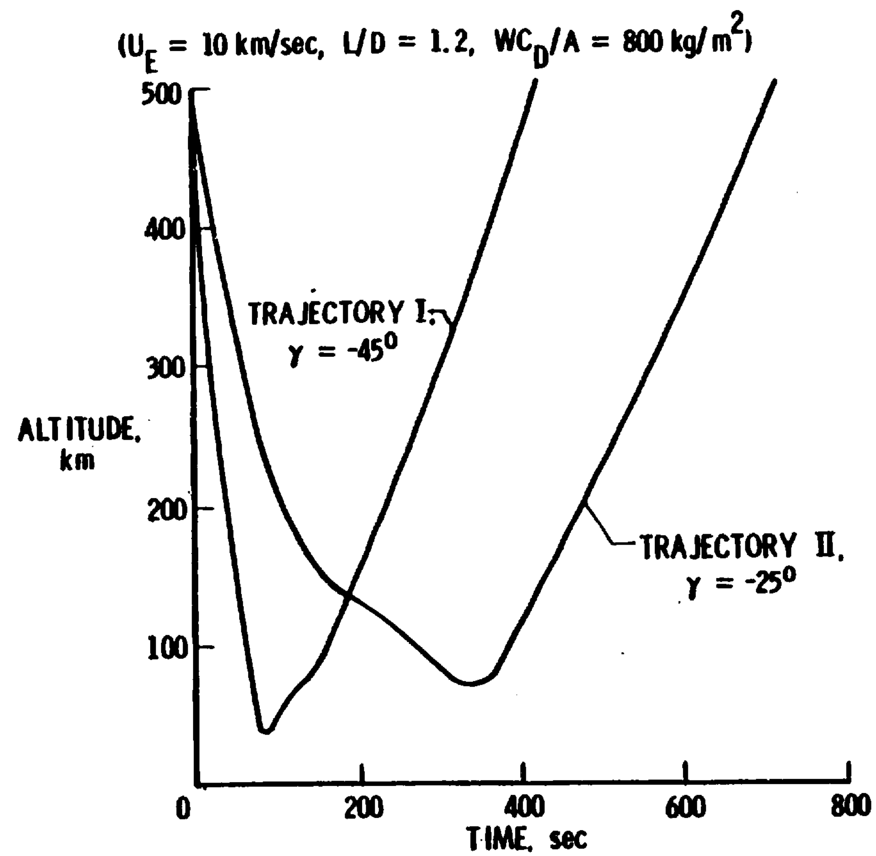

Figure 6. The altitude history for an aerocapture vehicle.

8. METHOD OF SOLUTION

A numerical procedure for solving the viscous shock-layer equations for stagnation and downstream regions is given by Davis (ref. 10). Moss (ref. 13) and Tiwari and Szema (ref. 12) applied this method of solution to reacting multicomponent mixtures. A modified form of this procedure is used in this study to obtain solutions of the viscous shock-layer equations. In this method, a transformation is applied to the viscous shock-layer equations in order to simplify the numerical computations. In this transformation most of the variables are normalized with their local shock values; the transformed variables are (refs. 12, 13):

$$\eta = \frac{n}{n_s} \qquad \bar{P} = \frac{P}{P_s}$$

$$\bar{u} = \frac{u}{u_s} \qquad \xi = s$$

$$\bar{\rho} = \frac{\rho}{\rho_s} \qquad \bar{K} = \frac{K}{K_s}$$

$$\bar{\mu} = \frac{\mu}{\mu_s} \qquad \bar{T} = \frac{T}{T_s}$$

$$\bar{C}_p = \frac{C_p}{C_{ps}} \qquad \bar{v} = \frac{v}{v_s}$$

$$\bar{H} = \frac{H}{H_s} \tag{8.1}$$

The transformations relating the differential quantities are

$$\frac{\partial(\ )}{\partial x} = \frac{\partial(\ )}{\partial \xi} - \frac{\eta}{n_s}\frac{dn_s}{d\xi}\frac{\partial(\ )}{\partial \eta} \tag{8.2}$$

$$\frac{\partial(\ )}{\partial n_s} = \frac{1}{n_s}\frac{\partial(\ )}{\partial_\eta} \qquad \frac{\partial^2}{\partial n_s} = \frac{1}{n_s}\frac{\partial^2(\ )}{\partial \eta} \tag{8.3}$$

After the governing equations are written in the transformed variables, the resulting second-order partial differential equations can be expressed in the following form:

$$\frac{\partial^2 W}{\partial \eta^2} + a_1 \frac{\partial W}{\partial \eta} + a_2 W + a_3 + a_4 \frac{\partial W}{\partial \xi} = 0 \tag{8.4}$$

The quantity W represents $\bar{u}$ in the s-momentum equation, $\bar{H}$ in the enthalpy energy equation, $\bar{C}_\ell$ in the elemental continuity equation. The coefficients a_1 to a_4 to be used in this study are exactly the same as given in references 12 and 13.

s-momentum, $W = \bar{u}$:

$$a_1 = \frac{1}{\bar{\mu}}\frac{\partial \bar{\mu}}{\partial \eta} + \frac{n_s \kappa}{1 + n_s \eta\kappa} + \frac{n_s \cos\theta}{r + n_s \eta \cos\theta}$$

$$+ \frac{n_s \rho_s u_s n_s'}{\varepsilon^2 \mu_s (1 + n_s \eta\kappa)} \frac{\overline{\rho u}\eta}{\bar{\mu}} - \frac{n_s \rho_s v_s}{\varepsilon^2 \mu_s} \frac{\overline{\rho v}}{\bar{\mu}}, \tag{8.5a}$$

$$a_2 = - \frac{\kappa n_s}{(1 + n_s \kappa\eta)} \frac{1}{\bar{\mu}}\frac{\partial \bar{\mu}}{\partial \eta} \frac{\kappa^2 n_s^2}{(1 + n_s \eta\kappa)^2} - \frac{\cos\theta\ n_s^2 \kappa}{(r + n_s \eta \cos\theta)(1 + n_s \eta\kappa)}$$

$$- \frac{\rho_s n_s^2 u_s'}{\varepsilon^2 \mu_s (1 + n_s \eta\kappa)} \frac{\overline{u\rho}}{\bar{\mu}} - \frac{n_s^2 \rho_s v_s \kappa}{\varepsilon^2 \mu_s (1 + n_s \eta\kappa)} \frac{\overline{\rho v}}{\bar{\mu}}, \tag{8.5b}$$

$$a_3 = -\frac{p_s n_s^2}{\epsilon^2 \mu_s u_s (1 + n_s \eta\kappa)\,\overline{\mu}} \left[\frac{\partial \bar{P}}{\partial \xi} + \frac{p_s' \bar{P}}{P_s} - \frac{n_s' \eta}{n_s} \frac{\partial \bar{P}}{\partial \eta}\right] \tag{8.5c}$$

$$a_4 = -\frac{\rho_s u_s n_s^2}{\epsilon^2 \mu_s (1 + n_s \eta\kappa)} \frac{\overline{\rho}\overline{u}}{\overline{\mu}} \tag{8.5d}$$

Energy (enthalpy, $W = \bar{H}$:

$$a_1 = \frac{1}{\bar{\mu}} \frac{\partial \bar{\mu}}{\partial \eta} - \frac{1}{\overline{Pr}} \frac{\partial \overline{Pr}}{\partial \eta} + n_s \left[\frac{\kappa}{1 + n_s \eta\kappa} + \frac{\cos\theta}{r + n_s \eta \cos\theta}\right]$$

$$+ \frac{\rho_s Pr_s \overline{Pr}\, n_s}{\epsilon^2 \mu_s \overline{\mu}} \left[\frac{n_s' u_s \eta \overline{u}\overline{\rho}}{1 + n_s \eta\kappa} - v_s \overline{\rho}\overline{v}\right] \tag{8.6a}$$

$$a_2 = a_4 \frac{H_s'}{H_s} \tag{8.6b}$$

$$a_3 = \frac{Pr_s \overline{Pr}\, n_s^2}{\mu_s \overline{\mu} H_s} \left[\frac{1}{n_s} \frac{\partial \psi}{\partial \eta} + \left(\frac{\kappa}{1 + n_s \eta\kappa} + \frac{\cos\theta}{r + n_s \eta \cos\theta}\right)\psi\right] + \frac{Prp_s v_s \overline{v}}{\epsilon^2 \mu_s \overline{\mu} H_s} \frac{\partial P}{\partial \eta}$$

$$- \frac{\overline{Pr} P_{r,s}}{\epsilon^2 \mu_s H_s \overline{\mu}} \left[\frac{1}{n_s} \frac{\partial q_R}{\partial \eta} + q_R \left(\frac{\kappa}{1 + n_s \eta\kappa)} \frac{\cos\theta}{r \quad n_s \cos\theta}\right)\right] \tag{8.6c}$$

$$a_4 = -\frac{Pr_s n_s^2 \rho_s u_s \overline{Pr}\overline{u}\overline{\rho}}{\epsilon^2 \mu_s (1 + n_s \eta\kappa)\,\overline{\mu}} \tag{8.6d}$$

where

$$\psi = \frac{\mu_s}{n_s Pr_s}\left[-\frac{\overline{\mu}}{\overline{Pr}}\sum_{i=1}^{N} h_i \frac{\partial C_i}{\partial \eta} + \frac{u^2 \overline{\mu}\,\overline{u}}{\overline{Pr}}(Pr_s \overline{Pr} - 1)\frac{\partial \overline{u}}{\partial \eta}\right]$$

$$- \frac{\mu_s u_s^2 \kappa \overline{\mu}\,\overline{u}^2}{1 + n_s \eta\kappa} \tag{8.6e}$$

The preceding energy equation is for the thin shock-layer approximation. When equation (2.3) is used for the n-momentum equation, the following term must be added to equation (8.6c):

$$- \frac{Pr_s v_s n_s^2 \rho_s}{\varepsilon^2 \mu_s H_s}\frac{\overline{Pr}\,\overline{\rho}\,\overline{v}}{\overline{\mu}}\left[\frac{u_s \overline{u}}{1 + n_s \eta\kappa}\left(\overline{v}v_s' + v_s\frac{\partial \overline{v}}{\partial \xi} - \frac{n_s' \eta v_s}{n_s}\frac{\partial \overline{v}}{\partial \eta}\right)\right.$$

$$\left. + \frac{v_s^2 \overline{v}}{n_s}\frac{\partial \overline{v}}{\partial \eta}\right] \tag{8.6f}$$

Elemental continuity, $W = C_\ell$:

$$a_1 = \frac{1}{\widetilde{PL}}\frac{\partial \widetilde{PL}}{\partial \eta} + n_s\left[\frac{\kappa}{1 + n_s \eta\kappa} + \frac{\cos\theta}{r + n_s \eta \cos\theta}\right]$$

$$- \frac{\rho_s v_s n_s \overline{v}}{\varepsilon^2 \widetilde{PL}} + \frac{n_s \rho_s u_s n_s' \overline{\rho}\,\overline{u}\eta}{\varepsilon^2 \widetilde{PL}(1 + n_s \eta\kappa)} \tag{8.7a}$$

$$a_2 = 0 \tag{8.7b}$$

$$a_3 = \frac{1}{\widetilde{PL}}\left[\frac{\partial}{\partial \eta}\widetilde{PM} + n_s \widetilde{PM}\left(\frac{k}{1 + n_s \eta\kappa} + \frac{\cos\theta}{r + n_s \eta\cos\theta}\right)\right] \tag{8.7c}$$

$$a_4 = - \frac{n_s^2 \rho_s u_s}{\varepsilon^2 (1 + n_s \eta\kappa)} \frac{\overline{\overline{\rho u}}}{\widetilde{PL}} \tag{8.7d}$$

where

$$\widetilde{PL} = \frac{\mu_s \overline{\mu}_L}{Pr_s \overline{Pr}} \tag{8.7e}$$

and

$$PM = \sum_{i=1}^{NS} \delta_{i\ell} \frac{M_\ell^*}{M_i^*} \sum_{\substack{k=1 \\ \neq 1}}^{NS} \Delta b_{ik} \frac{\partial C_k}{\partial \eta} \tag{8.7f}$$

for multicomponent diffusion and for binary diffusion:

$$PL = \frac{\mu_s \overline{\mu}\zeta}{Pr_s \overline{Pr}} \tag{8.7g}$$

$$\widetilde{PM} = 0 \tag{8.7h}$$

The remaining equations are written as follows:

Continuity:

$$\frac{\partial}{\partial \xi} \left[n_s (r + n_s \eta \cos\theta) \rho_s u_s \overline{\overline{\rho u}} \right] + \frac{\partial}{\partial \eta} \Big[(r + n_s \eta \cos\theta) \Big]$$

$$\left\{ (1 + n_s \eta\kappa) \rho_s v_s \overline{\overline{\rho v}} - n_s' \eta \rho_s u_s \overline{\overline{\rho u}} \right\} \Big] = 0 \tag{8.8}$$

n-momentum:

$$\frac{\bar{\rho}\bar{u}}{1 + n_s \eta\kappa}\;\frac{v_s'}{v_s}\bar{v} + \frac{\partial \bar{v}}{\partial \xi} + \frac{v_s}{u_s}\,\frac{\bar{\rho}\bar{v}}{n_s}\,\frac{\partial \bar{v}}{\partial \eta}$$

$$- \frac{u_s}{v_s}\,\frac{\kappa}{(1 + n_s \eta\kappa)}\,\bar{\rho}\bar{u}^2 + \frac{P_s}{\rho_s u_s n_s v_s}\,\frac{\partial \bar{P}}{\partial \eta} = 0 \qquad (8.9a)$$

which becomes

$$\frac{\partial \bar{P}}{\partial \eta} = \frac{n_s \rho_s u_s^2 \kappa}{P_s (1 + n_s \eta\kappa)}\,\bar{\rho}\bar{u}^2 \qquad (8.9b)$$

if the thin shock-layer approximation is made

State:

$$\bar{P} = \bar{\rho}\,\bar{T}\,\frac{M^*}{M_s^*} \qquad (8.10)$$

The boundary conditions at the body surface (the surface boundary conditions) in terms of transformed variables are as follows:

No slip: $\bar{u} = 0$ (8.11a)

$$\bar{v} = 0 \qquad (8.11b)$$

$$\bar{T} = \text{const.} \qquad (8.11c)$$

$$\bar{H} = \sum_{i=1}^{N} h_i C_{i\,w} \Big/ \sum_{i=1}^{N} h_i C_{i\,s} \qquad (8.11d)$$

With slip:

$$\bar{u} = \epsilon^2 A_1\left(\frac{P_s}{\rho_s}\right)^{1/2}\left(\frac{\mu_s}{P_s}\right)\left(\frac{1}{n_s}\right)\left(\frac{\bar{P}}{\bar{\rho}}\right)^{1/2}\left(\frac{\bar{\mu}}{\bar{P}}\right)\left[\left(\frac{\partial \bar{u}}{\partial \eta}\right) - n_s \bar{u}\right] \quad (8.12a)$$

$$\bar{v} = 0 \quad (8.12b)$$

$$\bar{T} = \bar{T}_w + \epsilon^2 A_2\left(\frac{\mu_s}{P_s}\right)\left(\frac{1}{n_s}\right)(T_s)^{1/2}\left[(\gamma - 1)\frac{\bar{T}}{\gamma}\right]^{1/2}\left(\frac{\bar{\mu}}{\bar{P}}\right)\left(\frac{\partial \bar{T}}{\partial \eta}\right) \quad (8.12c)$$

$$\bar{h} = \bar{h}_w + \epsilon^2 A_2\left(\frac{\mu_s}{P_s}\right)\left(\frac{1}{n_s}\right)\left(\frac{P_s}{\rho_s}\right)^{1/2}\left(\frac{\bar{u}}{\bar{P}}\right)\left(\frac{\bar{P}}{\bar{\rho}}\right)^{1/2}\frac{\partial \bar{h}}{\partial \eta} \quad (8.12d)$$

The conditions at the shock (i.e., the transformed shock conditions at $\eta = 1$) for slip or no slip cases are

$$\bar{u} = \bar{T} = \bar{H} = \bar{v} = \bar{P} = \bar{\rho} = 1 \quad (8.13)$$

When downstream numerical solutions are required, it is necessary to have an accurate solution for the flow along the stagnation streamline. A truncated series which has the same form as that used by Kao (ref. 23) is used to develop the stagnation streamline equations. The flow variables are expanded about the axis of symmetry with respect to nondimensional distance ξ near the stagnation streamline as

$$p(\xi,\eta) = p_1(\eta) + p_2(\eta)\xi^2 + \ldots \quad (8.14a)$$

$$u(\xi,\eta) = u_1(\eta)\xi + \ldots \quad (8.14b)$$

$$v(\xi,\eta) = v_1(\eta) + \ldots \quad (8.14c)$$

$$\rho(\xi,\eta) = \rho_1(\eta) + \ldots \quad (8.14d)$$

$$T(\xi,\eta) = T_1(\eta) + \ldots \quad (8.14e)$$

(cont'd)

$$h(\xi,\eta) = h_1(\eta) + \ldots \tag{8.14f}$$

$$\mu(\xi,\eta) = \mu_1(\eta) + \ldots \tag{8.14g}$$

$$K(\xi,\eta) = K_1(\eta) + \ldots \tag{8.14h}$$

$$C_p(\xi,\eta) = C_{p,1}(\eta) + \ldots \tag{8.14i}$$

$$\tilde{C}_\ell(\xi,\eta) = \tilde{C}_{\ell,1}(\eta) + \ldots \tag{8.14j}$$

(concl'd)

The shock-standoff distance is expressed by

$$n_s = n_{1,s} + n_{2s}\,\xi^2 + \ldots \tag{8.15}$$

Since ξ is small and the curvature κ is approximately of order one in the stagnation region, it is logical to say that (see fig. 4):

$$\beta \approx \xi \tag{8.16}$$

Now, since $\theta = (\pi/2) - \beta$, one may express

$$\alpha \approx \frac{\pi}{2} + \xi\left(\frac{2n_{2s}}{1 + n_{1s}} - 1\right) \tag{8.17}$$

By using equations (8.15) to (8.17), the shock relations, equations (3.3) to (3.8), can be expressed in terms of expanded variables as

$$v_s = v_{1s} + \ldots \approx -\frac{1}{\rho_{1s}} \tag{8.18}$$

$$u_s = u_{1s}\,\xi + \ldots \approx \xi\left[1 - \frac{2n_{2s}}{1 + n_{1s}}\left(1 + \frac{1}{\rho_{1s}}\right)\right] \tag{8.19}$$

$$p_s = p_{1s} + p_{2s}\xi^2 + \ldots \approx \frac{1}{\gamma M_\infty^2} + \left(\frac{1}{\rho_{1s}}\right)$$

$$- \xi^2 \left[\left(1 - \frac{1}{\rho_{1s}}\right)\left(1 - \frac{2n_{2s}}{1 + n_{1s}}\right)^2\right] \tag{8.20}$$

$$h_s = h_{1s} + \ldots \approx \frac{1}{M_\infty^2(\gamma_\infty - 1)} + \frac{1}{2}\left(1 - \frac{1}{\rho_{1s}}\right) \tag{8.21}$$

Since equations (8.19) and (8.20) involve n_{2s}, these terms cannot be determined from the stagnation solutions. Thus, a value of $n_{2s} = 0$ is assumed to start the solution. This assumption is removed by iterating on the solution by using the previous shock-standoff distances to define n_{2s}.

Along the stagnation streamline, the second-order differential equation is written as

$$\frac{d^2W}{d\eta^2} + a_1 \frac{dw}{d\eta} + a_2 + a_3 = 0 \tag{8.22}$$

The coefficients in equation (8.22) are defined as

s-momentum, $W = \bar{u}$:

$$a_1 = \frac{1}{\bar{\mu}_1}\frac{d\bar{\mu}_1}{d\eta} + \frac{2n_{1s}}{1 + n_{1s}\eta} - \frac{n_{1s}\rho_{1s}v_{1s}}{\epsilon^2\mu_{1s}}\frac{\bar{\rho}_1\bar{v}_1}{\bar{\mu}_1} \tag{8.23a}$$

$$a_2 = -\frac{n_{1s}}{1 + n_{1s}\eta}\left[\frac{1}{\bar{\mu}_1}\frac{d\bar{\mu}_1}{d\eta} + \frac{2n_{1s}}{1 + n_{1s}} + \frac{\rho_{1s}n_{1s}u_{1s}}{\epsilon^2\mu_{1s}}\frac{\bar{u}_1\bar{\rho}_1}{\bar{\mu}_1}\right.$$

$$\left. + \frac{n_{1s}\rho_{1s}v_{1s}}{\epsilon^2\mu_{1s}}\frac{\bar{\rho}_1\bar{v}_1}{\bar{\mu}_1}\right] \tag{8.23b}$$

$$a_3 = \frac{-2P_{1s}\bar{n}^2{}_{1s}}{\epsilon^2\mu_{1s} 1 + n_{1s}\,\eta)u_{1s}\,\bar{\mu}}\;\bar{P}_2 + \frac{P_{2s}\bar{P}_1}{P_{1s}} - \frac{n_{1s}\eta}{\eta_{1s}}\frac{d\bar{P}_1}{d\eta} \tag{8.23c}$$

Energy (enthalpy), $W = \bar{H}$:

$$a_1 = \frac{1}{\bar{\mu}_1}\frac{d\bar{\mu}_1}{d\eta} - \frac{1}{\bar{Pr}_1}\frac{d\bar{Pr}_1}{d\eta} + \frac{2n_{1s}}{1 + n_{1s}\,\eta} - \frac{n_{1s}\rho_{1s}Pr_{1s}v_{1s}}{\epsilon^2\mu_{1s}}\frac{\bar{\rho}_1\bar{Pr}_1\bar{v}_1}{\bar{\mu}_1} \tag{8.24a}$$

$$a2 = 0 \tag{8.24b}$$

$$a_3 = \frac{Pr_{1s}\bar{n}^2{}_{1s}}{\mu_{1s}H_{1s}}\frac{\bar{Pr}_1}{\bar{\mu}_1}\;\frac{1}{n_{1s}}\frac{d\psi}{d\eta} + \frac{2\psi}{1 + \eta\; n_{1s}} \tag{8.24c}$$

Elemental continuity, $W = C_\ell$:

$$a_1 = \frac{1}{\tilde{PL}}\frac{d\tilde{PL}}{d\eta} + 2\left[\frac{n_{1s}}{1 + \eta n_{1s}} - \frac{n_{1s}\rho_{1s}v_{1s}\bar{\rho}_1\bar{v}_1}{\epsilon^2\tilde{PL}}\right] \tag{8.25a}$$

$$a2 = 0 \tag{8.25b}$$

$$a_3 = \frac{1}{\tilde{PL}}\left[\frac{d\tilde{PM}}{d\eta} + 2\;\frac{n_{1s}\tilde{PM}}{1+\eta n_{1s}}\right] \tag{8.25c}$$

The remaining equations are written as follows:

Continuity:

$$\frac{d}{d\eta}\left[(1 + n_{1s}\eta)^2\;\rho_{1s}v_{1s}\bar{\rho}_1\bar{v}_1\right] = -2n_{1s}(1 + n_{1s}\eta)\rho_{1s}u_{1s}\bar{\rho}_1\bar{u}_1 \tag{8.26}$$

n-momentum:

$$\frac{d\bar{P}_1}{d\eta} = -\frac{V^2{}_{1s}\rho_{1s}}{P_{1s}}\bar{\rho}_1\bar{v}_1\frac{d\bar{v}_1}{d\eta} \tag{8.27}$$

When the thin shock-layer approximation is made, the n-momentum equation becomes

$$\frac{d\bar{P}_1}{d\eta} = 0 \tag{8.28}$$

The governing second-order partial differential equations are solved by employing an implicit finite-difference method. A variable grid spacing (fig. 7) is used in the η-direction so that the grid spacing can be made small in the region of large gradients. In the figure, m is a station measured along the body surface and n denotes the station normal to the body surface. The derivatives are converted to finite-difference form by using Taylor's series expansions. Thus, unequal space central difference equations in the η-direction at point m, n can be written as

$$\left.\frac{\partial W}{\partial \eta}\right)_n = \frac{\Delta\eta_{n-1}}{\Delta\eta_n(\Delta\eta_{n-1} + \Delta\eta_n)} W_{m,n+1} - \frac{\Delta\eta_n}{\Delta\eta_{n-1}(\Delta\eta_{n-1} + \Delta\eta_n)} W_{m,n-1} + \frac{\Delta\eta_n - \Delta\eta_{n-1}}{\Delta\eta_n\Delta\eta_{n-1}} W_{m,n} \tag{8.29a}$$

$$\left.\frac{\partial^2 W}{\partial \eta^2}\right)_n = \frac{2}{\Delta\eta_n(\Delta\eta_n + \Delta\eta_{n-1})} W_{m,n+1} - \frac{2}{\Delta\eta_n\Delta\eta_{n-1}} W_{m,n} + \frac{2}{\Delta\eta_{n-1}(\Delta\eta_n + \Delta\eta_{n-1})} W_{m,n+1} \tag{8.29b}$$

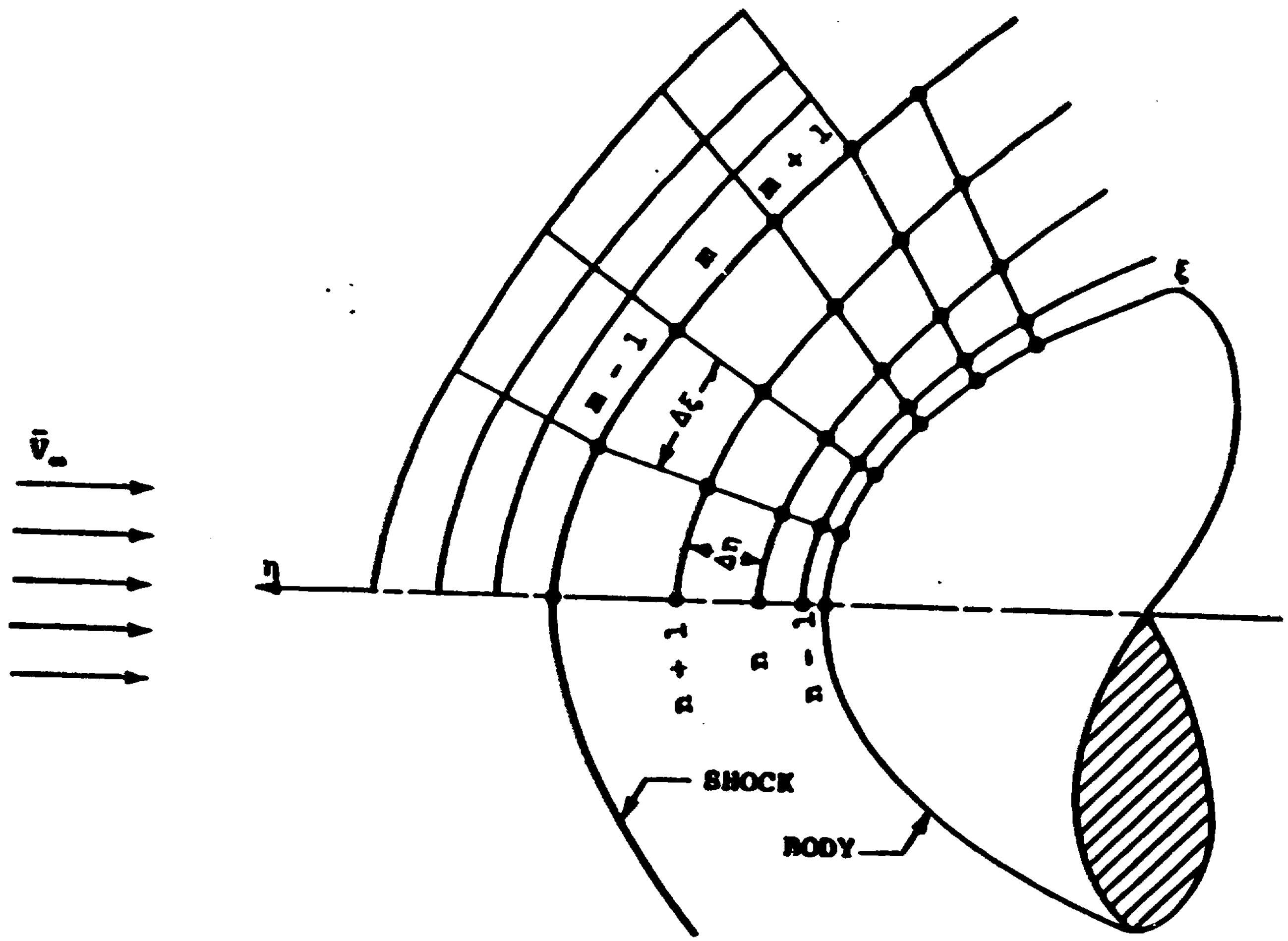

Figure 7. Finite-difference representation of flow field.

$$\left.\frac{\partial W}{\partial \xi}\right)_m = \frac{W_{m,n} - W_{m-1,n}}{\Delta\xi} \qquad (8.29c)$$

A typical finite-difference expansion of the standard differential equation is obtained by substituting the above equations in equation (8.4) as

$$A_n W_{m,\ n+1} + B_n W_{m,n} + C_n W_{m,\ n-1} + D_n = 0 \qquad (8.30)$$

where

$$A_n = \frac{2 + a_1 \Delta\eta_{n-1}}{\Delta\eta_n + \Delta\eta_{n-1}} \qquad (8.31a)$$

$$B_n = - \frac{2 - a_1 \left(\Delta\eta_n - \Delta\eta_{n-1}\right)}{\Delta\eta_n \Delta\eta_{n-1}} - \frac{a_2 - a_4}{\Delta\xi_{m-1}} \qquad (8.31b)$$

$$C_n = \frac{2 - a_1 \Delta\eta_n}{\Delta\eta_{n-1}\left(\Delta\eta_n + \Delta\eta_{n-1}\right)} \qquad (8.31c)$$

$$D_n = \frac{a_3 - a_4 W_{m-1,n}}{\Delta\xi_{m-1}} \qquad (8.31d)$$

If it is assumed that

$$W_{m,n} = E_n W_{m,\ n+1} + F_n \qquad (8.32)$$

or

$$W_{m,\ n-1} = E_{n-1} W_{m,n} + F_{n-1} \qquad (8.33)$$

then substituting (8.33) into equation (8.30) yields

$$W_{m,n} = \left[\frac{-An}{B_n + C_n E_{n-1}}\right] W_{m,n+1}$$

$$+ \frac{-D_n - C_n F_{n-1}}{B_n + C_n E_{n-1}} \tag{8.34}$$

By comparing equations (8.32) and (8.33), one finds

$$E_n = \frac{-An}{B_n - C_n E_{n-1}} \tag{8.35}$$

$$F_n = \frac{-D_n - C_n F_{n-1}}{B_n + C_n E_{n-1}} \tag{8.36}$$

Now, since E_1 and F_1 are known from the boundary conditions, E_n and F_n can be calculated from equations (8.35) and (8.36). The quantities $W_{m,n}$ at point m,n can now be calculated from equation (8.32).

The overall solution procedure starts with evaluation of the flow properties immediately behind the shock by using the Rankine-Hugoniot relations. With known shock and body surface conditions, the solutions are obtained first for the stagnation streamline. With this solution providing the initial conditions, the solution is marched downstream to the desired body location. Each of the second-order partial differential equations is integrated numerically by using the tridiagonal formalism of equation (8.4) and following the procedure described by equations (8.30) to (8.36). The first solution pass provides only an approximate flow-field solution. This is because, in the first solution, pass, the thin shock-layer form of the normal momentum equation is used, the stagnation streamline solution is assumed to be independent of downstream influence, the term $dn_s/d\xi$ is equal to zero at each body station, and the shock angle α is assumed to be the same as the body angle θ. These assumptions are removed by making one or more additional solution passes.

The shock solution procedure at any location is identical for the first and subsequent solution passes. However the shock angle α is defined differently for the first and subsequent solution passes. For the first solution pass, $\alpha = \theta$. For subsequent solution, the shock angle is defined as

$$\alpha = \theta + \tan^{-1}\left[\frac{n'_s}{1 + \kappa n_s}\right] \tag{8.37}$$

In the first solution pass, the viscous shock-layer equations are solved at any location m after obtaining the shock conditions. The converged solutions at station $m - 1$ are used as the initial guess for the solutions at station m. The solution is then iterated locally until convergence is achieved. For the stagnation streamline, guess values for dependent variables are used to start the solution.

In the first local iteration, both $\partial n_s/\partial\xi$ and $\partial w/\xi$ are assumed to be zero. The energy equation is integrated numerically to obtain a new temperature. By using this temperature, new values of thermodynamic and transport properties are calculated. Next, the x-momentum equation is inegrating to find the $\bar{u}$ component of velocity. The continuity equation is used to obtain both the shock-standoff distance and the $\bar{v}$ component of velocity. The pressure $\bar{p}$ is determined by integrating the normal momentum equation. The equation of state is used to determine the density. For example, the integration of the stagnation streamline continuity equation from 0 to η results in

$$\left[(1 + n_{1s}\eta)^2 \rho_{1s} v_{1s} \rho_1\right] v_1 = (-2n_{1s}\rho_{1s}u_{1s})A \tag{8.38}$$

where

$$A = \int_0^{\eta} (1 + n_{1s}\eta)\bar{\rho}_1\bar{u}_1 d\eta$$

This equation give the v-velocity component along the stagnation streamline. However, integration of the continuity equation from $\eta = 0$ to $\eta = 1$ results in

$$1 + n_{1s} \quad 2\rho_{1s}v_{1s} = - 2\rho_{1s}u_{1s}n_{1s} \ (B + C) \tag{8.39}$$

where

$$B = \int_0^1 \bar{\rho}_1\bar{u}d\eta, \ C = n_{1s} \int_0^1 \bar{\rho}_1\bar{u}_1\eta d\eta$$

The shock-standoff distance can be obtained from the solution of equation (8.39) as

$$n_{1s} = \frac{-(2v_{1s}+2Bu_{1s}) + [(2v_{1s}+2Bu_{1s})^2 - 4(v_{1s}+2Cu_{1s})v_{1s}]^{1/2}}{2(v_{1s}+2Cu_{1s})} \tag{8.40}$$

Integration of the downstream continuity equation from $\eta = 0$ to η results in

$$\frac{\partial}{\partial\xi}\left[\int_0^{\eta} n_{sm}(r+n_{sm}\eta \cos\theta)\, \rho_s u_s \bar{\rho}\bar{u} d\eta\right]$$

$$+ (r + n_{sm}\eta \cos\theta)[(1 + \eta n_{sm}\kappa)(\rho_s v_s \bar{\rho}\bar{v}) - n'_{sm}\eta\rho_s u_s \bar{\rho}\bar{u}] = 0 \tag{8.41}$$

This can be expressed in terms of the difference equation as

$$\frac{[(GG)_m - (GG)_{m-1}]}{\Delta\xi} + (FF)_m \bar{v} + (EE)_m = 0 \tag{8.42}$$

where

$$(EE)_m = (r + n_{sm}\eta \cos\theta)(1 + n_{sm}\eta\kappa)\rho_s v_s \bar{\rho}$$

$$(FF)_m = -(r + n_{sm}\eta \cos\theta)n'_{sm}\eta\rho_s u_s \bar{\bar{\rho u}}$$

$$(GG)_m = \int_0^\eta n_{sm}(r + n_{sm}\eta \cos\theta)\rho_s u_s \bar{\bar{\rho u}} d\eta$$

Now, the v-velocity component at each point on the station m can be obtained from equation (8.42).

For the downstream shock-standoff distance, integration of the continuity equation from $\eta = 0$ to $\eta = 1$ gives

$$\frac{\partial}{\partial\xi}[n_s^2 \cos\theta\, \rho_s u_s \int_0^1 \bar{\bar{\rho u}}\eta d\eta + n_s r\rho_s u_s \int_0^\eta \bar{\bar{\rho u}} d\eta$$

$$= (r + n_s \cos\theta)[n_s \rho_s u_s - (1 + n_s\kappa)\rho_s v_s] \tag{8.43}$$

By defining, for station m

$$D_1 = \cos\theta\, \rho_s u_s \int_0^1 \bar{\bar{\rho u}}\eta d\eta,\quad D_2 = r\rho_s u_s \int_0^1 \bar{\bar{\rho u}} d\eta$$

and denoting the same relations by D_3 and D_4 for station m-1, equation (8.43) can be expressed in terms of a difference equation as

$$[(D_1 n_s^2 + D_2 n_s)_m - (D_3 n_s + D_4 n_s)_{m-1}](\Delta\xi)^{-1}$$

$$= r \rho_s u_s n'_{sm} + \cos\theta \rho_s u_s n'_{sm} n_{sm} - r \rho_s v_s$$

$$- r \rho_s v_s \kappa n_{sm} - \cos\theta \rho_s v_s n_{sm} - \cos\theta \rho_s v_s \kappa n_s{}^2{}_m \tag{8.44}$$

This can be expressed in a quadratic form as

$$(II)n_{sm}^2 + (JJ)n_{sm} + (KK) = 0 \tag{8.45}$$

where

$$II = D_1 + \cos\theta \kappa \rho_s v_s \Delta\xi$$

$$JJ = D_2 + r \rho_s v_s \kappa\Delta\xi - \cos\theta \rho_s u_s n'_s \Delta\xi$$

$$KK = - [D_3 (n_s)^2_{m-1} + D_4 (n_s)_{m-1} + r \rho_s u_s n'_s \Delta\xi - r \rho_s v_s \Delta\xi]$$

Then, the shock-standoff distance at station m is obtained from equation (8.45) as

$$n_{sm} = \{-(FF) + [(JJ)^2 - 4(II)(KK)]^{1/2}\}[2(II)]^{-1} \tag{8.46}$$

The flow diagrams for computation procedure are shown in figures 8(a) to 8(d).

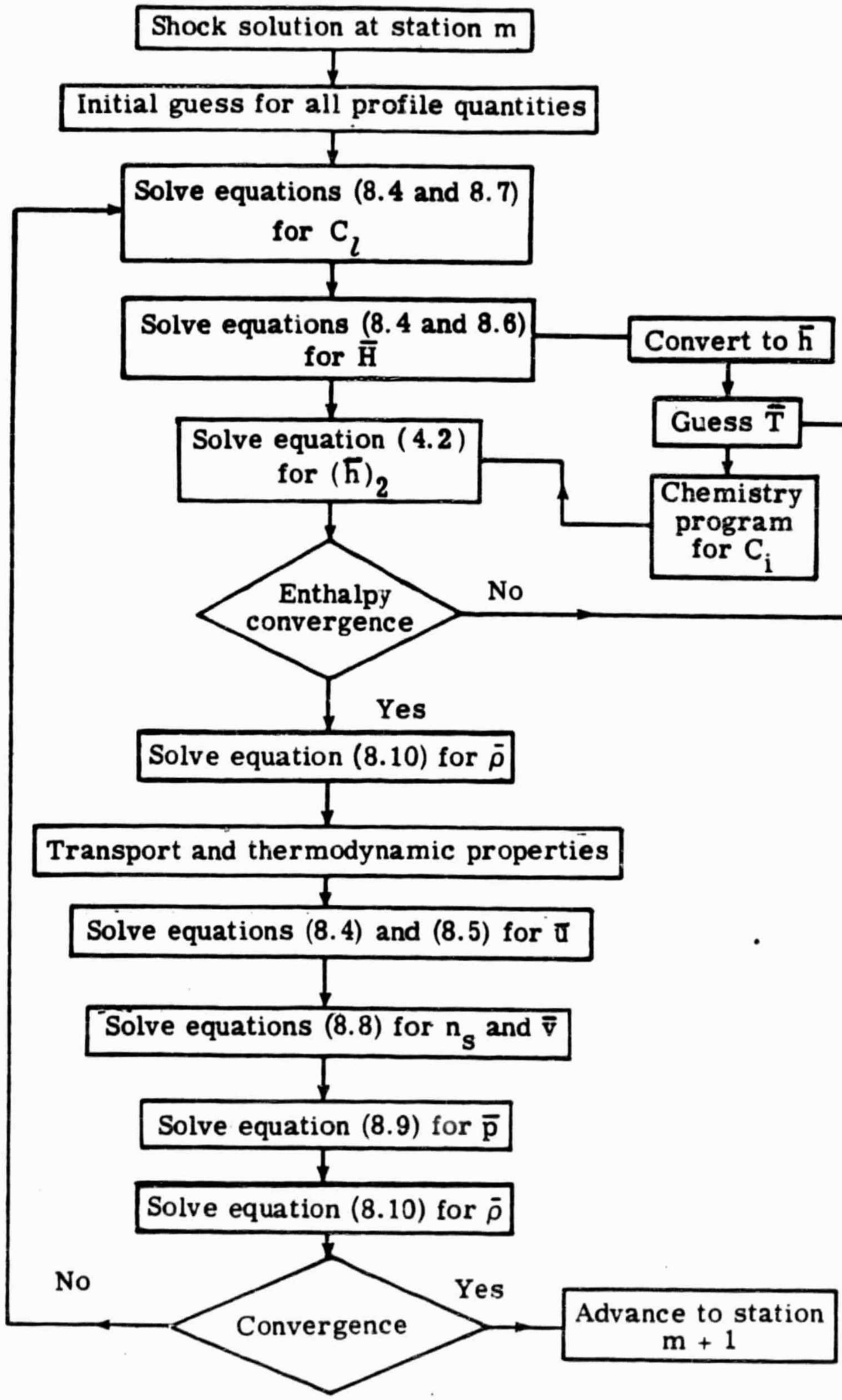

Figure 8(a). Flow chart for solution sequence of viscous shock-layer equation.

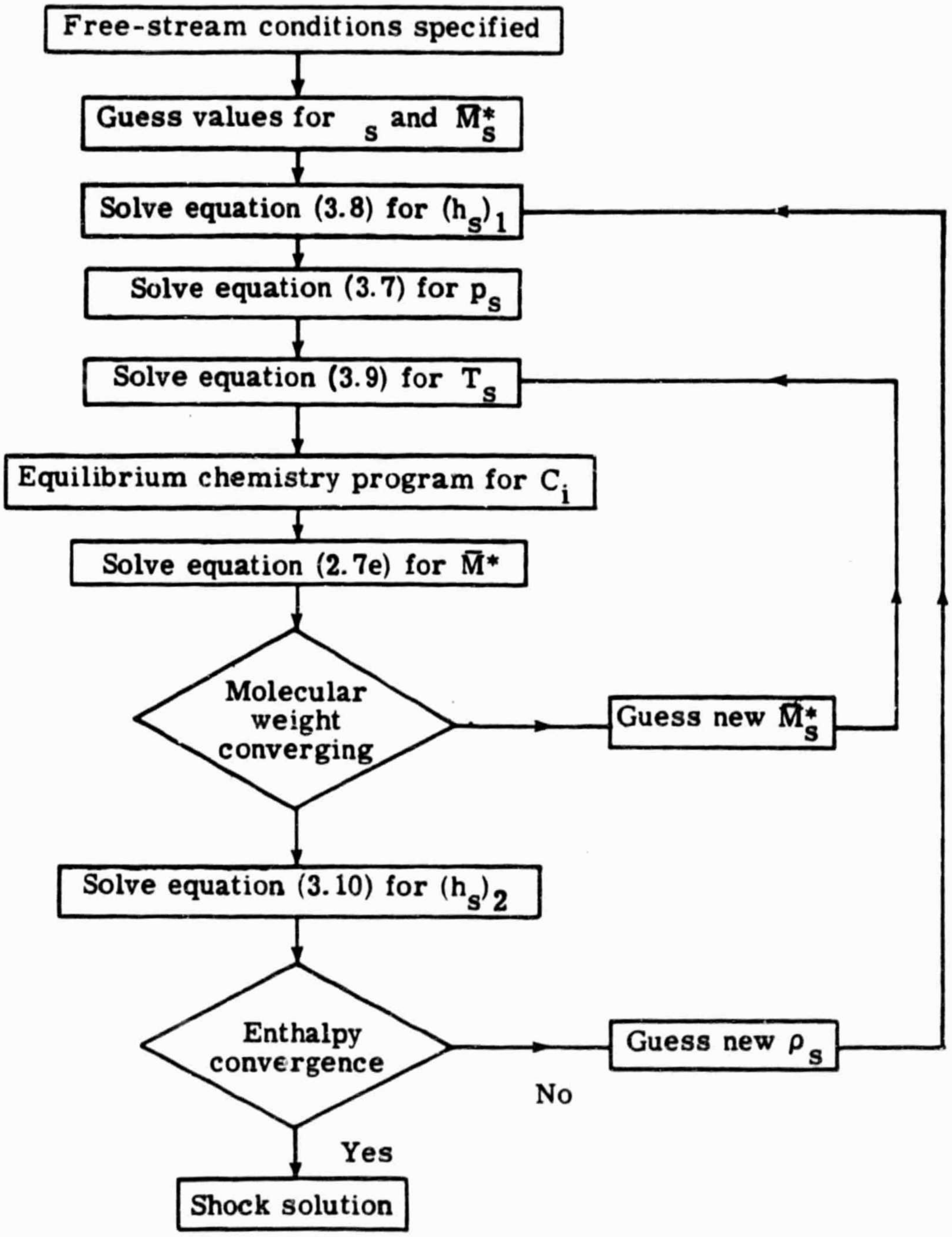

Figure 8(b). Flow chart for subroutine shock solution procedure.

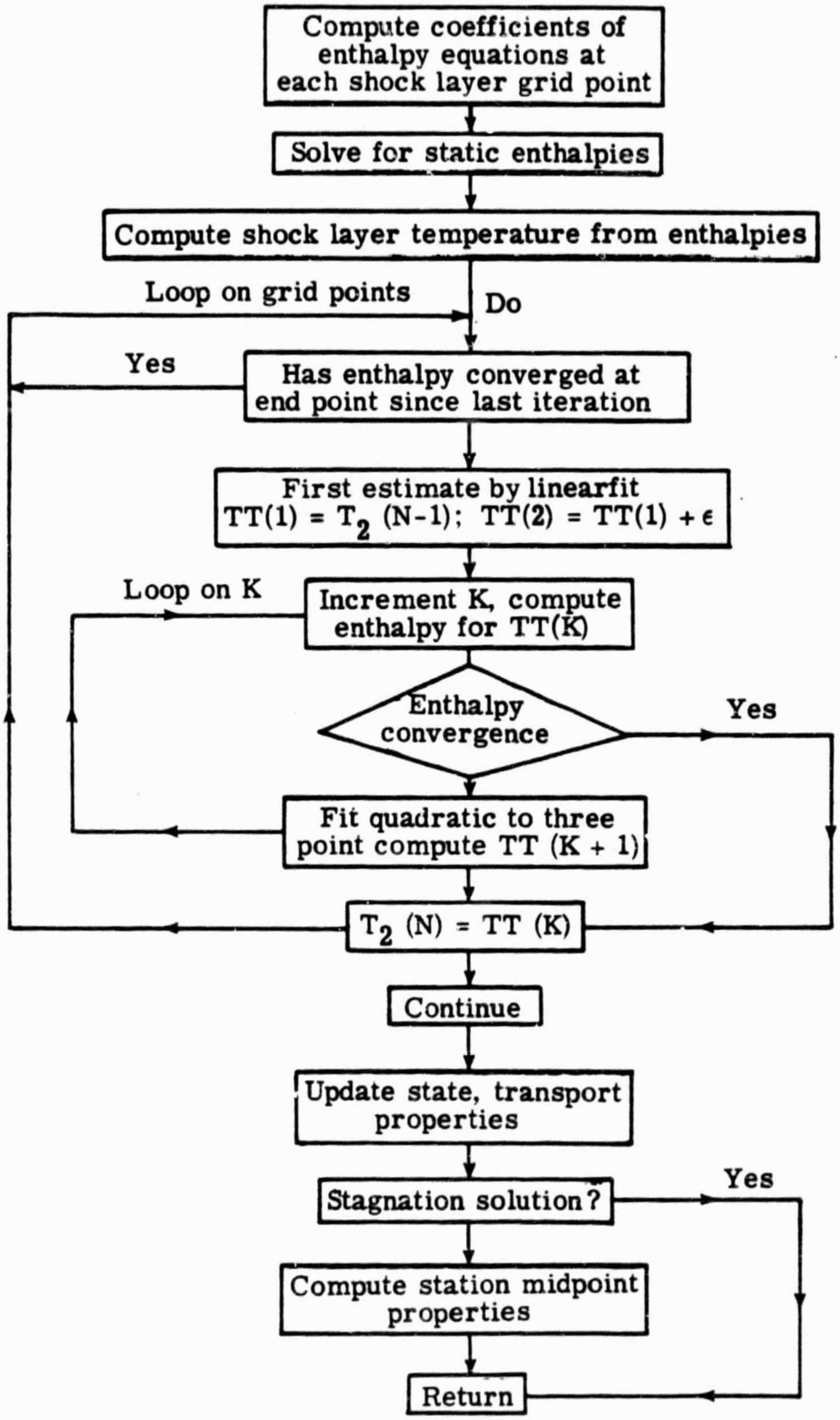

Figure 8(c). Flow chart for subroutine energy solution procedure.

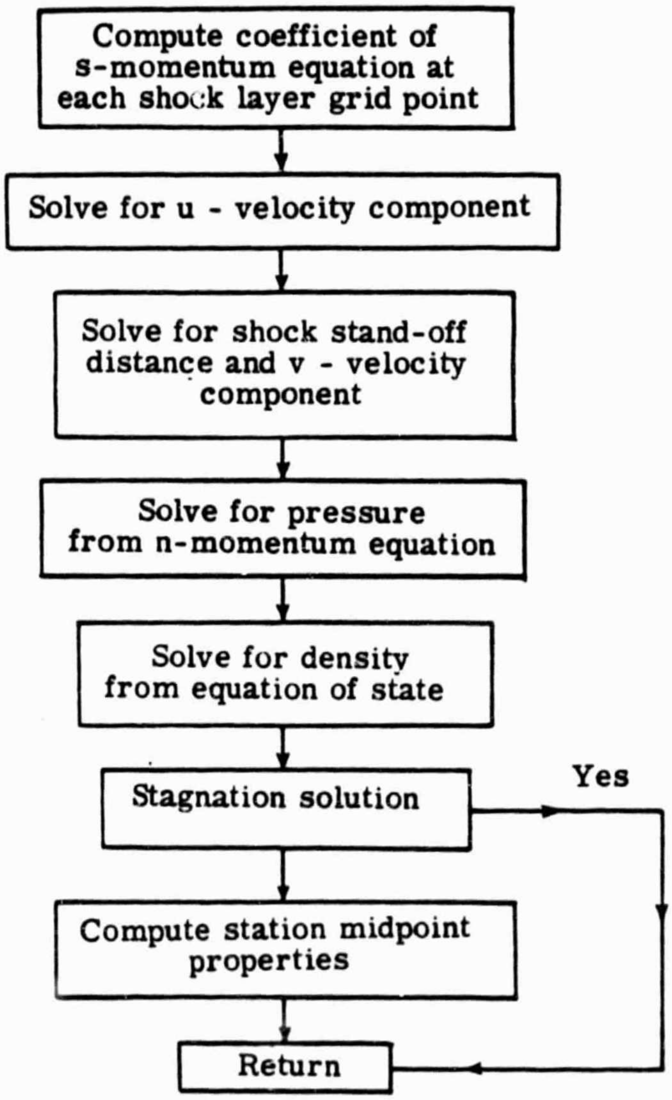

Figure 8(d). Flow chart for subroutine momentum solution procedure.

9. RESULTS AND DISCUSSION

The entry body considered for this study is a 45-degree sphere cone at zero degree angle of attack. The body surface temperature is taken to be uniform at 2,000 K and the body nose radius is 0.2 m. The entry trajectories and free-stream conditions are given in tables 3 to 9. Results have been obtained to investigate the effects of different gas composition, entry velocity and body nose radius on the stagnation-point convective and radiative heating. Specific results were obtained to determine the extent of convective and radiative heating along the body for free-stream gas composition of 90% N_2 + 10% CH_4, 98% N_2 + 2% CH_4, and 99.5% N_2 + 0.5% CH_4. The results for Trajectories I to VI with different free-stream gas compositions are given in tables 10 to 18. For the slip boundary conditions, some important results are presented in this section to show the effects of both the body and shock slips on the convective heating; these results are given in tables 19 to 24.

For Trajectory I, the effects of free-stream gas composition on the shock temperature are illustrated in figures 9 and 10. The results show that the shock temperature as well as the temperature in the shock layer increases with increasing N_2 concentration. This is because N_2 provides less energy accomodation in comparison to CH_4. The stagnation shock temperatures are relatively higher for early entry time (fig. 10); this, however, would be expected because of relatively higher free-stream velocities. The results of figure 9 show that the temperature gradient in the shock layer is restricted essentially in the regions near the body surface for all free-stream gas compositions.

The effects of gas composition on the stagnation-point convective and radiative heating for Trajectory I are illustrated in figures 11 and 12. The convective heating is seen to increase with increasing N_2 concentration (fig. 11), and peak heating occurs at an entry time of about 70 s. This is a direct consequence of the variation in the shock temperature. The situation, however, is not the same with respect to the radiative heating [figs.

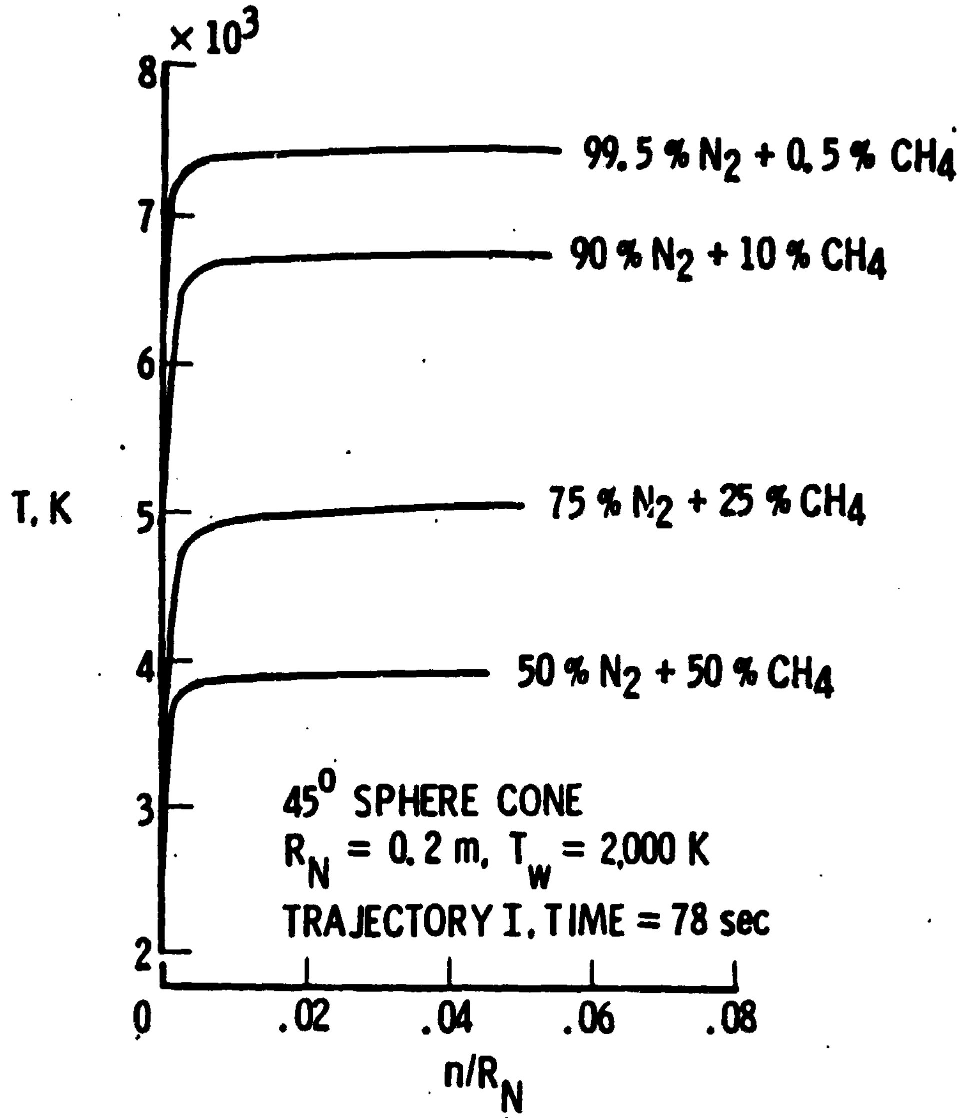

Figure 9. Effect of gas composition on temperature distribution along the stagnation streamline, Trajectory I (time = 78 s).

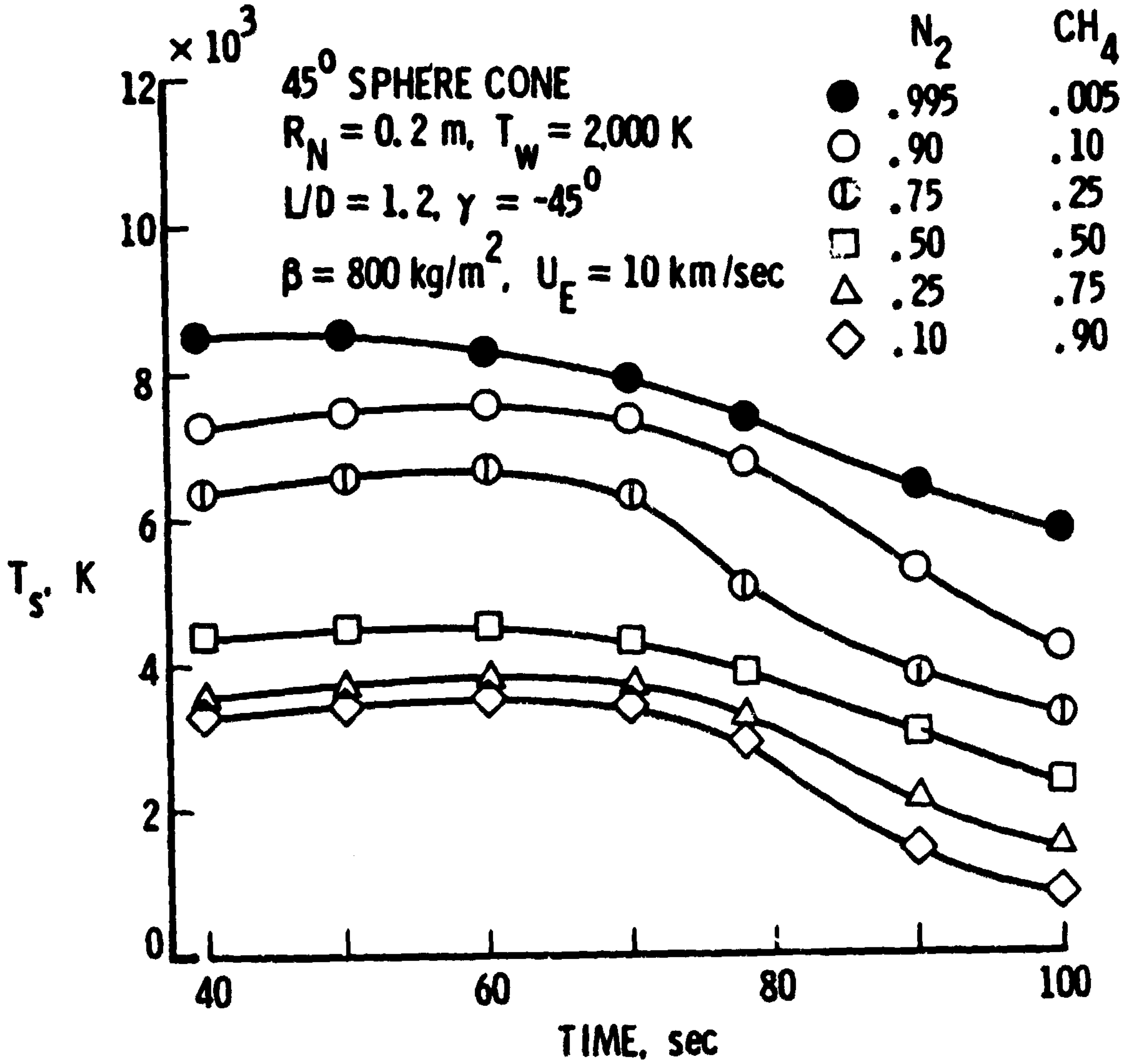

Figure 10. Effect of gas composition on stagnation-point shock temperature, Trajectory I.

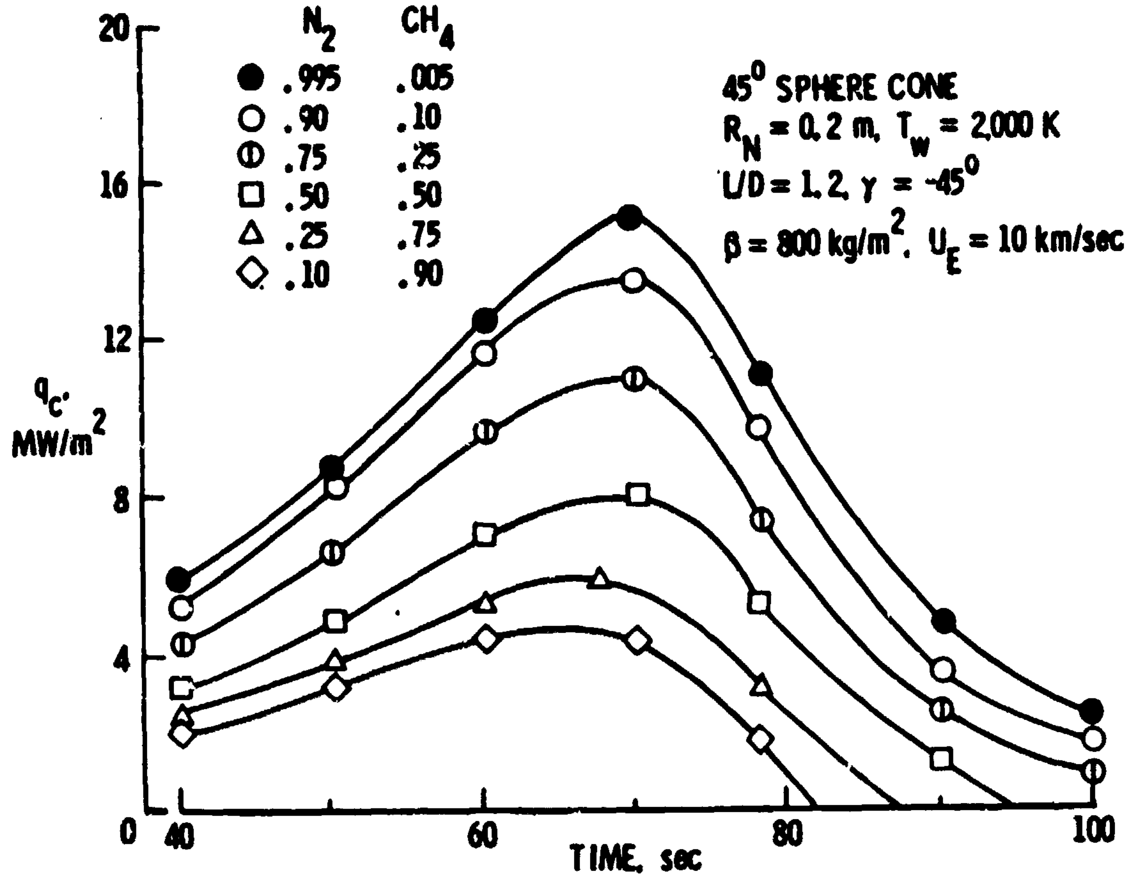

Figure 11. Effect of gas composition on stagnation-point convective heating, Trajectory I.

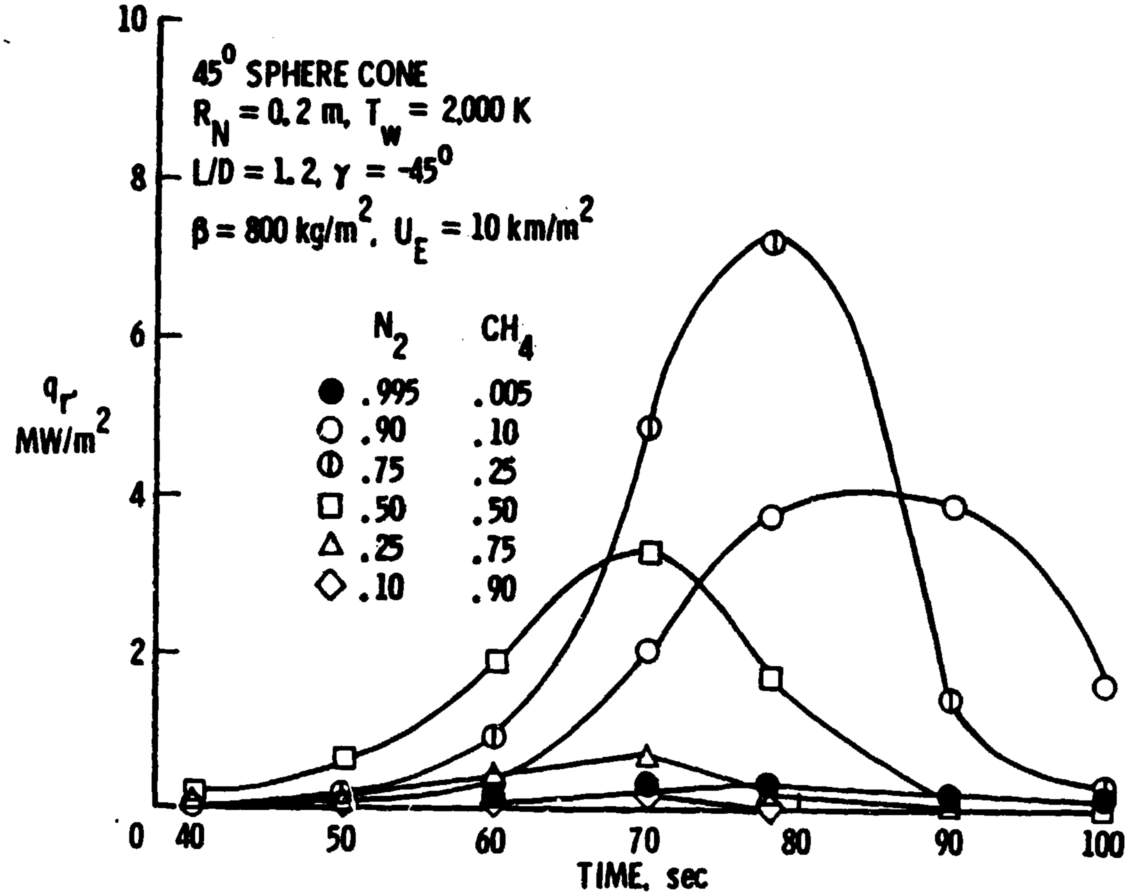

(a)

Figure 12. Effect of gas composition on stagnation-point radiative heating.

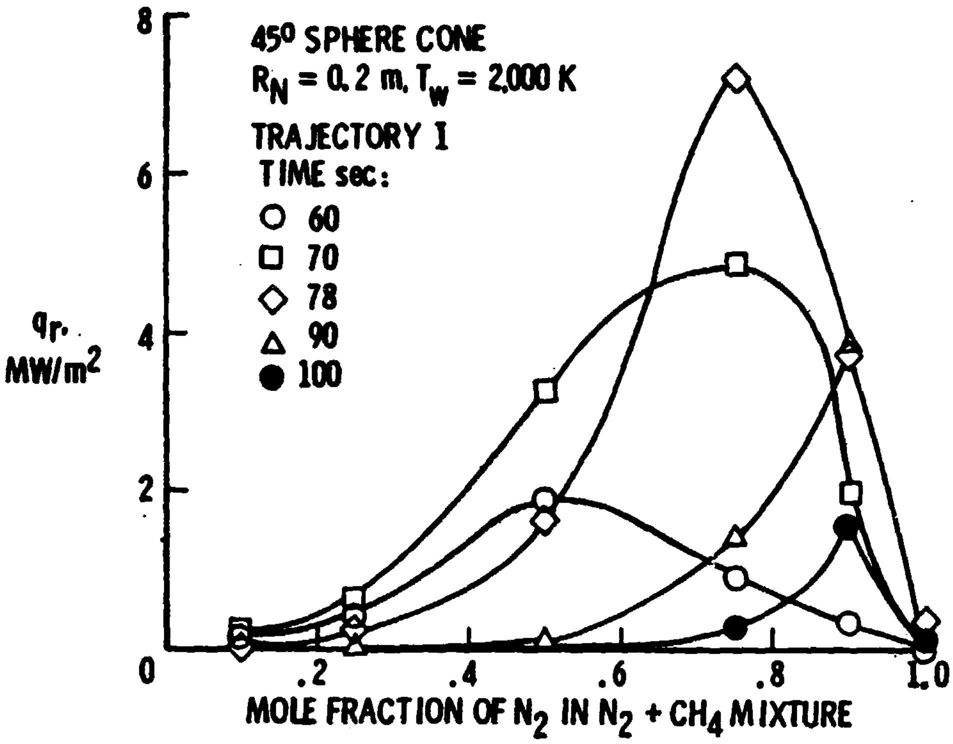

(b)

Figure 12. (Concluded.)

12(a) and (b)], i.e.) the radiative heating does not necessarily increase with increasing N_2 concentration. This is because, for a given set of conditions, the radiative transfer strongly depends on the presence of absorbing-emitting species in the gas mixture. It is also evident from figures 12(a) and (b) that the peak radiative heating occurs at different entry times for different free-stream gas compositions. For N_2 concentrations between 50% and 90%; the maximum heating is noted for 75% N_2 concentration. The free-stream compositions of 99.5% N_2 + 0.5% Ch_4 and 98% N_2 + 2% CH_4 are considered to be the realistic compositions for Titan's atmosphere. The results for stagnation-point shock temperature and convective and radiative heatings are illustrated in figure 13 for Trajectory I and for 99.5% N_2 + 0.5% CH_4. It is noted that for this case, the radiative heating is negligible as compared to the convective heating. The radiative heating is not more than seven percent of the total heating.

The effect of entry velocity on the stagnation-point shock temperature and convective and radiative heating rates are illustrated in figures 14 to 16. For the free-stream gas composition of 90% N_2 + 10% CH_4, the results presented in figures 14(a), 15(a) and 16(a) show that the shock temperature and heating rates, in general, increase with increasing entry velocity for a fixed entry altitude (time). It is seen that the extent of convective heating is considerably higher than the radiative heating for all cases. The results also show a similar trend for the gas composition of 99.5% N_2 + 0.5 CH_4 [figs. 14(b), 15(b), and 16(b)]. For this gas composition, the radiative heating is negligible in comparison to the convective heating. One exception to this, however, is noted from the results presented in figure 16(b). The radiative heating rate for an entry velocity of 13 km/s is considerably higher than for other velocities. Thus, for the entry speed of 13 km/s (and for an entry time between 30 and 60 s), it is possible to have physical conditions in the shock layer to produce a higher concentration of radiating species.

For the free-stream atmospheric composition of 90% N_2 + 10% CH_4, the results for stagnation-point convective and radiative heating are shown in figure 17 (and also in table 14 for Trajectories I and II). The results

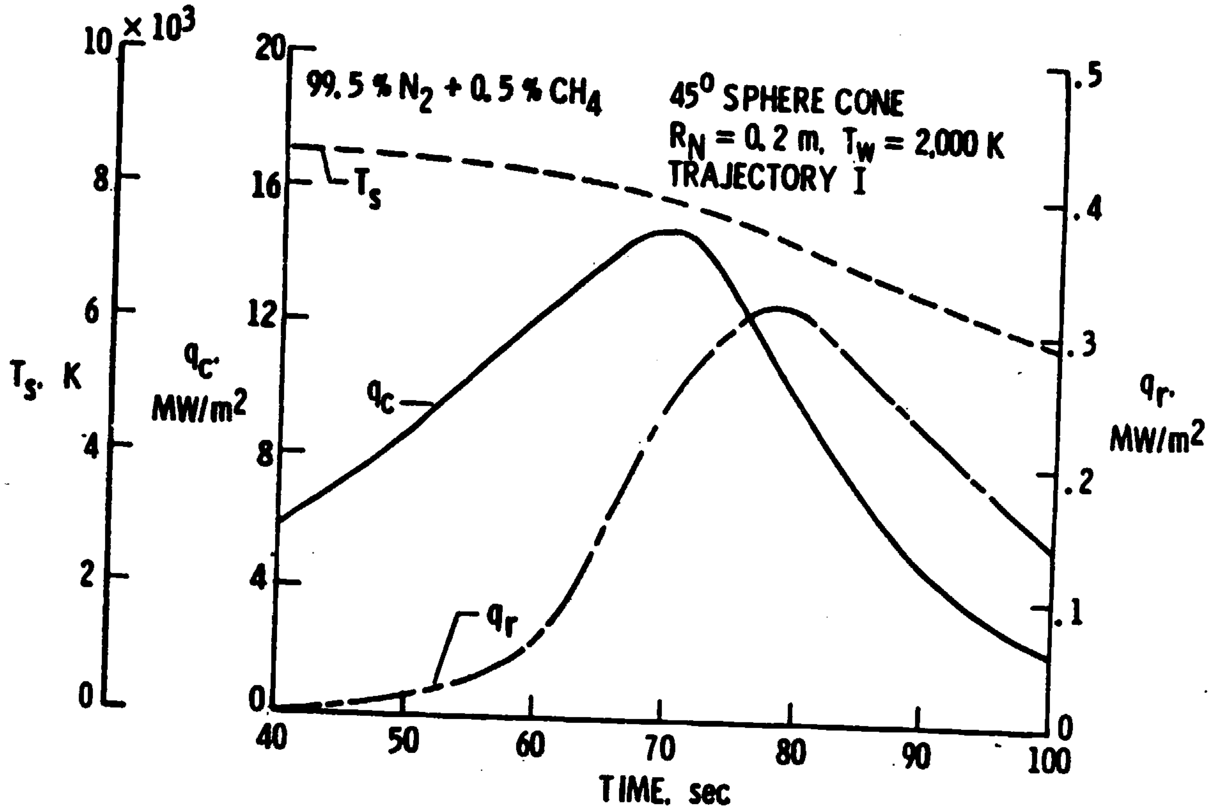

Figure 13. Variation of stagnation-point shock temperature and convective and radiative heating for 99.5% N_2 + 0.5% CH_4.

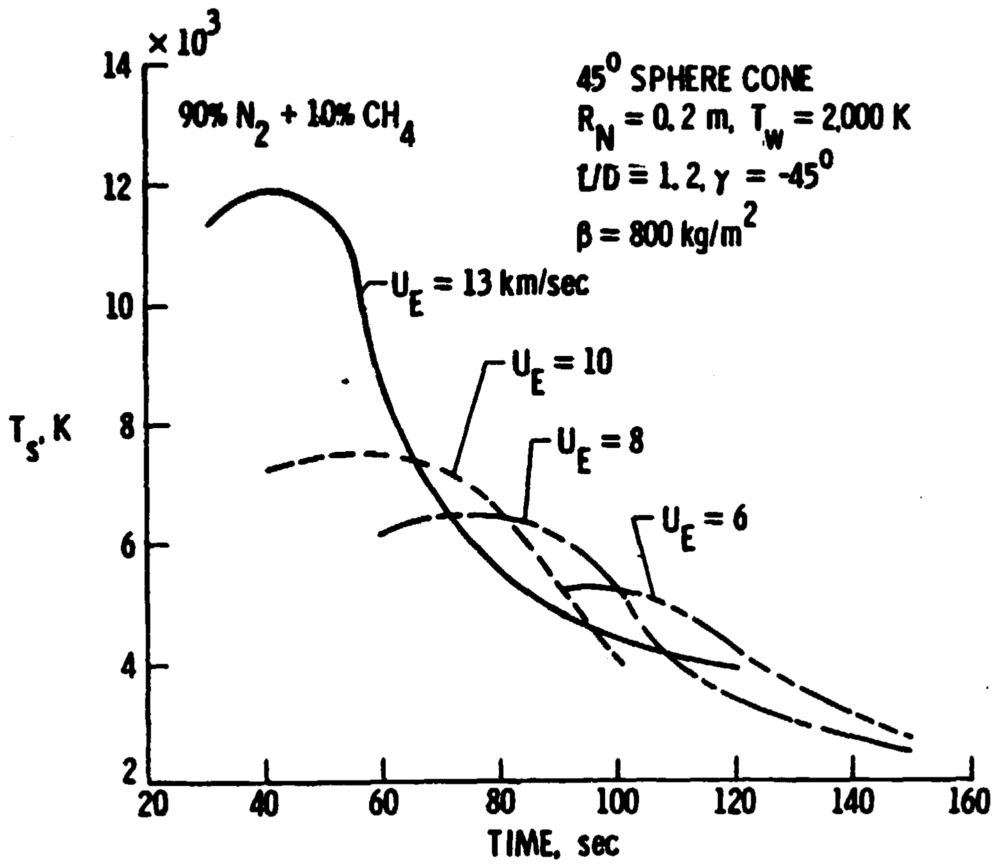

Figure 14(a). Effect of entry velocity on stagnation-point shock temperature, 90% N_2 + 10% CH_4.

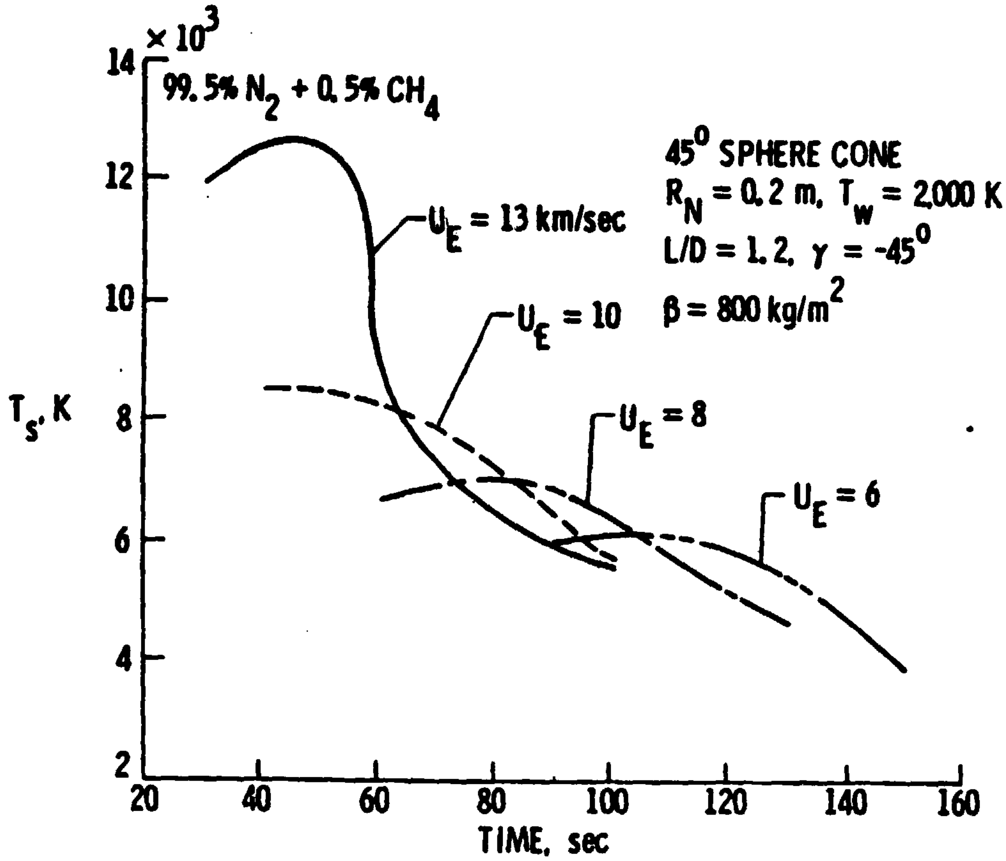

Figure 14(b). Effect of entry velocity on stagnation-point shock temperature, 99.5% N_2 + 0.5% CH_4.

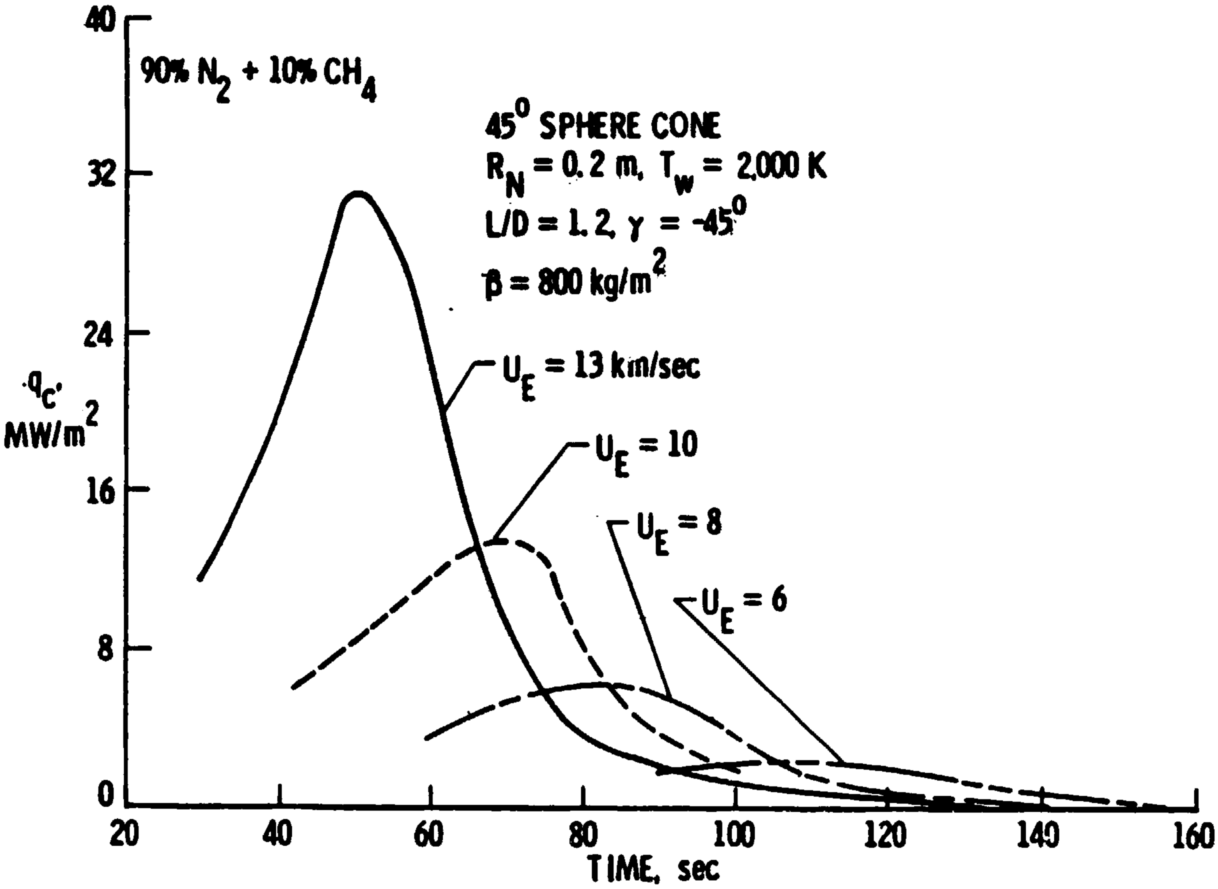

Figure 15(a). Effect of entry velocity on stagnation-point convective heating, 90% N_2 + 10% CH_4.

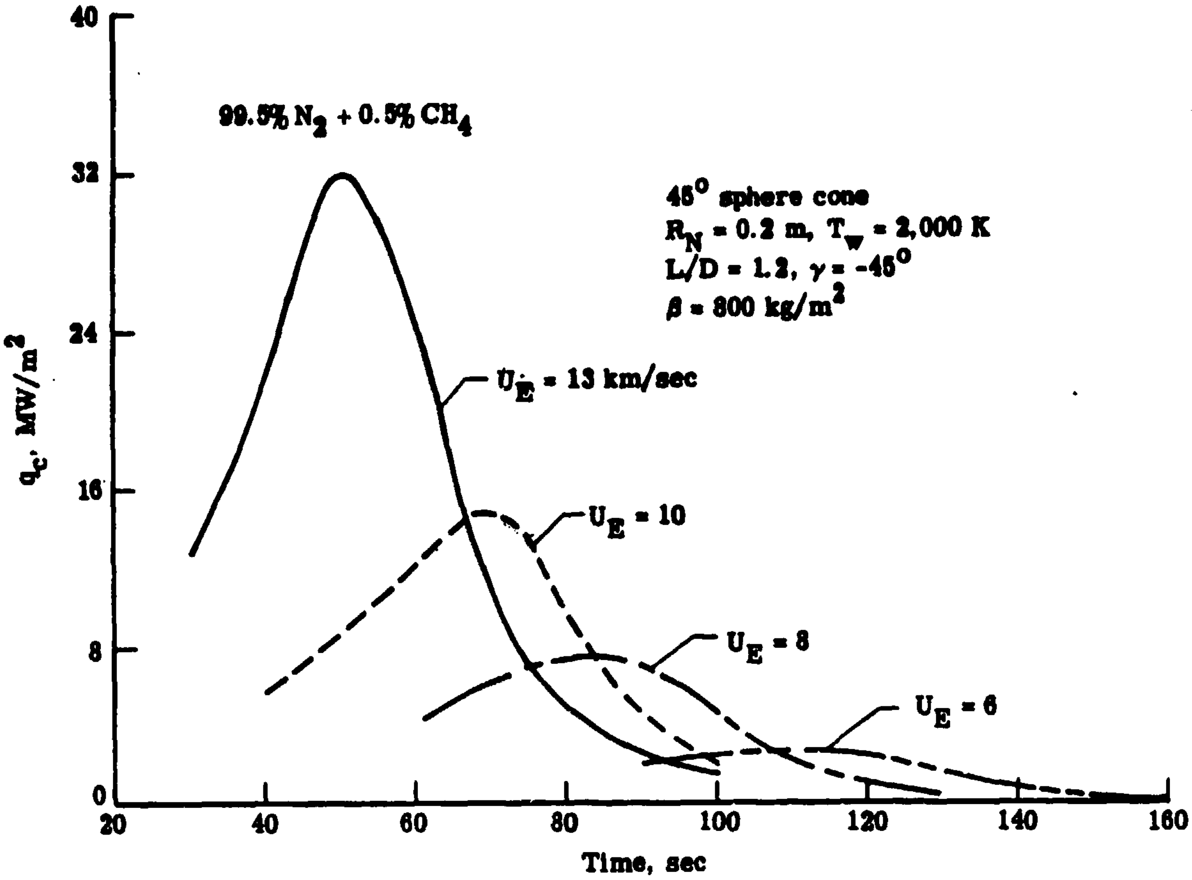

Figure 15(b). Effect of entry velocity on stagnation-point convective heating, 99.5% N_2 + 0.5% CH_4.

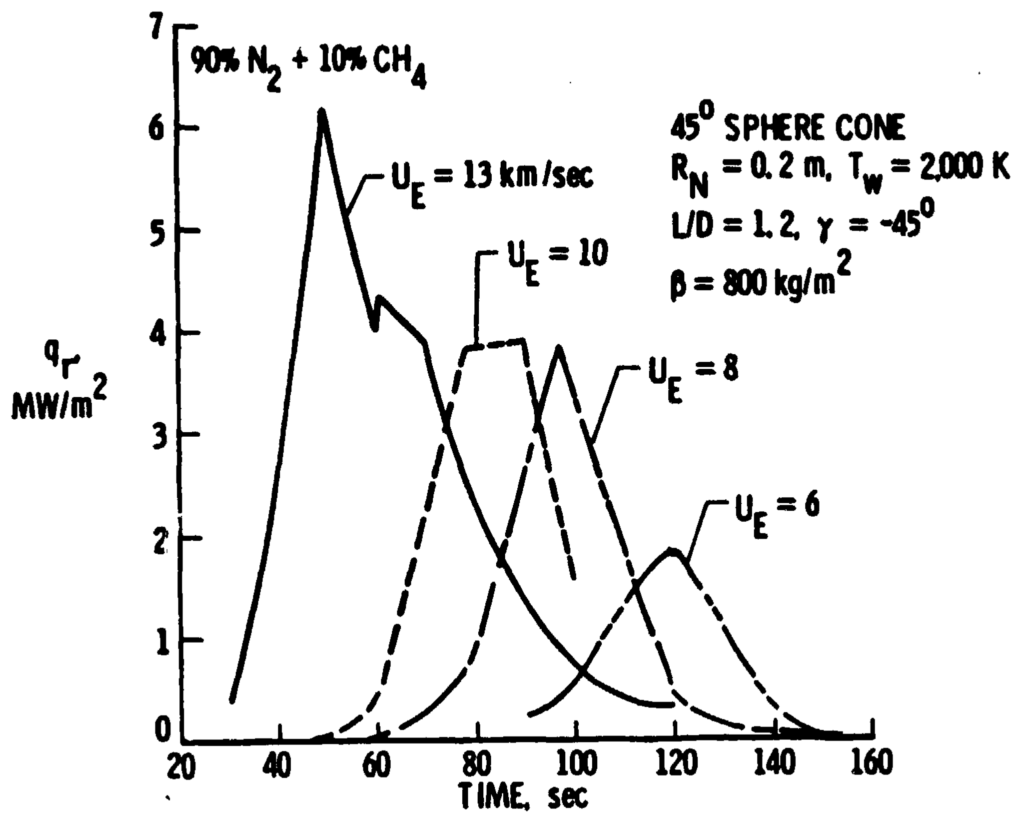

Figure 16(a). Effect of entry velocity on stagnation-point radiative heating, 90% N_2 + 10% CH_4.

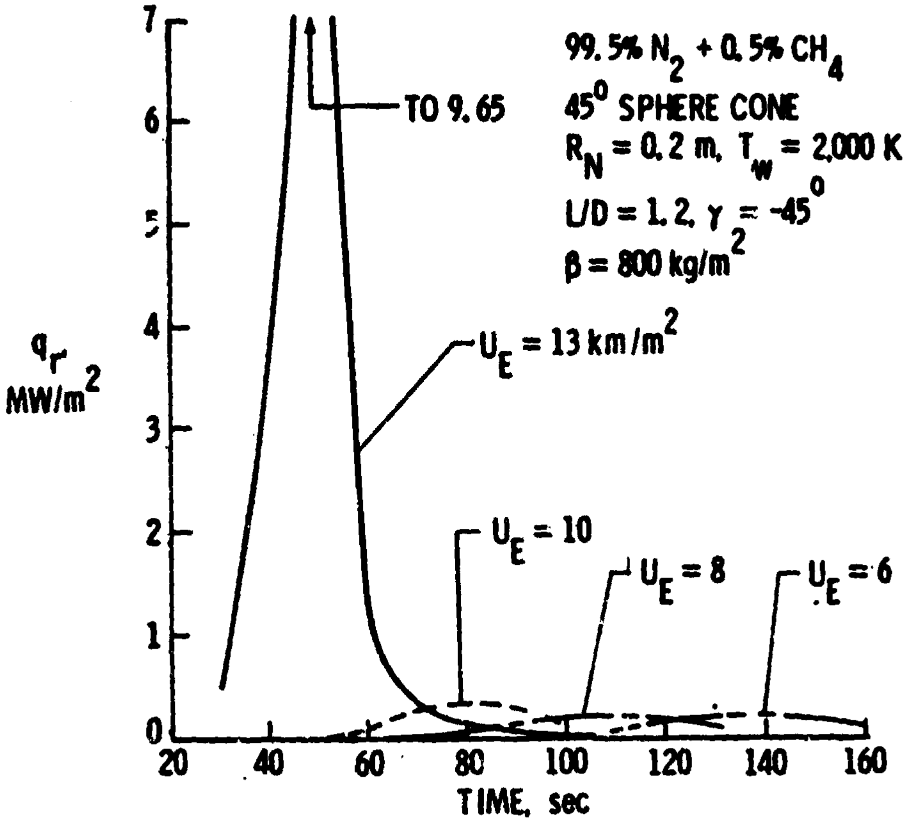

Figure 16(b). Effect of entry velocity on stagnation-point radiative heating, 99.5% N_2 + 0.5% CH_4.

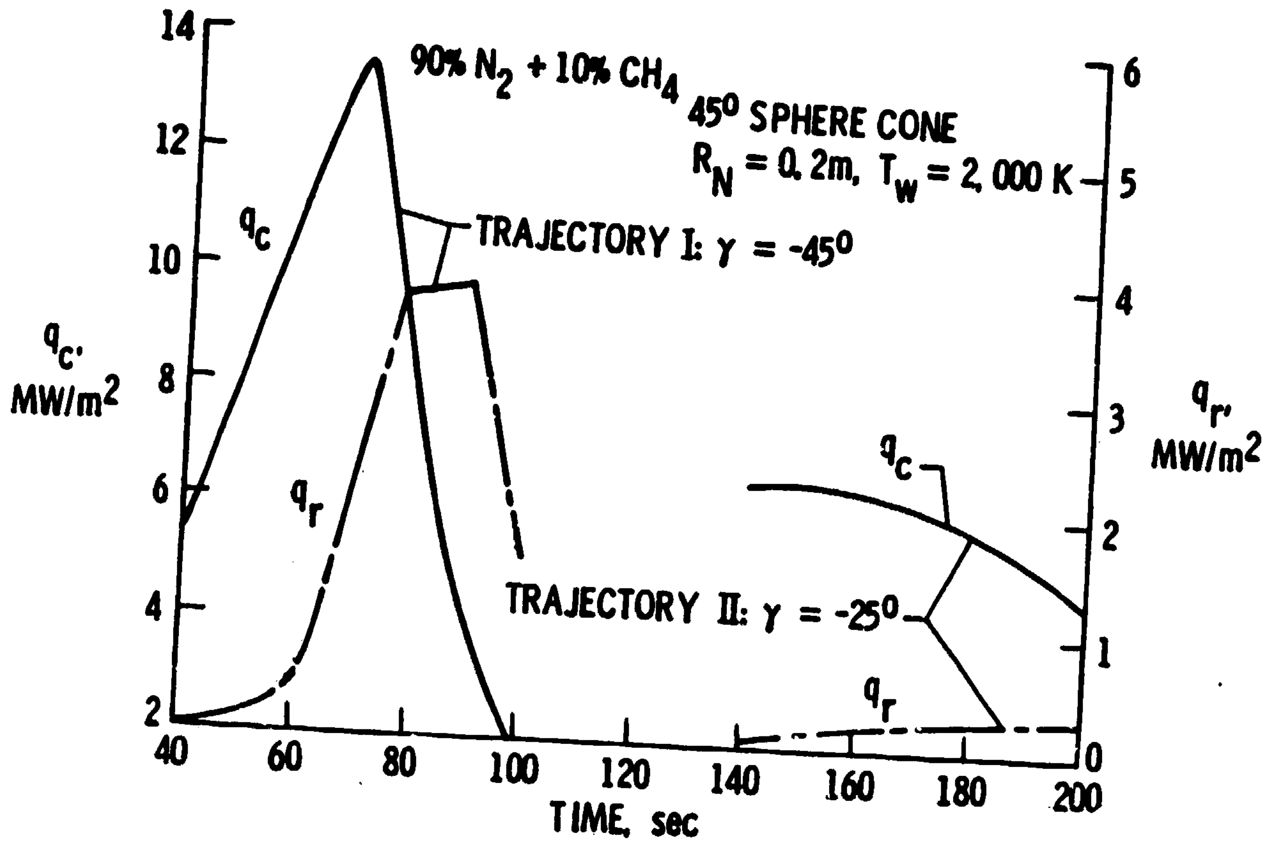

Figure 17. Variation of stagnation-point convective and radiative heating for Trajectories I and II, 90% N_2 + 10% CH_4.

show that the extent of both convective and radiative heating is considerably higher for Trajectory I (a steeper entry angle trajectory) than for Trajectory II. This, however, is expected since the rate of viscous dissipation will be higher for the steeper trajectory, resulting in a relatively higher shock temperature.

For the atmospheric composition of 99.5% N_2 + 0.5% CH_4, the variation of stagnation-point convective and radiative heating with body nose radius is given in figure 18 for Trajectory I and an entry time of 78 s (Z = 50.9 km). Although the extent of radiative heating is small, it is seen to increase with increasing nose radius. The convective heating rate, however, is seen to decrease with increasing nose radius. For a given set of entry conditions, the shock-standoff distance generally increases with increasing nose radius (ref. 4). This, in turn, results in different temperature, pressure, and species distributions in the shock layer. A combination of these changes influences the trend exhibited.

The results of heating rate along the body are illustrated in figures 19 and 20 for Trajectory I and for the entry conditions at 78 s. Variations in shock temperature and heating rates are shown in figure 19 for the atmospheric composition of 99.5% N_2 + 0.5% CH_4. The results show that both convective and radiative heating essentially follow the trend of the shock temperature from the stagnation point to the tangency point (at about $S/R_N^* =$ 0.8). Beyond this point, the convective heating continues the same trend, but the radiative heating is seen to increase with the body location. This is because the pressure and temperature conditions near such location are conducive for production of the radiating CN species over a large portion of the shock-layer thickness (see fig. 5), and also because the optical thickness of the shock-layer gas is relatively higher in the downstream regions. The variation in heating rates along the body is illustrated in figures 20(a) and 20(b) for the cases with and without CN concentration in the shock-layer gas. The results show that while the presence of CN has little influence on the convective heating, the radiative heating is increased considerably by its presence. It is important to note that after the tangency point, the rate of radiative heating in the presence of CN is significantly higher than the convective heating for the free-stream composition

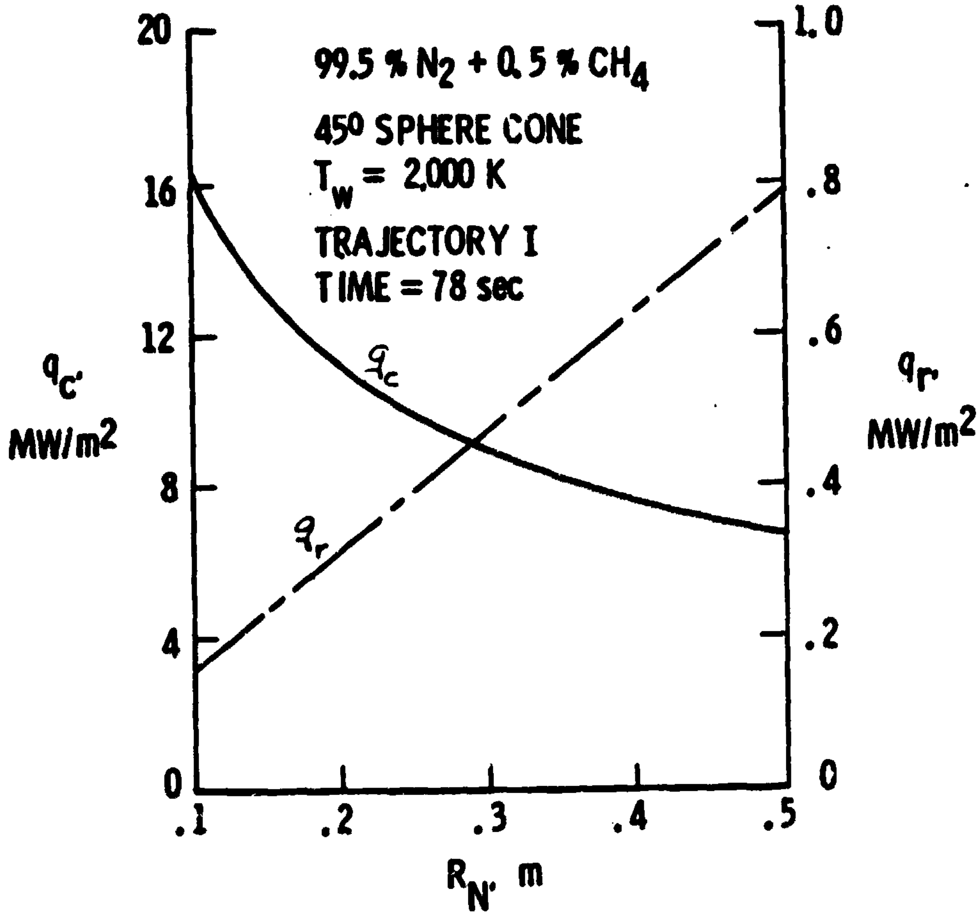

Figure 18. Effect of body nose radius on stagnation-point convective and radiative heating for 99.5% N_2 + 0.5% CH_4, t = 78 s.

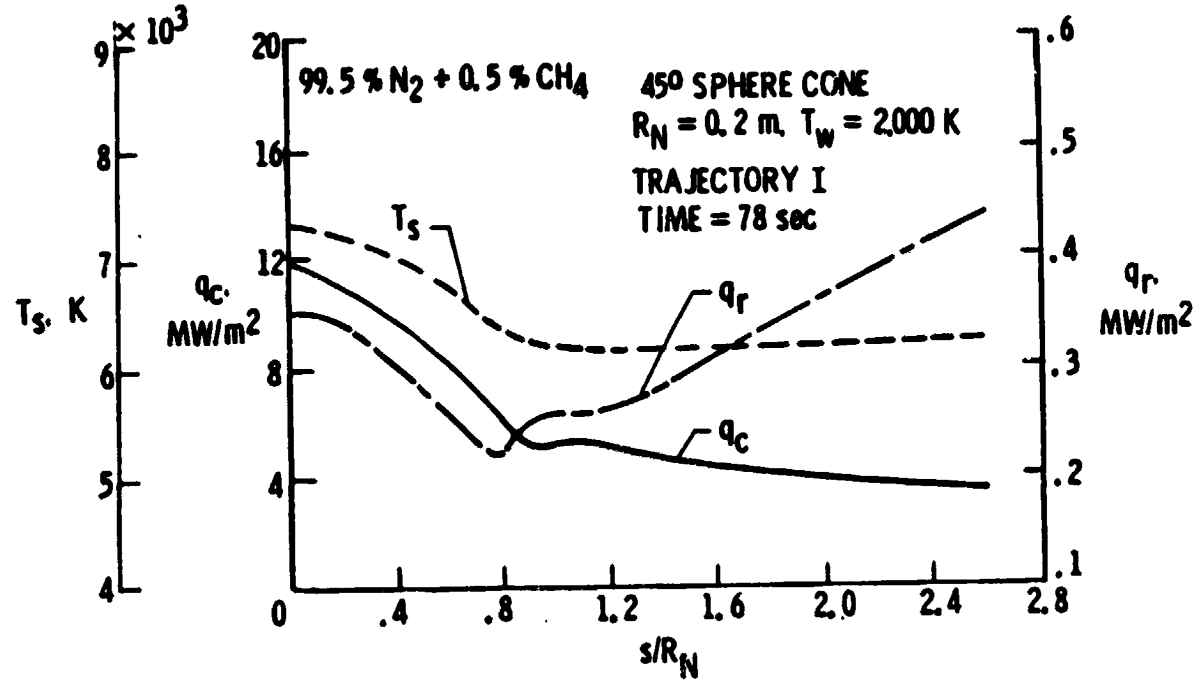

Figure 19. Variation of shock temperature, convective and radiative heating along the body for 99.5% N_2 + 0.5% CH_4.

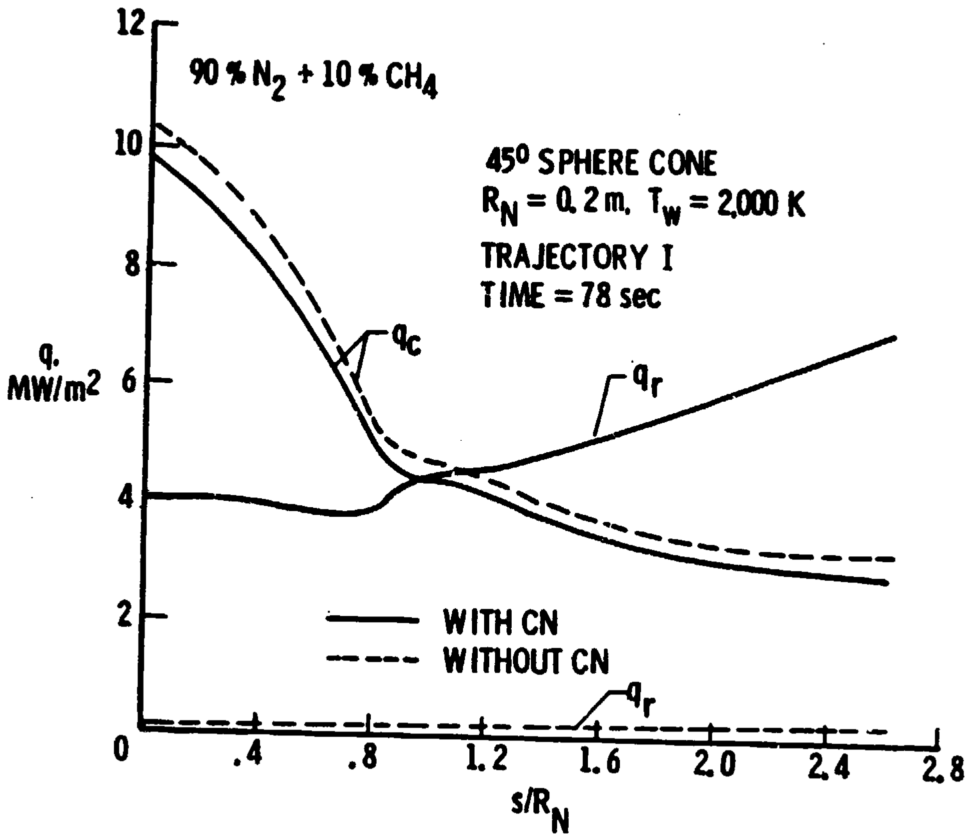

Figure 20(a). Influence of CN on convective and radiative heating along the body for t = 78 s and 90% N_2 + 10% CH_4.

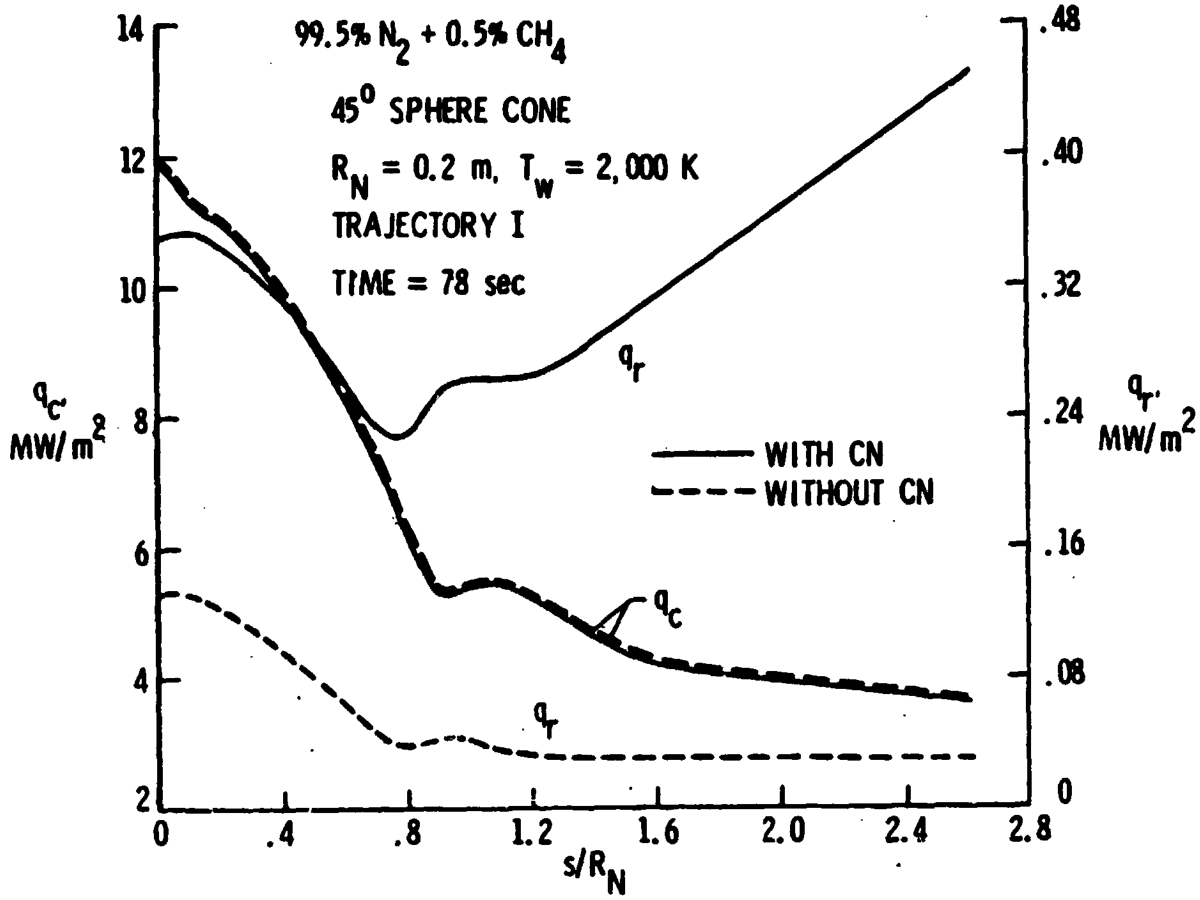

Figure 20(b). Influence of CN on convective and radiative heating along the body for t = 78 s and 99.5% N_2 + 0.5% CH_4.

of 90% N_2 + 10% CH_4 [(fig. 20(a)]. The same trend is seen in figure 20(b) for the atmospheric composition of 99.5% N_2 + 0.5% CH_4, but the extent of radiative heating is considerably small.

For the free-stream atmospheric composition of 99.5% N_2 + 0.5% CH_4, variations in important results with distance along the body surface are illustrated in figures 21 to 23 for Trajectory I and for critical entry times (altitudes). The results for shock density and shock-standoff distance presented in figure 21 show that, for a given entry altitude, the shock-standoff distance increases as density decreases. The shock-standoff distance is seen to decrease with increasing altitude; this is because higher free-stream velocities are associated with higher altitudes (see table 1). The results for shock temperature and enthalpy presented in figure 22 show that both decrease along the body until the tangency point, and they remain essentially constant beyond that point. Because of higher free-stream velocities, the shock temperature and enthalpy are greater for higher altitudes. The variation in heating rates is shown in figure 23. As discussed earlier, the peak convective heating occurs for entry conditions at $t = 70$ s ($z = 70.4$ km) and peak radiative heating at $t = 78$ s ($z = 50.9$ km). These results clearly show that the radiative heating is not important in the stagnation region if Titan's atmospheric composition is considered to be 99.5% N_2 + 0.5% CH_4.

Trajectory VI is the latest trajectory specified for the Titan mission, and there appears to be a general agreement to consider the atmospheric composition as 98% N_2 + 2% CH_4. Results for this case are shown in figures 24 and 25. The results for stagnation-point shock temperature, enthalpy, and convective and radiative heating rates are shown in figure 24 for different entry times. The results show that the extent of radiative heating for this trajectory is small compared to the convective heating. It is noted that the radiative peak heating occurs at an entry time of 70 s ($Z = 204.570$ km), whereas the convective peak heating (20.276 MW/m^2) occurs at 73 s ($Z = 196.349$ km). The variations in shock temperature, shock density, shock-standoff distance, and heating rates along the body are shown in figure 25 for an entry time of 73 s. These results exhibit essentially the same trend as noted in figures 19 and 21 for Trajectory I with 99.5% N_2 + 0.5% CH_4.

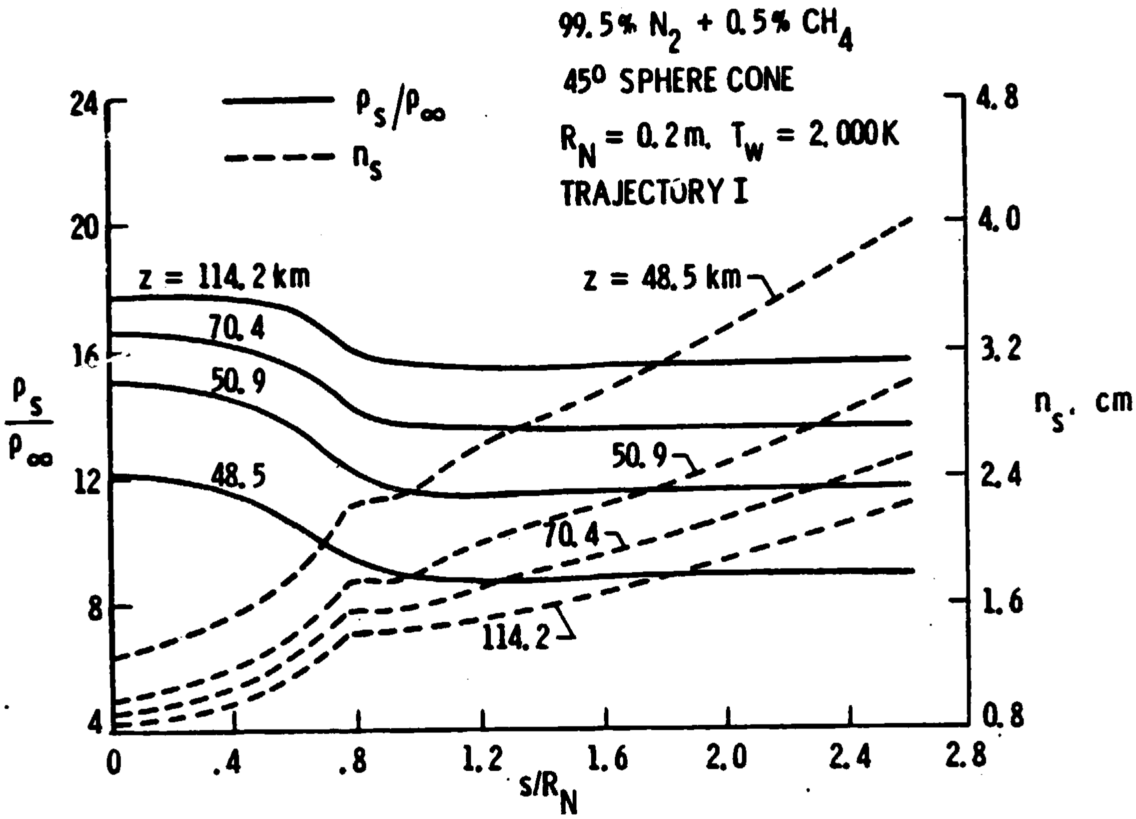

Figure 21. Variation of shock density and shock-standoff distance with body coordinate for 99.5% N_2 + 0.5% CH_4.

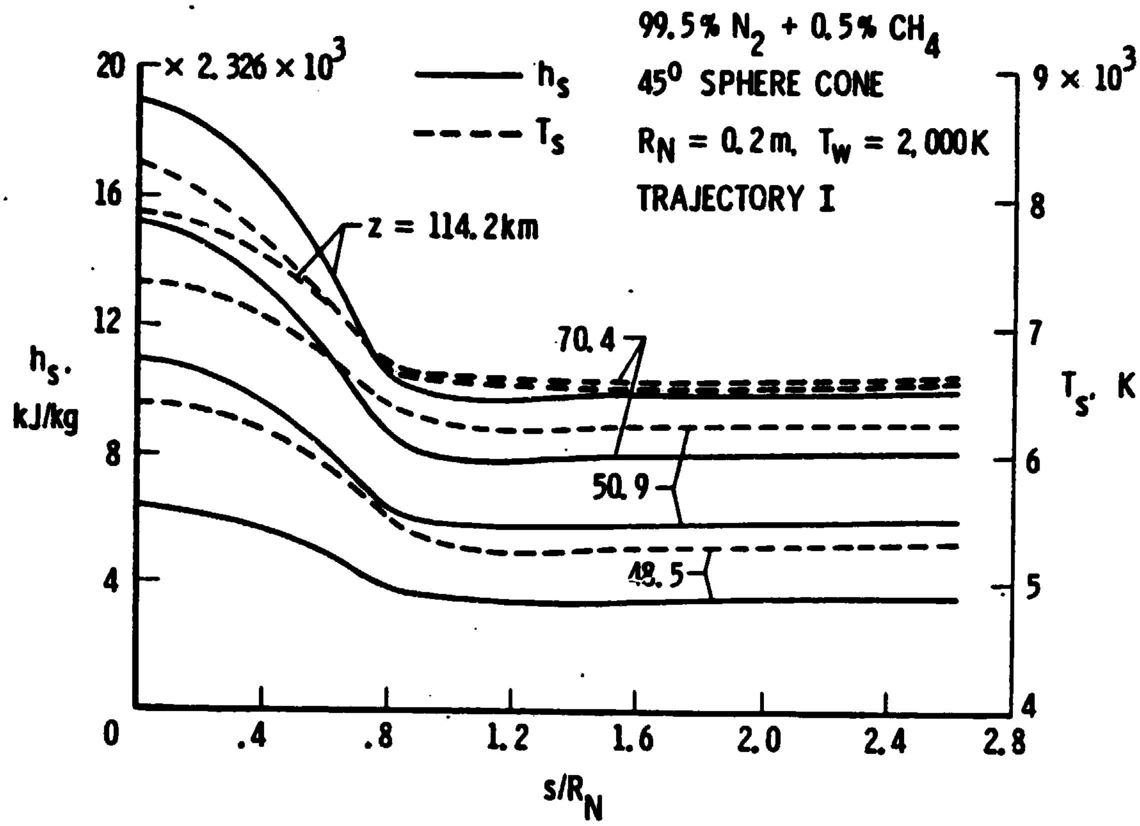

Figure 22. Variation of shock temperature and enthalpy with body coordinate for 99.5% N_2 + 0.5% CH_4.

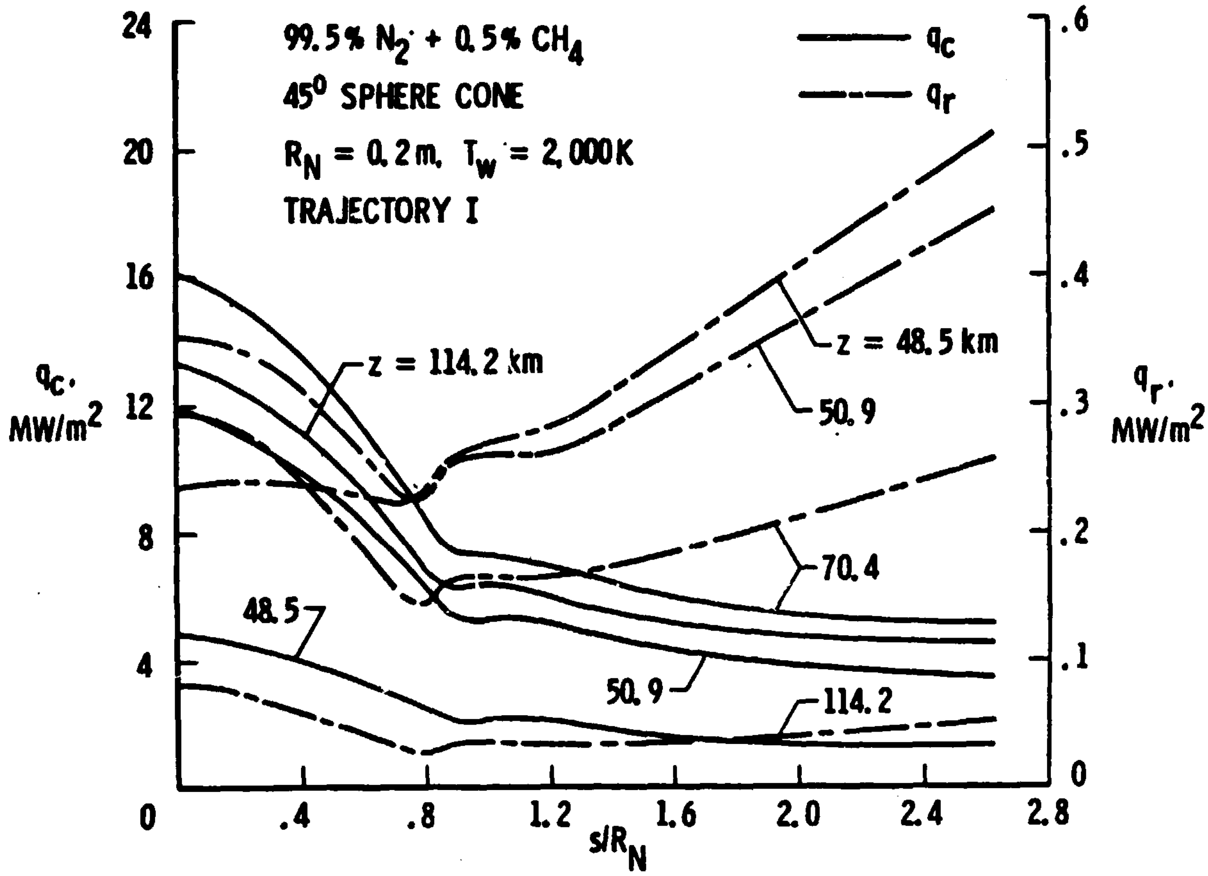

Figure 23. Variation of convective and radiative heating along the body for 99.5% N_2 + 0.5% CH_4.

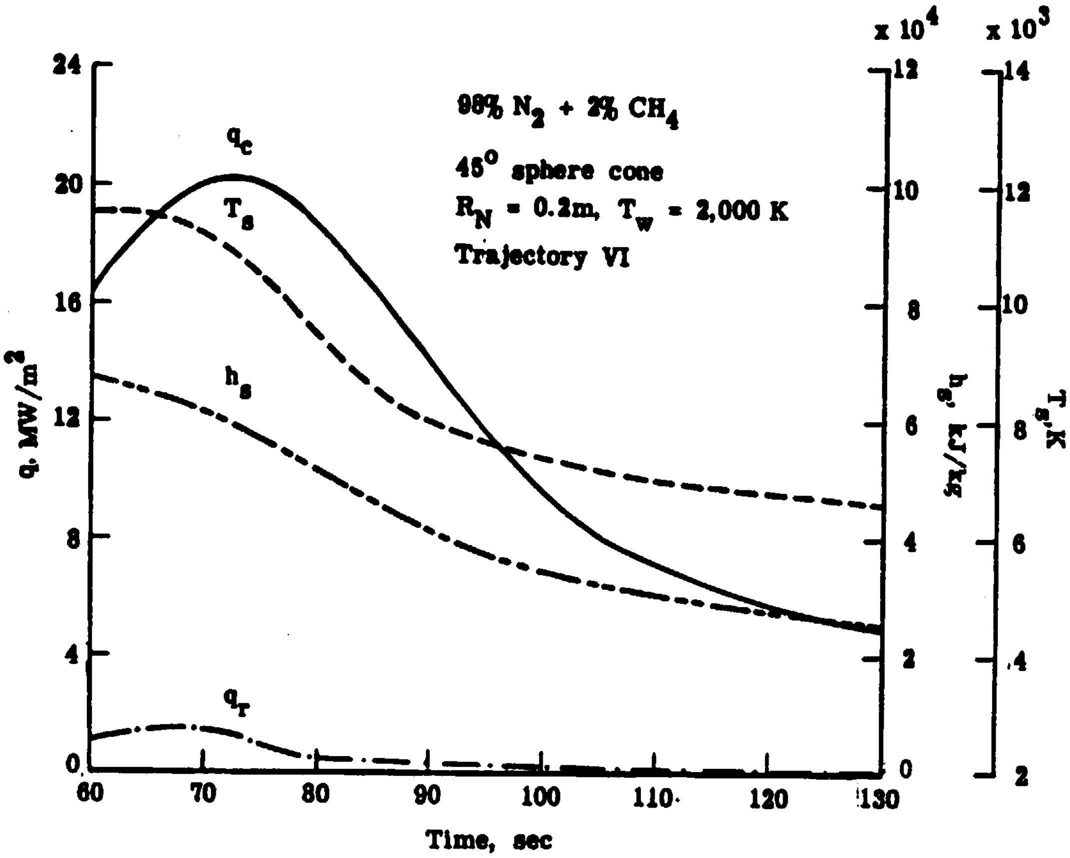

Figure 24. Variation of stagnation-point shock temperature, enthalpy, and convective and radiative heating for Trajectory VI, 98% N_2 + 2% CH_4.

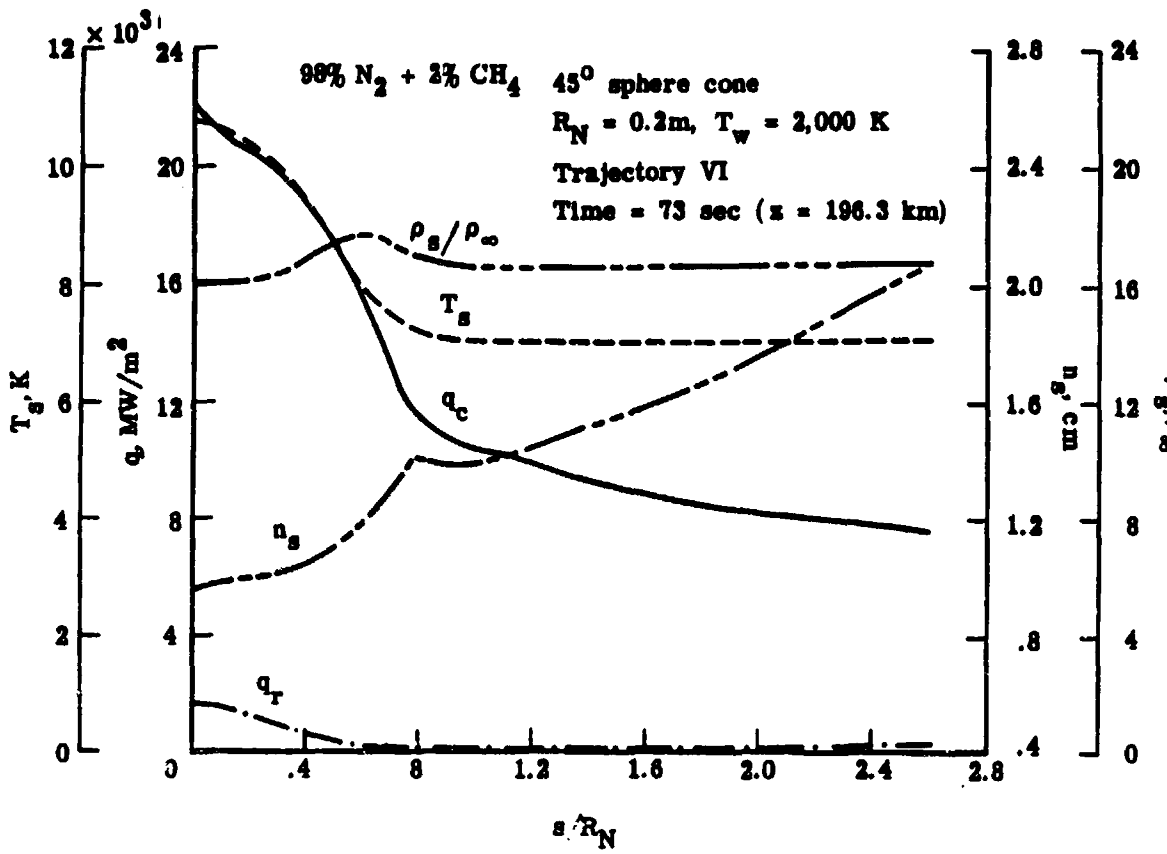

Figure 25. Variation of shock temperature, shock density, shock-standoff distance, and convective and radiative heating along the body for Trajectory VI, 98% N_2 + 2% CH_4.

Thus, for atmospheric compositions with very high N_2 concentration, the radiative heating is not important in the stagnation region.

The extent of convective and radiative heating over the entire length of the aerocapture vehicle is shown in figure 26 for the free-stream gas composition of 90% N_2 + 10% CH_4 and 98% N_2 + 2% CH_4. For the free-stream composition of 90% N_2 + 10% CH_4, the results clearly show that, while the convective heating rate continues to decrease in the downstream region, the radiative heating rate is considerably higher in this region. As discussed before, the reason for this trend is the combined influence of shock-temperature density and pressure variations in this region and the relatively higher optical thicknesses of the radiating shock layer. A similar trend in heating rates is noted also for the gas composition of 98% N_2 + 2% CH_4, but the extent of radiative heating is found to be relatively lower. However, it is important to note that the radiative heating approaches the convective heating in the downstream region.

To investigate the effects of body and shock slip conditions on the entire shock-layer flow phenomena, the results were obtained for the recently specified Trajectory IV (Table 6), with a free-stream atmospheric composition of 98% N_2 + 2% CH_4. Since chemical equilibrium is assumed and the thickness effect is of higher order, the concentration slip and thickness effects were neglected in this study. The results were obtained specifically for the higher altitude entry conditions where the influence of slip conditions was anticipated. Some important results of this investigation are presented here. In discussion of these results (and in figures), the word "slip" implies both the body and shock slip conditions. Results are presented first for the velocity slip and temperature jump at the body surface. Following this, results are presented for the properties immediately behind the shock. Next, the effects of slip conditions on the temperature distribution in the shock layer and on the convective heating along the body are discussed. The results are then presented for selected entry altitudes to show the separate effects of body and shock slip conditions on the convective heating along the body. Finally the results are presented for the temperature distribution and convective heating for very high entry altitudes.

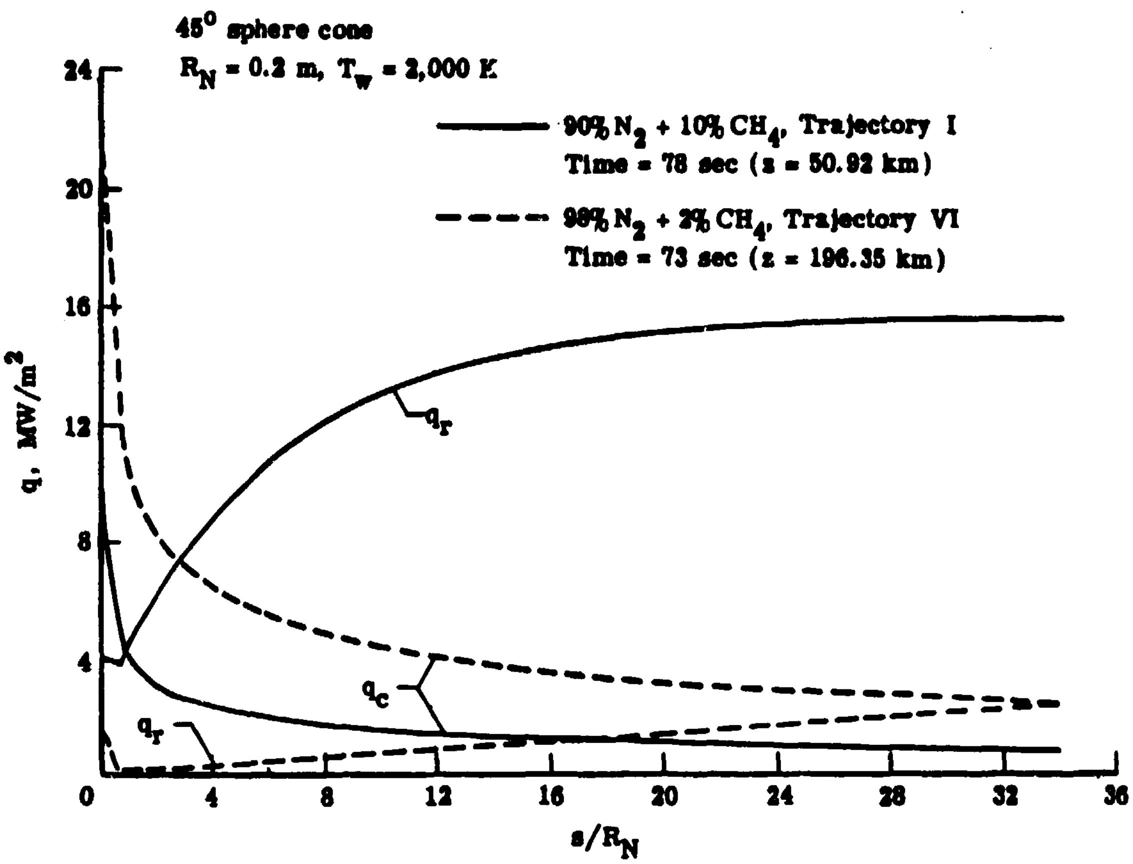

Figure 26. Variation of convective and radiative heating along the body for Trajectory I, 90% N_2 + 10% CH_4 (t = 78 s), and Trajectory VI, 98% N_2 + 2% CH_4 (t = 73 s).

The variation in the surface-slip velocity is illustrated in figure 27 as a function of the entry time. The results clearly illustrate that the condition of no slip is not satisfied at higher altitudes (earlier entry time). The magnitude of velocity slip ($u_{w,s}$) is expressed as a percent of the velocity just behind the shock. It is evident from the figure that about 7 percent velocity slip occurs at the entry time of 20 s (Z = 465.115 km), and only 0.12 percent at the entry time of 73 s (z = 196.349 km).

The temperature jump and enthalpy change at the body surface are shown in figure 28 for different entry altitudes. The body surface temperature was taken to be 2,000 K. A temperature jump of about 1.2 times the surface temperature (i.e, ΔT = 2,500 K) is seen along the body surface near the stagnation point for entry altitude Z = 465.115 km. At lower altitudes, however, the temperature jump is seen to be relatively smaller. For example, at Z = 196.349 km the temperature jump is about 150 K. A similar trend is noted for enthalpy change at the body surface.

Figures 29 to 32 show the velocity slip, temperature jump, enthalpy change, and density change just behind the shock. The results illustrated in figure 29 show that both the u and v velocity components are influenced by the slip conditions. It is evident from figures 30 to 32 that, when the altitude is lower than 402.595 km, the effects of slip conditions are not important. However, a significant temperature jump is noted at Z = 465.115 km (see fig. 30). Since both the temperature and velocity components decrease just behind the shock, the slip conditions result in a decrease in enthalpy and an increase in density; these are clearly evident from the results in figures 31 and 32.

The temperature distribution in the shock layer, along the stagnation streamline, is shown in figure 33 for different altitude entry conditions. It is evident from the figure that, when the altitude is lower than 402.595 km, the effect of slip conditions is not important.

The effects of slip conditions on the convective heating along the body are shown in figure 34 for different entry conditions. The effects are seen to be lower for lower altitudes. It is important to note that at lower

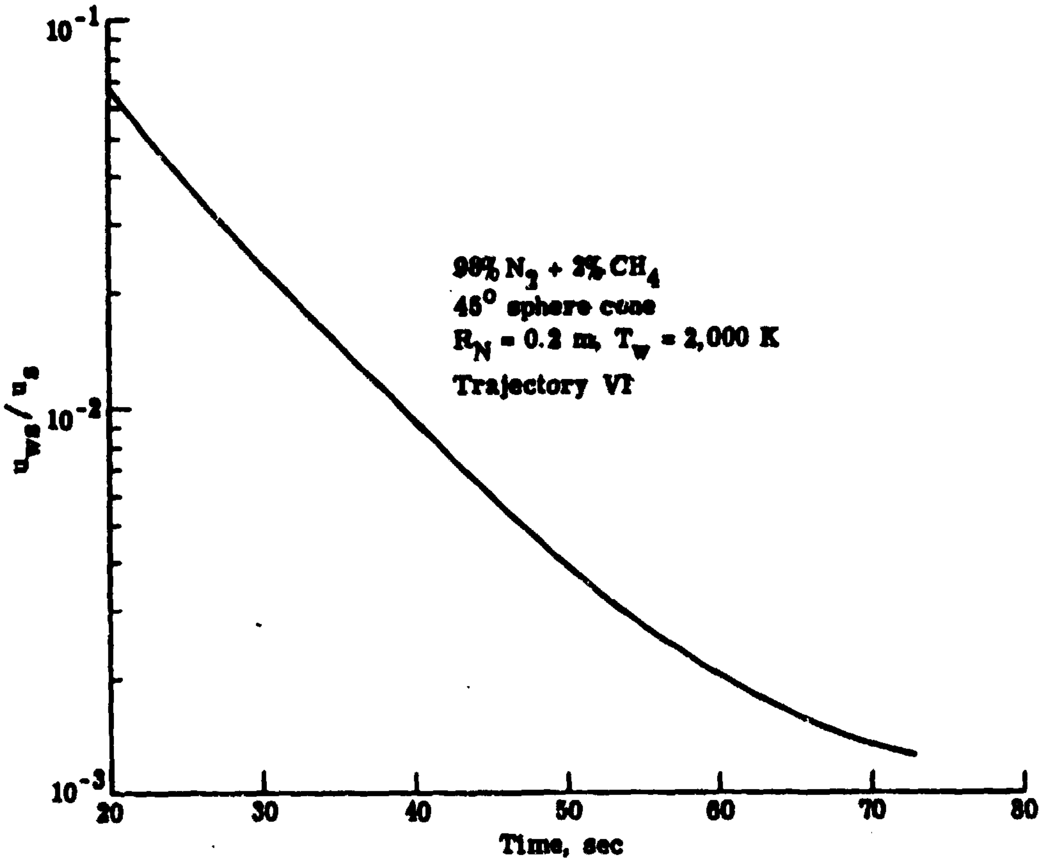

Figure 27. Velocity slip at the body surface as a function of entry time (altitude) on the stagnation point.

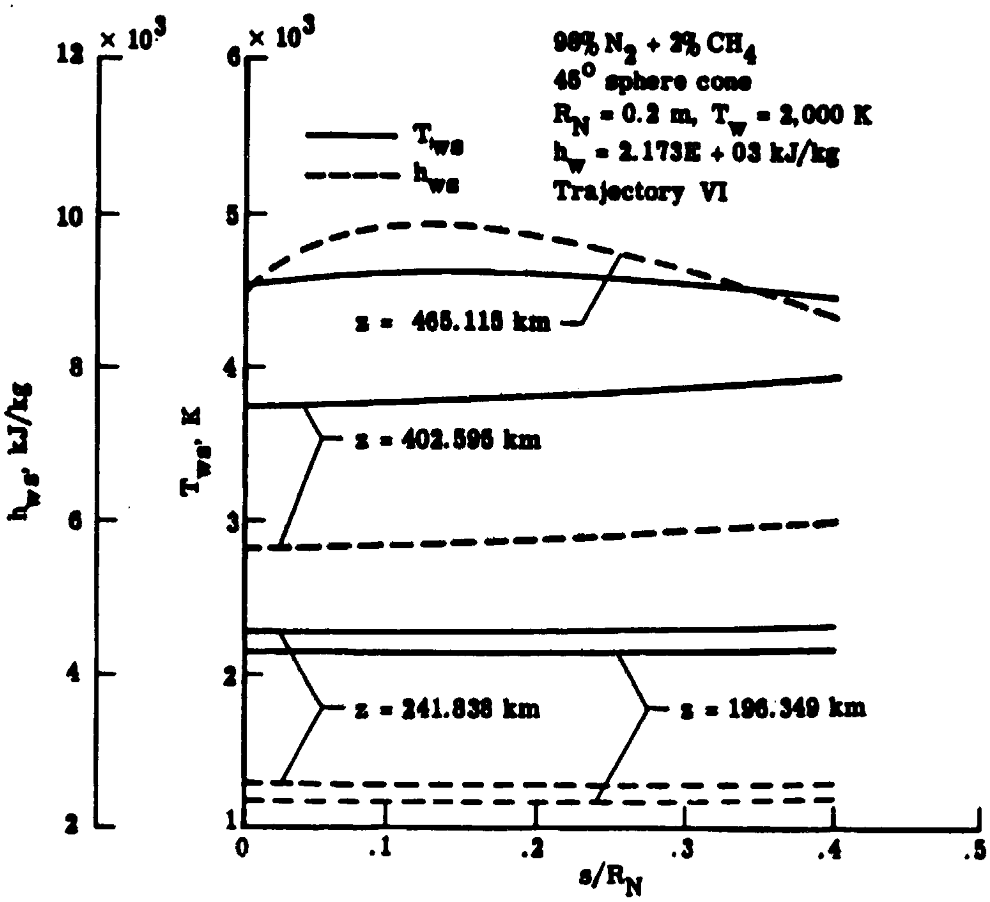

Figure 28. Temperature jump and enthalpy change along the body surface fcr different entry altitudes.

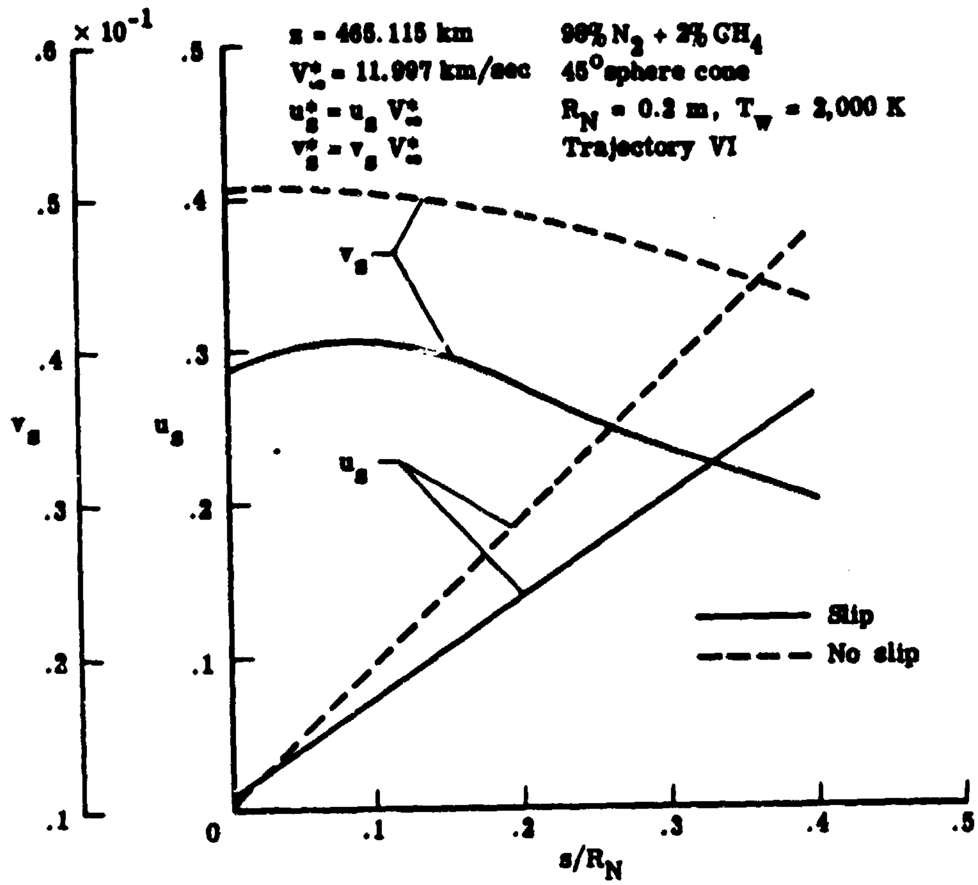

Figure 29. Velocity variation just behind the shock wave as a function of ξ coordinate.

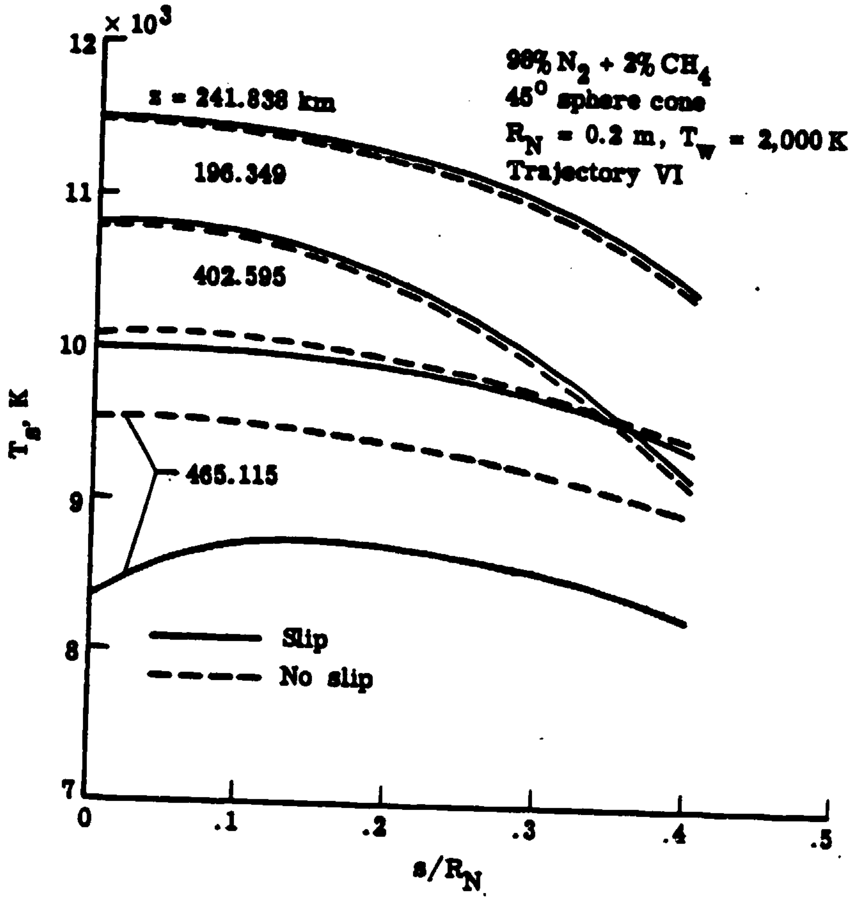

Figure 30. Temperature variation just behind the shock wave as a function of ξ coordinate for different entry altitudes.

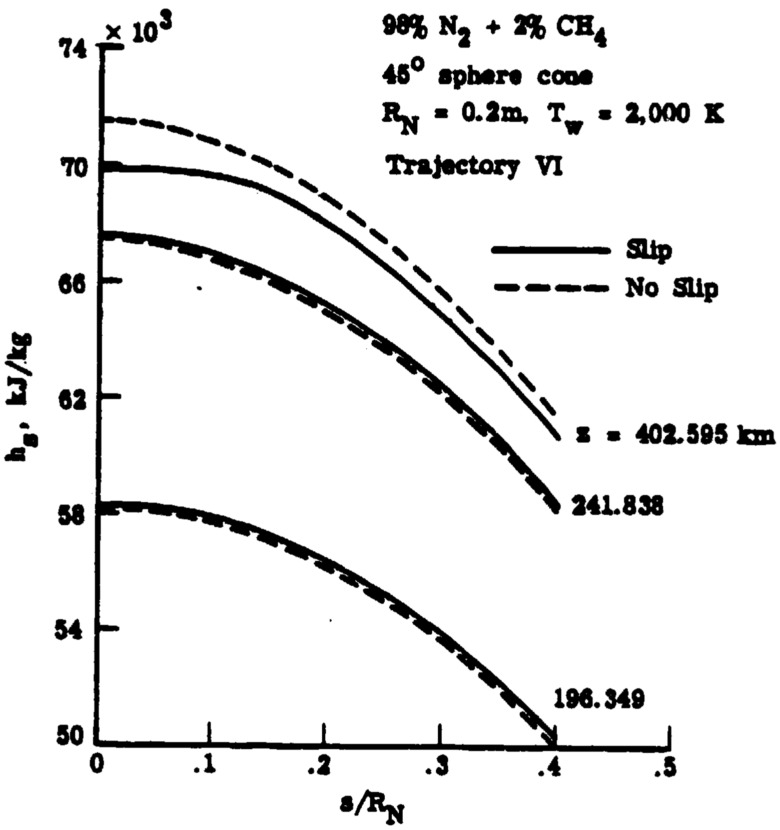

Figure 31. Enthalpy variation just behind the shock wave as a function of ξ coordinate for different entry altitudes.

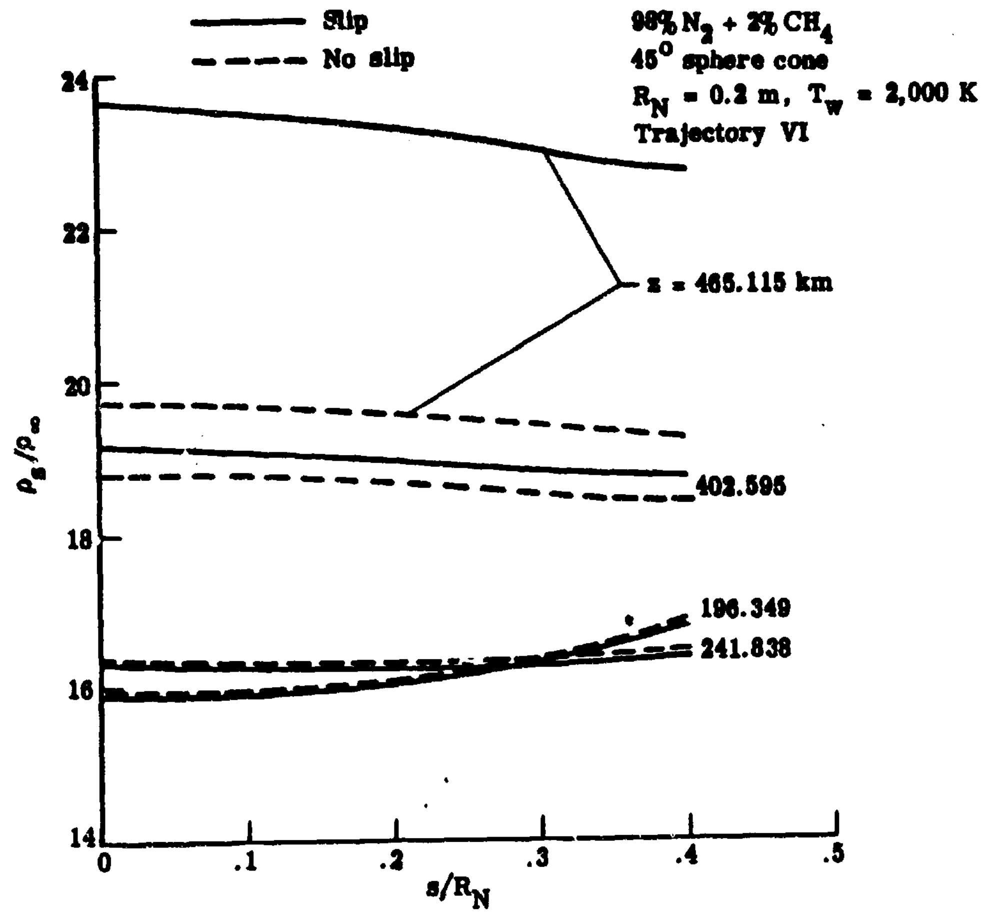

Figure 32. Density variation just behind the shock wave as a function of ξ coordinate for different entry altitudes.

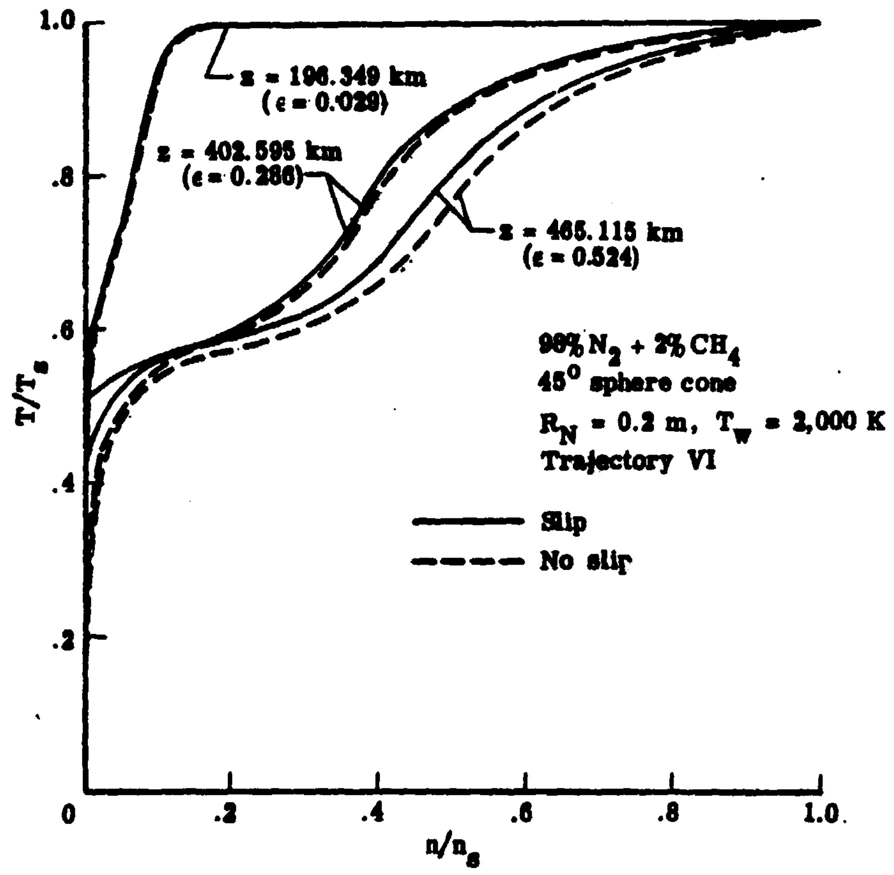

Figure 33. Temperature profile in the shock layer at stagnation point with slip conditions for different entry altitudes.

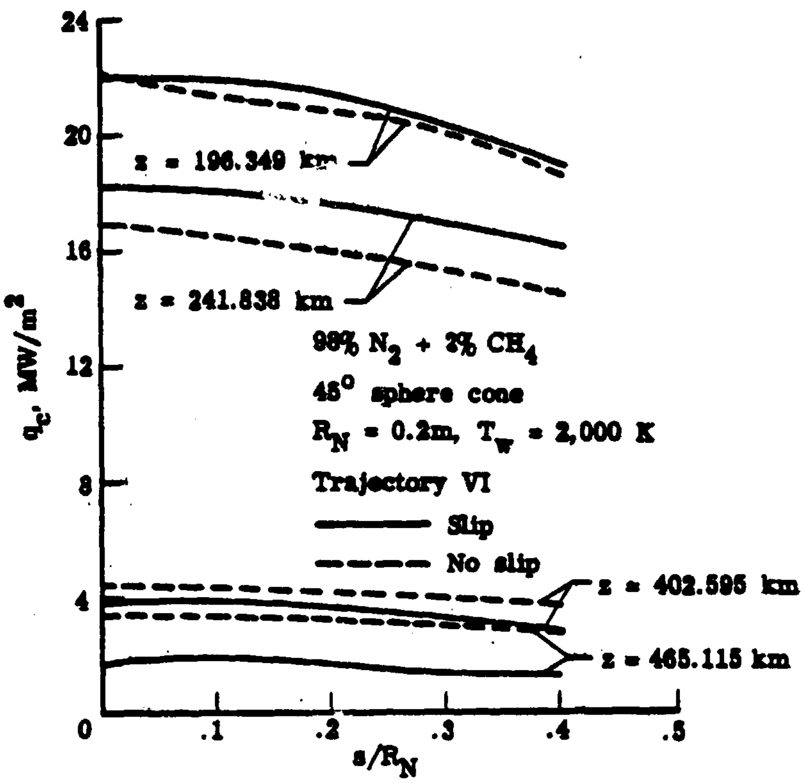

Figure 34. Variation of convective heating along the body surface for different entry altitudes.

altitudes the slip conditions result in an increase in the convective heating, whereas the reverse is true for the higher altitudes. For example, about a 1 percent increase in convective heating is noted for Z = 196.349 km and about 6 percent increase for Z = 241.838 km; however, a reduction of about 48 percent is observed for entry conditions at Z = 465.115 km.

Separate effects of the body and shock slips on the convective heating are shown in figures 35 and 36 along with the slip (body as well as shock slip) and no slip solutions. As would be expected, the results obtained by considering only the body or shock slip fall, in general, between the results of slip and no-slip conditions. The effects of slip, of course, are higher for higher altitude entry conditions. The results clearly indicate that both the body and shock slips are equally important in influencing the extent of convective heating to the body.

In order to assess the effets of slip conditions on the convective heating for very high entry altitudes, the results were obtained by considering only the body-slip conditions because of the computational convenience. The temperature distribution along the stagnation streamline is illustrated in figure 37 for entry conditions at Z = 497.656 km and Z = 531.004 km. The results show that, while the no-slip temperature distribution is essentially the same for both altitudes, the body-slip temperature distributions are entirely different. The wall temperature jump and convective heating variation along the body are illustrated in figure 38. These are seen to be influenced greatly by the slip-body conditions. For entry conditions at Z = 531.004 km, the results show a temperature jump of about 150 percent and a decrease in convective heating by about 30 percent.

The results for slip conditions clearly indicate that both the body and shock slip conditions should be included in analyzing the aerothermal environment of the Titan's aerocapture vehicle at higher entry altitudes. However, during most of the heating pulse (where the heating is significant compared with peak heating), this study indicates that accurate results can be obtained without including slip boundary conditions while using the assumption of equilibrium flow.

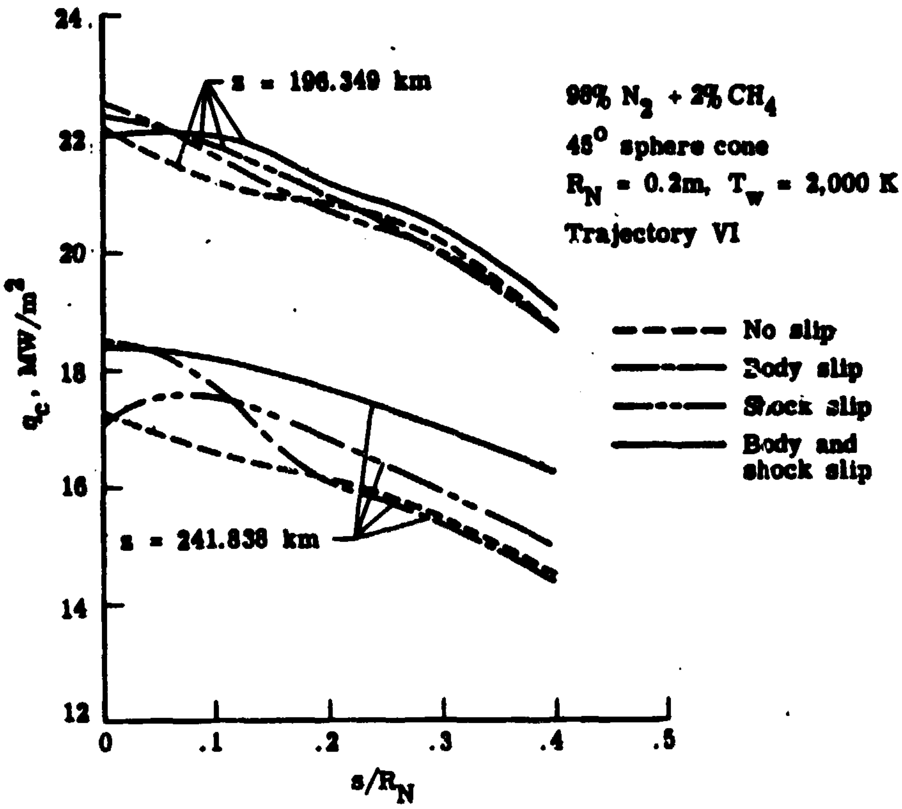

Figure 35. Variation of convective heating along the body for different slip condition at Z = 196.349 km and Z = 241.838 km.

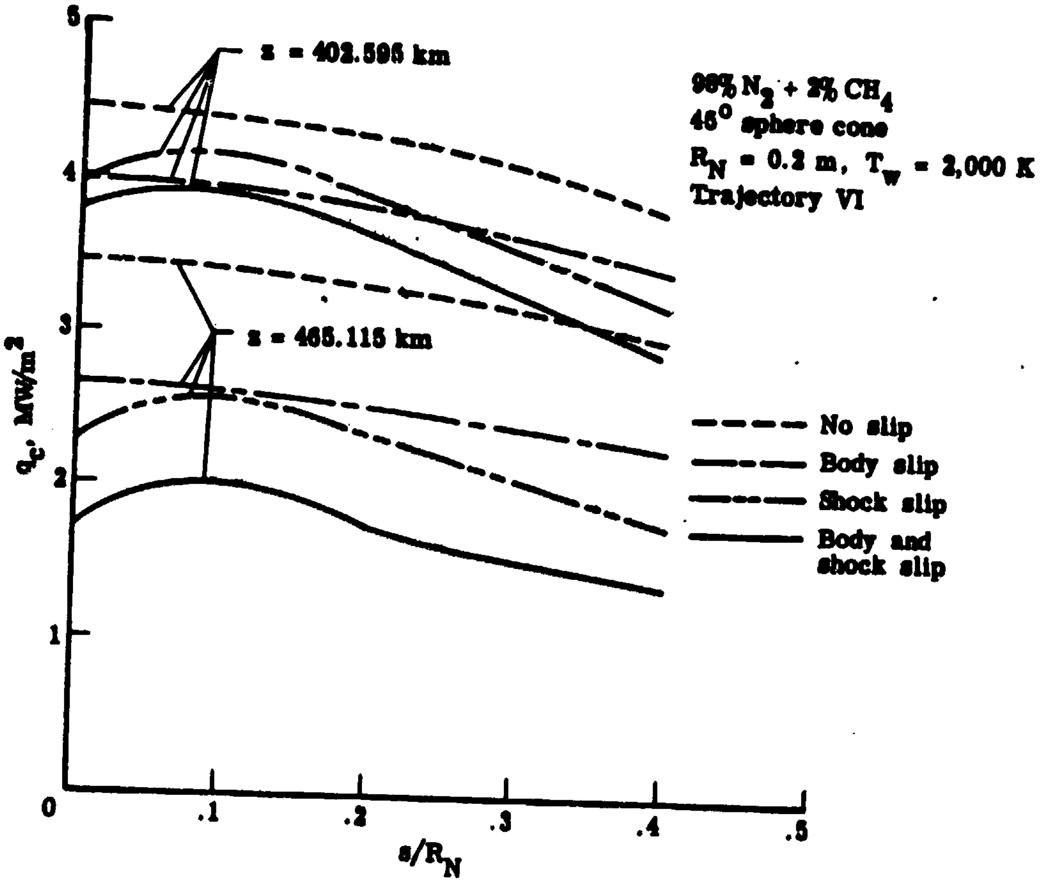

Figure 36. Variation of convective heating along the body for different slip conditions at Z = 402.595 km and Z = 465.115 km.

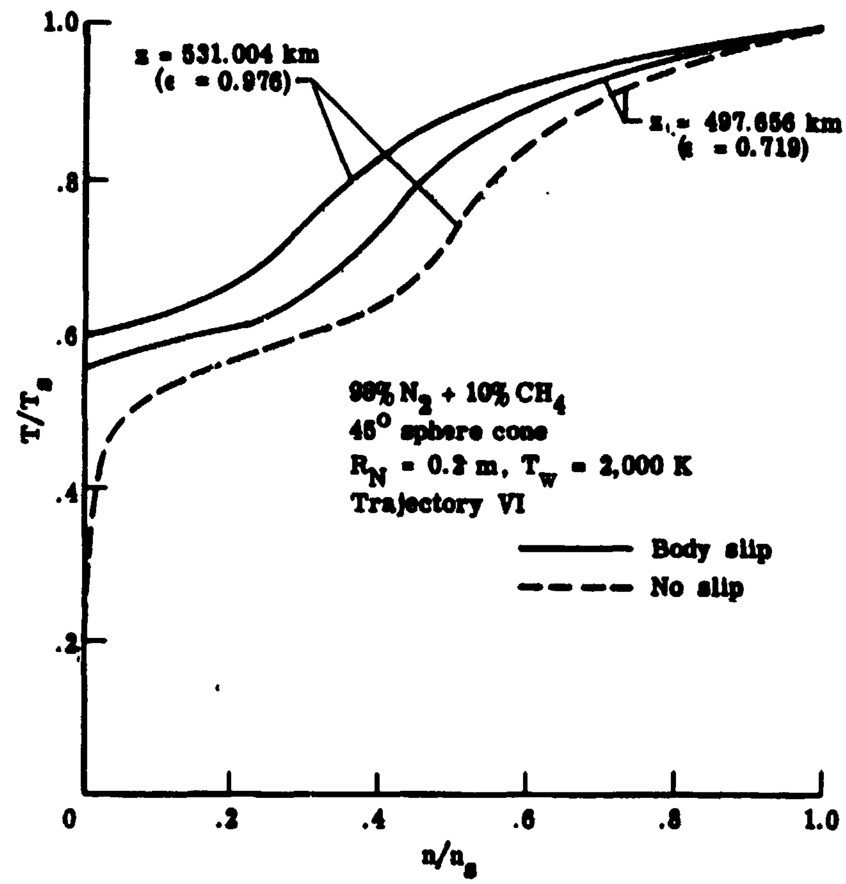

Figure 37. Temperature profile in the shock layer at stagnation point with body slip condition for very high altitudes.

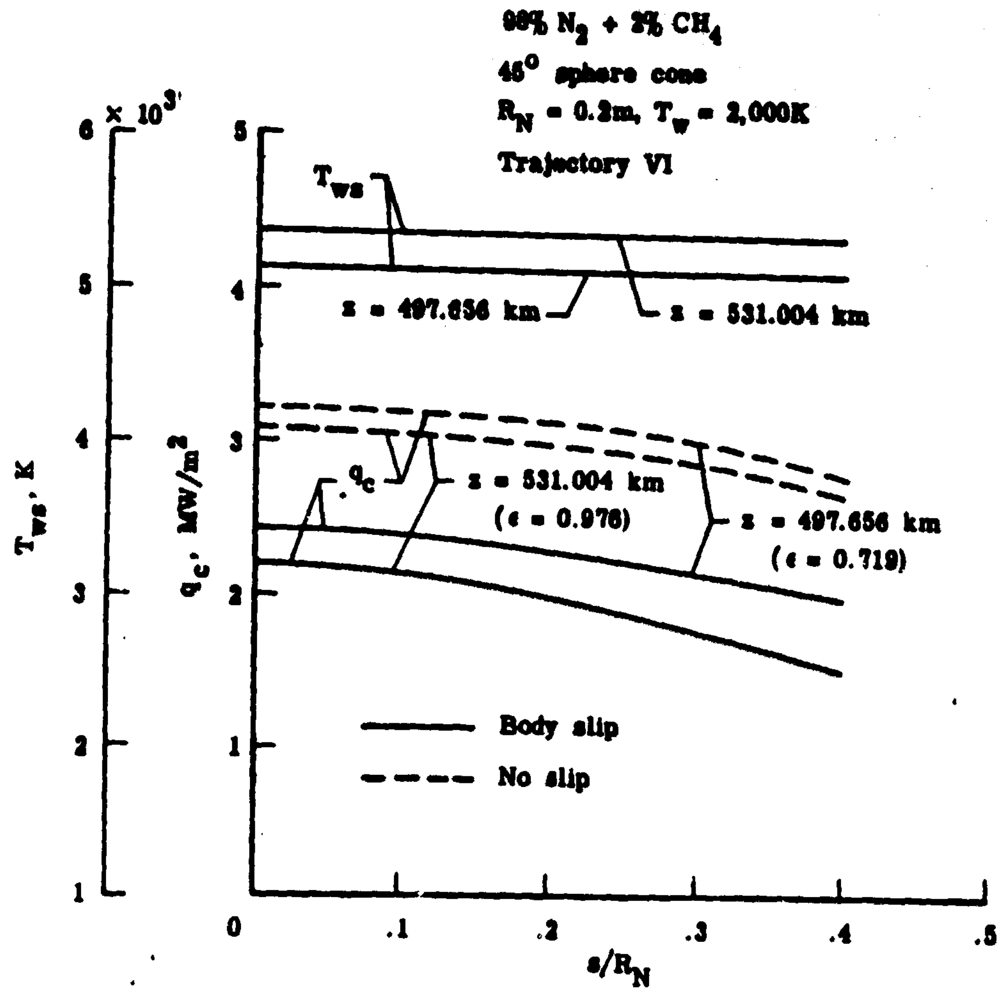

Figure 38. Effect of body slip condition on surface temperature and convective heating for very high altitudes near the stagnation region.

10. CONCLUSIONS

The main objective of this study was to assess the extent of convective and radiative heating that would be experienced by an aerocapture vehicle in a Titan mission. Different compositions for Titan's atmosphere were assumed and results were obtained for the entry trajectories specified by JPL. The influences of slip boundary conditions (both at the shock and the body) were investigated for important cases. Specific results were obtained for free-stream atmospheric compositions of 90% N_2 + 10% CH_4, 99.5% N_2 + 0.5% CH_4, and 98% N_2 + 2% CH_4.

Results show that both the convective and radiative heating rates are quite sensitive to the gas composition used. The convective heating increases significantly as the N_2 concentration increases. However, this, in general, is not the case with regard to the radiative heating. The radiative heating is negligible for the shallow entry ($\gamma = -25°$) condition regardless of the free-stream gas composition. But, for the steepest entry angle ($\gamma = -45°$), the radiative heating will be important only if the free-stream gas is assumed to contain N_2 concentrations between 50% and 90%. For the gas composition of 90% N_2, the radiative heating is important in the stagnation region (as well as in the downstream region) with the peak radiative heating rate being 30 percent of the corresponding convective heating rate (about 13 MW/m^2). For the free-stream gas composition of 99.5% N_2 + 0.5% CH_4, the radiative heating, in the stagnation region, is negligible (less than 6%) in comparison to the convective heating for all cases considered. For this gas composition, the peak convective heating is found to be about 15 MW/m^2. The amount of CN concentration in the shock-layer gas determines the extent of the radiative heating. For a given free-stream gas composition, the radiative heating downstream of the stagnation region increases due to an increase in the CN concentration and the optical thickness of the shock layer.

Other results obtained in this study show that higher initial entry speeds produce higher shock temperature which, in turn, results in higher heating rate. Results for the gas composition with 99.5% N_2 indicate that, while the convective heating decreases, the radiative heating increases with increasing body nose radius. Specific results obtained for a more recent trajectory (Trajectory VI with free-stream gas composition of 98% N_2 + 2% CH_4) indicate that radiative heating becomes comparable to the convective heating in the far downstream region of the aerocapture vehicle.

Results of slip conditions (for the recent trajectory with free-stream gas composition of 98% N_2 + 2% CH_4) clearly indicate that both body and shock slip are important in influencing the shock-layer flow phenomena for high-altitude conditions. As such, these should be considered in determining the extent of heating rates to the aerocapture vehicle at higher entry altitudes.

For further study, it is suggested to consider the influence of chemical as well as radiative nonequilibrium in analyzing the aerothermal environment of the aerocapture vehicle. At this time, it might be advisable also to include the effects of thickness and concentration slip. However, during most of the heating pulse, this study indicates that accurate results can be obtained without including slip boundary conditions while using the assumption of equilibrium flow.

REFERENCES

1. French, J.R.; and Cruz, M.I.: Aerobreaking and Aerocapture for Planetary Missions. Astronautics and Aeronautics, Feb. 1980, pp. 48-71.

2. Cruz, M.I.: Aerocapture Vehicle Mission Design Concept. AIAA Paper 79-0893, May 1979.

3. Cruz, M.I.: Aerocapture Vehicle Mission Design Concepts for the Inner and Outer Planets. AIAA Paper 79-115, June 1979.

4. Armento, R.F.: Mars Aerocapture Vehicle Definition Study Final Report. G.E. Document No. 79SR2258, Sept. 1979.

5. Cruz, M.I.: Technology Requirements for a Generic Aerocapture System. AIAA Paper 80-1493, July 1980.

6. Florence, D.E.: Aerothermodynamic Design Feasibility of a Mars Aerocapture/Aeromaneuver Vehicle. AIAA Paper 81-0350, Jan. 1981.

7. Golden, F.: Visit to a Large Planet: A Thousand Rings Round Saturn, Icy Moons and Lakes of Liquid Nitrogen. Time Magazine, Vol. 116, No. 21, Nov. 24, 1980, pp. 32-41.

8. Bird, R.B.; Stewart, W.E.; and Lightfoot, E.N.: Transport Phenomena. John Wiley & Sons, Inc. (N.Y.), 1960.

9. Williams, Forman A.: Combustion Theory. Addison-Wesley Pub. Co., Inc. 1965.

10. Davis, R.T.: Numerical Solution of the Hypersonic Viscous-Shock-Layer Equations. AIAA J., Vol. 8, May 1970, pp. 843-845.

11. Moss, J.N.: Stagnation and Downstream Viscous-Shock-Layer Solution with Radiation and Coupled Ablation Injection. AIAA Paper 74-73, Jan. 1974; also AIAA J., Vol. 14, Sept. 1976, pp. 1311-1317.

12. Tiwari, S.N.; and Szema, K.Y.: Influence of Precursor Heating on Viscous Flow Around a Jovian Entry Body. Progress in Astronautics and Aeronautics: Outer Planet Entry Heating and Thermal Protection. Vol. 64, edited by R. Viskanta, AIAA. (N.Y.), 1979, pp. 80-107.

13. Moss, J.N.: Reacting Viscous-Shock-Layer Solutions with Multicomponent Diffusion and Mass Injection. NASA TR-411, June 1974.

14. Shidlovskiy, V.P.: Introduction to Rarefield Gases. American Elsevier Publishing Company, Inc. (N.Y.), 1967.

15. Patterson, G.N.: Molecular Flow Gases. John Wiley and Sons, Inc. (N.Y), 1965.

16. Street, R.E.: Problem of Slip Flow in Aerodynamics. NASA RM S-7A30, 1957.

17. Scott, C.D.: Reacting Shock Layer with Slip and Catalytic Boundary Condition. AIAA J., Vol. 13, Oct. 1957, pp. 1271-1278.

18. Esch, D.D.; Siripong, A.; and Pike, R.W.: Thermodynamic Properties in Polynomial Form for Carbon, Hydrogen, Nitrogen, and Oxygen Systems From 300 to 15,000 K. NASA CR-111989, Nov. 1970.

19. Stroud, C.W.; and Brinkley, K.L.: Chemical Equilibrium of Ablation Materials Including Condensed Species. NASA TN D-5391, Aug. 1969.

20. Vincenti, W.G.; and Kruger, C.H.: Introduction to Physical Gas Dynamics. John Wiley and Sons, 1965.

21. Sparrow, E.M.; and Cess, R.D.: Radiation Heat Transfer. Brooks/Cole Publishing Co. (Belment, Calif.), 1966.

22. Nicolet, W.E.: User's Manual for the Generalized Radiation Transfer Code (RAD/EQUIL). NASA CR-116353, Oct. 1969; also User's Manual for RAD/EQIL/1973, A General Purpose Radiation Transport Program. NASA CR-132470, Nov. 1973.

23. Kao, Hsiao C.: Hypersonic Viscous Flow Near the Stagnation Streamline of a Blunt Body. I-A Test of Local Similarity, AIAA J., Vol. 2, No. 11, Nov. 1964, pp. 1892-1897.

24. Tiwari, S.N.; and Szema, K.Y.: Effects of Precursor Heating on Radiative and Chemically Reacting Viscous Flow Around a Jovian Entry Body. NASA CR-3186, Oct. 1979.

PRECEDING PAGE BLANK NOT FILMED

APPENDIX

Table 1. Constant for polynomial approximations of thermodynamic properties.

SPECIES	a_1	a_2	a_3	a_4	a_5	a_6	a_7	T
N	.2503E+01	-.2180E-04	.5420E-07	-.5647E-10	.2099E-13	.560989E+05	.4167E+01	300 K
	.2450E+01	.1066E-03	-.7465E-07	.1879E-10	-.1025E-14	.561160E+05	.4448E+01	1000 K
	.2748E+01	-.3909E-03	.1338E-06	-.1191E-10	.3369E-15	.560900E+05	.2872E+01	6000 K
N_2	.3674E+01	-.1208E-02	.2324E-05	-.6321E-09	-.2257E-12	-.106116E+04	.2358E+01	300 K
	-.2896E+01	.1515E-02	-.5723E-06	.9980E-10	-.6522E-14	-.905862E+03	.6161E+01	1000 K
	.3727E+01	.4684E-03	-.1140E-06	.1154E-10	-.3293E-15	-.104300E+04	.1294E+01	6000 K
N^+	.2727E+01	-.2820E-03	.1105E-06	-.1551E-10	.7847E-15	.225400E+06	.3645E+01	300 K
	.2727E+01	-.2820E-03	.1105E-06	-.1551E-10	.7847E-15	.225400E+06	.3645E+01	1000 K
	.2499E+01	-.3725E-05	.1147E-07	-.1102E-11	.3078E-16	.225400E+06	.4950E+01	6000 K
C	.2532E+01	-.1588E-03	.3068E-06	-.2677E-09	.8748E-13	.852404E+05	.4606E+01	300 K
	.2581E+01	-.1469E-03	.7438E-07	-.7948E-11	.5890E-16	.852163E+05	.4312E+01	1000 K
	.2141E+01	.3219E-03	-.5498E-07	.3604E-11	-.5564E-16	.854200E+05	.6874E+01	6000 K
C_2	.7451E+01	-.1014E-01	.8587E-05	.8732E-09	-.2442E-11	.989120E+05	-.1584E+02	300 K
	.4043E+01	.2057E-03	.1090E-06	-.3642E-10	.3412E-14	.997095E+05	.1277E+01	1000 K
	.4026E+01	.4857E-03	-.7026E-07	.4666E-11	-.1142E-13	.978700E+05	.1090E+01	6000 K
C_3	.5740E+01	-.8428D-02	.1862E-04	-.1451E-07	.3967E-11	.971575E+05	-.2383E+01	300 K
	.3681E+01	.2416E-02	-.8434E-06	.1450F-09	-.9569E-14	.974140E+05	.6837E+01	1000 K
	.2213E+01	-.1759E-01	.5565E-05	-.6758E-09	.2825E-13	.942300E+05	-.1021E+03	6000 K
C^+	.2595E+01	-.4068E-03	.6892E-06	-.5266E-09	.1508E-12	.216663E+06	.3895E+01	300 K
	.2511E+01	-.1735E-04	.9504E-08	-.2218E-11	.1862E-15	.216677E+06	.4286E+01	1000 K
	.2528E+01	.4869E-05	-.7026E-08	.1134E-11	-.3476E-16	.216800E+06	.4139E+01	6000 K
C_2H	.2649E+01	.8491E-02	-.9816E-05	.6537E-08	-.1735E-11	.562758E+05	.7689E+01	300 K
	.4420E+01	.2211E-02	-.5929E-06	.9419E-10	-.6852E-14	.558354E+05	-.1158E+01	1000 K
	.5307E+01	.8966E-03	-.1378E-06	.9251E-11	-.2278E-15	.580900E+05	-.5288E+01	6000 K

Table 1. (Concluded.)

SPECIES	a_1	a_2	a_3	a_4	a_5	a_6	a_7	T
C_2H_2	.1410E+01	.1905E-01	-.2450E-04	.1639E-07	-.4134E-11	.261882E+05	.1139E+02	300 K
	.4575E+01	.5123E-02	-.1745E-05	.2867E-09	-.1795E-13	.256074E+05	-.3573E+01	1000 K
	.6789E+01	.1503E-02	-.2295E-06	.1534E-10	-.3763E-15	.259000E+05	-.1539E+02	6000 K
C_3H	.3344E+01	.1068E-01	-.1331E-04	.1338E-07	-.5698E-11	.625819E+05	.6000E+01	300 K
	-.3877E+01	.6724E-02	-.2605E-05	.4416E-09	-.2708E-13	.625643E+05	.3826E+01	1000 K
	.3877E+01	.6724E-02	-.2605E-05	.4416E-09	-.2708E-13	.635643E+05	.3826E+01	6000 K
C_4H	.4968E+01	.1727E-01	-.2994E-04	.3246E-07	-.1366E-10	.754546E+05	-.8769E+00	300 K
	.6531E+01	.6506E-02	-.2251E-05	.3329E-09	-.1721E-13	.753505E+05	-.7446E+01	1000 K
	.6531E+01	.6506E-02	-.2251E-05	.3329E-09	-.1721E-13	.753504E+05	-I	6000 K
CN	.3738E+01	-.1923E-02	.4703E-05	-.3111E-08	.6167E-12	.512709E+05	.3449E+01	300 K
	.3603E+01	.3364E-03	.1002E-06	-.1631E-10	-.3628E-15	.511598E+05	.3545E+01	1000 K
	.3473E+01	.7337E-03	-.9088E-07	.4847E-11	-.1018E-15	.542000E+05	.4152E+01	6000 K
H	.2500E+01	0.	0.	0.	0.	.254716E+05	-.4601E+00	300 K
	.2500E+01	0.	0.	0.	0.	.254716E+05	-.4601E+00	1000 K
	.2475E+01	.7366E-04	-.2537E-07	.2386E-11	-.4551E-16	.252363E+05	-.3749E+00	6000 K
H_2	.3057E+01	.2676E-02	-.5809E-05	.5521E-08	-.1812E-11	-.988905E+03	-.2299E+01	300 K
	.3100E+01	.5111E-03	.5264E-07	-.3491E-10	.3694E-14	-.877380E+03	-.1962E+01	1000 K
	.3363E+01	.4656E-03	.5127E-07	.2802E-11	-.4905E-16	-.101800E+04	-.3716E+01	6000 K
H^+	.2500E+01	0.	0.	0.	0.	.184033E+06	-.1153E+01	300 K
	.2500E+01	0.	0.	0.	0.	.184033E+06	-.1153E+01	1000 K
	.2500E+01	0.	0.	0.	0.	.184033E+06	-.1153E+01	6000 K
HCN	.2451E+01	.8720E-02	-.1009E-04	.6725E-08	-.1762E-11	.152130E+00	.5080E+02	300 K
	.3706E+01	.3338E-02	-.1191E-05	.1999E-09	-.1282E-13	.149626E+05	.2079E+01	1000 K
	.3706E+01	.3338E-02	-.1191E-05	.1999E-09	-.1282E-13	.149626E+05	.2079E+01	6000 K
E^-	.2500E+01	0.	0.	0.	0.	-.745375E+03	-.1173E+02	300 K
	.2500E+01	0.	0.	0.	0.	-.745375E+03	-.1173E+02	1000 K
	.2508E+01	-.6332E-05	.1364E-08	-.1094E-12	.2934E-17	-.754000E+03	-.1208E+02	6000 K

Table 2. Viscosity and thermal conductivity constants.

SPECIES	b_1	b_2	b_3	c_1	c_2
N	.253000E-05	.220600E-07	-.373700E-12 *	.128100E-04	.859300E-08
N_2	.9 0000E-05	.161300E-07	-.191600E-12 *	.654000E-05	.645700E-08
N^+	0.	.500000E-08	-.100000E-12 *	.260000E-03	0.
C	.199700E-04	.177200E-07	-.337800E-12 *	.250600E-04	.747900E-08
C_2	.193100E-04	.139300E-07	-.257500E-12 *	.859000E-05	.623300E-08
C_3	.201900E-04	.117900E-07	-.165500E-12 *	.630000E-05	.580400E-08
C^+	0.	.500000E-08	-.100000E-12 *	.260000E-03	0.
C_2H	.240400E-04	.136300E-07	-.218400E-12 *	.112600E-04	.743900E-08
C_2H_2	.139600E-04	.842000E-08	-.693900E-12 *	.112600E-04	.743900E-08
C_3H	.201900E-04	.117900E-07	-.165500E-12 *	.630000E-05	.580400E-08
C_4H	.201900E-04	.117900E-07	-.165500E-12 *	.630000E-05	.580400E-08
CN	.240400E-04	.136300E-07	-.218400E-12 *	.859000E-05	.623300E-08
H	.294000E-05	.889000E-08	-.811000E-03 *	.249600E-04	.512900E-07
H^2	-.790000E-06	.791000E-08	-.886000E-13 *	.321100E-04	.534400E-07
H^+	0.	.500000E-08	-.100000E-12 *	.260000E-03	0.
HCN	.137800E-04	.965000E-08	-.948000E-13 *	.486000E-05	.580400E-08
E^-	0.	.500000E-08	-.100000E-12 *	.260000E-03	0.

Table 3. Altitude and free-stream conditions: Trajectory I ($L/D = 1.2$, $\gamma = -45°$, $\beta = 800\ kg/m^2$, $U_E = 10\ km/s$).

TIME (s)	ALTITUDE (km)	ρ_∞ (g/cm^3)	p_∞ (mb)	T_∞ (K)	V_∞ (km/s)	MACH NO.
40	230.965	0.1265E-6	0.10355	159.10	9.929	29.13
50	169.824	0.3473E-6	0.24562	139.44	9.803	30.72
60	114.238	0.1022E-5	0.64627	119.17	9.431	31.90
70	70.409	0.3197E-5	1.5836	103.16	8.448	30.78
78	50.922	0.5157E-5	2.5901	96.28	7.185	27.10
90	48.539	0.5512E-5	2.7449	95.56	5.502	20.83
100	60.654	0.3944E-5	1.9738	99.26	4.727	17.56
150	95.613	0.1604E-5	0.89555	112.46	3.406	11.89
220	173.831	0.3728E-6	0.23159	140.84	3.015	9.40

Table 4. Altitude and free-stream conditions: Trajectory II ($L/D = 1.2$, $\gamma = -25°$, $\beta = 800\ kg/m^2$, $U_E = 10\ km/s$).

TIME (s)	ALTITUDE (km)	ρ_∞ (g/cm^3)	p_∞ (mb)	T_∞ (K)	V_∞ (km/s)	MACH NO.
50	321.264	0.3952E-7	0.3249E-1	160.00	9.953	29.11
100	213.217	0.1654E-6	0.1335E+0	155.60	9.689	28.74
110	198.471	0.2063E-6	0.1638E+0	150.30	9.583	28.91
120	185.306	0.2694E-6	0.1967E+0	145.10	9.451	29.03
130	173.617	0.3288E-6	0.2323E+0	140.76	9.286	28.96
140	163.335	0.3812E-6	0.2683E+0	137.16	9.100	28.75
150	154.339	0.4687E-6	0.3139E+0	134.02	8.889	28.41
170	141.502	0.6712E-6	0.3909E+0	129.53	8.358	27.18
175	139.412	0.7052E-6	0.4053E+0	128.79	8.210	26.77
180	137.610	0.7213E-6	0.4215E+0	128.16	8.062	26.36
200	130.832	0.7855E-6	0.4875E+0	125.79	7.495	24.73

Table 5. Altitude and free-stream conditions: Trajectory III ($L/D = 1.2$, $\gamma = -45°$, $\beta = 800\ kg/m^2$, $U_E = 6$ km/s).

TIME (s)	ALTITUDE (km)	ρ_∞ (g/cm^3)	p_∞ (mb)	T_∞ (K)	V_∞ (km/s)	MACH NO.
90	144.674	0.6142E-6	0.3719	130.00	5.847	18.93
100	111.891	0.1076E-5	0.6732	118.70	5.681	19.29
110	83.284	0.2349E-5	1.1359	108.10	5.379	19.14
120	61.655	0.3859E-5	1.9338	99.60	4.872	18.06
129	49.822	0.5318E-5	2.6615	95.90	4.327	16.35
140	45.041	0.6079E-5	2.9723	94.50	3.690	14.04
150	47.699	0.5643E-5	2.7995	95.30	3.245	12.30
160	54.496	0.4666E-5	2.3577	97.30	2.934	11.01
170	63.709	0.3693E-5	1.8516	100.50	2.724	10.05

Table 6. Altitude and free-stream conditions: Trajectory IV ($L/D = 1.2$, $\gamma = -45°$, $\beta = 800$ kg/m^2, $U_E = 8$ km/s).

TIME (s)	ALTITUDE (km)	ρ_∞ (g/cm^3)	p_∞ (mb)	T_∞ (K)	V_∞ (km/s)	MACH NO.
60	181.218	0.2927E-6	0.2070	143.48	7.883	24.35
70	134.830	0.7469E-6	0.4464	127.19	7.709	25.30
80	93.931	0.1689E-5	0.9283	111.87	7.329	25.63
90	63.296	0.3726E-5	1.868	100.32	6.515	24.07
97	50.882	0.5162E-5	2.592	96.26	5.783	21.81
110	46.913	0.5768E-5	2.850	95.07	4.554	17.28
120	54.841	0.4621E-5	2.335	97.17	3.961	14.84
130	67.354	0.3413E-5	1.706	101.94	3.603	13.20
150	98.351	0.1473E-5	0.8421	113.42	3.240	11.25

Table 7. Altitude and free-stream conditions: Trajectory V ($L/D = 1.2$, $\gamma = -45°$, $\beta = 800\ kg/m^2$, $U_E = 13$ km/s).

TIME (s)	ALTITUDE (km)	ρ_∞ (g/cm^3)	p_∞ (mb)	T_∞ (K)	V_∞ (km/s)	MACH NO.
30	237.512	0.1143E-6	0.0937	159.75	12.905	37.77
40	158.551	0.4165E-6	0.2887	135.49	12.672	40.28
50	90.769	0.1863E-5	0.9899	110.77	11.777	41.40
60	51.374	0.5092E-5	2.560	96.41	9.361	35.28
61	49.676	0.5339E-5	2.671	95.90	9.084	34.33
70	49.557	0.5357E-5	2.678	95.86	7.047	26.64
80	67.533	0.3401E-5	1.698	102.01	5.912	21.66
100	101.803	0.1345E-5	0.7892	114.72	5.083	17.56
120	124.659	0.8488E-6	0.5381	123.63	4.762	15.84

Table 8. Altitude and free-stream conditions: Trajectory VI ($L/D = 1.4$, $\gamma = -36°$, $\beta = 800$ kg/m^2, $U_E = 12$ km/s).

TIME (s)	ALTITUDE (km)	ρ_∞ (g/cm^3)	p_∞ (mb)	T_∞ (K)	V_∞ (km/s)	MACH NO.
10	531.004	0.1282E-08	0.846E-03	177	11.994	44.09
15	497.656	0.2366E-08	0.185E-02	177	11.996	44.10
20	465.115	0.4441E-08	0.432E-02	177	11.997	44.11
30	402.595	0.1489E-07	0.904E-02	177	11.995	44.10
60	241.838	0.4396E-06	0.4279E	177	11.664	42.88
70	204.570	0.1019E-05	0.7567	177	11.096	40.79
73	196.349	0.1227E-05	0.8292	177	10.843	39.86
77	187.956	0.1483E-05	0.9033	177	10.459	38.45
81	182.652	0.1672E-05	0.9501	177	10.043	36.92
90	181.525	0.1715E-05	0.9600	177	9.144	33.62
100	192.414	0.1341E-05	0.8640	177	8.405	30.90
110	200.836	0.1109E-05	0.7897	177	7.902	29.05
120	204.913	0.1012E-05	0.7537	177	7.510	27.61
130	205.759	0.9926E-06	0.7462	177	7.175	26.37

Table 9. Free-stream thermodynamic values for different gas compositions.

MOLE FRACTION	MIXTURE MOLECULAR WEIGHT ($\overline{M}$)	MIXTURE SPECIFIC HEAT (ft^2/s^2 - R)	MIXTURE ENTHALPY (Btu/lbm)
10% N_2 + 90% CH_4	17.238	11816.0	1933.22
25% N_2 + 75% CH_4	19.035	10884.6	1622.04
50% N_2 + 50% CH_4	22.030	9326.5	1103.42
75% N_2 + 25% CH_4	25.025	7771.2	584.80
90% N_2 + 10% CH_4	26.822	6836.5	273.62
98% N_2 + 2% CH_4	27.780	6338.2	107.66
99.5% N_2 + 0.5% CH_4	27.960	6235.2	76.54

Table 10. Stagnation results (sphere cone, R_N = 0.2 m, T_w = 2,000 K): atmosphere - 99.5% N_2 + 0.5% CH_4, Trajectory I.

(a)

TIME (s)	ρ_∞ (kg/m^3)	P_s (atm)	ρ_s/ρ_∞	T_s (K)	n_s (cm)	$q_{c,w}$ (MW/m^2)	$q_{r,w}$ (MW/m^2)
40	0.1265E-3	0.1163	18.13	8508	0.7963	5.783	0.0044
50	0.3473E-3	0.3112	17.93	8498	0.8241	8.558	0.0155
60	0.1022E-2	0.8473	17.76	8262	0.8381	12.265	0.0576
70	0.3197E-2	2.1194	16.75	7902	0.8927	14.818	0.2391
78	0.5157E-2	2.4560	15.08	7354	1.0011	11.188	0.3136
90	0.5512E-2	1.5121	12.10	6412	1.2341	4.688	0.2249
100	0.3944E-2	0.7888	10.48	5813	1.4109	2.290	0.1387

Table 10. (Concluded.)

(b)

TIME (s)	h_w (kJ/kg)	h_s (kJ/kg)	St	Re
40	2.045E+03	48.799E+03	0.9797E-01	0.1065E+04
50	2.045E+03	47.629E+03	0.5497E-01	0.2867E+04
60	2.045E+03	44.082E+03	0.3013E-01	0.8317E+04
70	2.045E+03	35.275E+03	0.1640E-01	0.2438E+05
78	2.045E+03	25.445E+03	0.1280E-01	0.3783E+05
90	2.045E+03	14.799E+03	0.1200E-01	0.3679E+05
100	2.045E+03	10.873E+03	0.1374E-01	0.2513E+05

Table 11. Stagnation results (sphere cone, R_N = 0.2 m, T_w = 2,000 K): atmosphere - 99.5% N_2 + 0.5% CH_4, Trajectory III.

(a)

TIME (s)	ρ_∞ (kg/m^3)	P_s (atm)	ρ_s/ρ_∞	T_s (K)	η_s (cm)	$q_{c,w}$ (MW/m^2)	$q_{r,w}$ (MW/m^2)
90	0.6135E-03	0.1926	13.96	5983	1.0951	2.035	0.0110
100	0.1075E-02	0.3174	13.31	6056	1.1407	2.416	0.0232
110	0.2345E-02	0.6164	12.22	6103	1.2286	2.895	0.0669
120	0.3855E-02	0.8218	10.84	5908	1.3689	2.545	0.1323
129	0.5312E-02	0.8805	9.45	5546	1.5510	1.860	0.2084
140	0.6072E-02	0.7185	8.10	4823	1.7890	1.009	0.217[illegible]
150	0.5637E-02	0.5113	7.56	4004	1.9090	0.528	0.1709
160	0.4660E-02	0.3448	7.37	3358	1.9600	0.275	0.0889

Table 11. (Concluded.)

(b)

TIME (s)	h_w (kJ/kg)	h_s (kJ/kg)	St	Re
90	2.045E+03	16.764E+03	0.3820E-01	0.4533E+04
100	2.045E+03	15.840E+03	0.2844E-01	0.7693E+04
110	2.045E+03	14.161E+03	0.1876E-01	0.1598E+05
120	2.045E+03	11.550E+03	0.1406E-01	0.2488E+05
129	2.045E+03	9.045E+03	0.1135E-01	0.3262E+05
140	2.045E+03	6.512E+03	0.9842E-02	0.3618E+05
150	2.045E+03	4.982E+03	0.9514E-02	0.3456E+05
160	2.045E+03	4.038E+03	0.9694E-02	0.2984E+05

Table 12. Stagnation results (sphere cone, R_N = 0.2 m, T_w = 2,000 K): atmosphere - 99.5% N_2 + 0.5% CH_4, Trajectory IV.

(a)

TIME (s)	ρ_∞ (kg/m^3)	P_s (atm)	ρ_s/ρ_∞	T_s (K)	n_s (cm)	$q_{c,w}$ (MW/m^2)	$q_{r,w}$ (MW/m^2)
60	0.2923E-03	0.1696	18.07	6658	0.8557	4.039	0.0047
70	0.7460E-02	0.4219	17.26	6942	0.8921	6.032	0.0191
80	0.1687E-02	0.8398	16.05	7004	0.9536	7.233	0.0589
90	0.3722E-02	1.4520	14.27	6866	1.0610	7.118	0.1549
97	0.5156E-02	1.5700	12.71	6561	1.1805	5.527	0.2061
110	0.5700E-02	1.0640	9.95	5759	1.4780	2.385	0.2291
120	0.4616E-02	0.6349	8.67	5147	1.6800	1.205	0.1618
130	0.3410E-02	0.3844	8.03	4640	1.8060	0.667	0.1037

Table 12. (Concluded.)

(b)

TIME (s)	h_w (kJ/kg)	h_s (kJ/kg)	St	Re
60	2.045E+03	30.707E+03	0.6080E-01	0.2475E+04
70	2.045E+03	30.027E+03	0.3680E-01	0.6063E+04
80	2.0454+03	26.496E+03	0.2970E-01	0.1303E+05
90	2.045E+03	20.873E+03	0.1540E-01	0.2681E+05
97	2.045E+03	16.374E+03	0.1279E-01	0.3516E+05
110	2.045E+03	10.051E+03	0.1117E-01	0.3588E+05
120	2.045E+03	7.534E+03	0.1174E-01	0.2784E+05
130	2.045E+03	6.193E+03	0.1275E-01	0.2050E+05

Table 13. Stagnation results (sphere cone, R_N = 0.2 m, T_w = 2,000 K): atmosphere - 99.5% N_2 + 0.5% CH_4, Trajectory V.

(a)

TIME (s)	ρ_∞ (kg/m^3)	P_s (atm)	ρ_s/ρ_∞	T_s (K)	n_s (cm)	$q_{c,w}$ (MW/m^2)	$q_{r,w}$ (MW/m^2)
30	0.1141E-03	0.1770	17.77	11938	0.8026	12.601	0.5307
40	0.4161E-03	0.6200	16.70	12606	0.8689	21.193	3.5369
50	0.1860E-02	2.3840	15.55	12628	0.8778	31.959	9.6454
60	0.5086E-02	4.1380	16.67	8881	0.8786	24.967	1.0094
61	0.5333E-02	4.0860	16.64	8630	0.8866	23.314	0.8945
70	0.5350E-02	2.4490	14.87	7290	1.0150	10.687	0.3173
80	0.3397E-02	1.0850	13.18	6507	1.1430	4.881	0.1143
100	0.1343E-02	0.3143	11.77	5791	1.2758	1.769	0.0327

Table 13. (Concluded.)

(b)

TIME (s)	h_w (kJ/kg)	h_s (kJ/kg)	St	Re
30	2.045E+03	82.571E+03	0.1056	0.1451E+04
40	2.045E+03	79.543E+03	0.5154E-01	0.4664E+04
50	2.045E+03	68.739E+03	0.2175E-01	0.1636E+05
60	2.045E+03	43.342E+03	0.1261E-01	0.3902E+05
61	2.045E+03	40.801E+03	0.1233E-01	0.4089E+05
70	2.045E+03	24.443E+03	0.1255E-01	0.3898E+05
80	2.045E+03	17.144E+03	0.1595E-01	0.2371E+05
100	2.045E+03	12.612E+03	0.24255E-01	0.9115E+04

Table 14. Stagnation results (sphere cone, R_N = 0.2 m, T_w = 2,000 K): atmosphere - 90% N_2 + 10% CH_4.

(a)

TIME (s)	ρ_∞ (kg/m^3)	P_s (atm)	ρ_s/ρ_∞	T_s (K)	n_s (cm)	$q_{c,w}$ (MW/m^2)	$q_{r,w}$ (MW/m^2)
			Atmosphere - 90% N_2 + 10% CH_4, Trajectory I				
40	0.1265E-3	0.1165	18.56	7259	0.8029	5.247	0.0177
50	0.3473E-3	0.3112	17.95	7460	0.8440	8.126	0.0713
60	0.1022E-2	0.8455	17.15	7544	0.8880	11.637	0.3569
70	0.3197E-2	2.1108	15.74	7342	0.9619	13.498	2.0398
78	0.5157E-2	2.443	14.08	6733	1.0642	9.687	3.7697
90	0.5512E-2	1.512	12.10	5269	1.2120	3.543	3.8894
100	0.3944E-2	0.7999	12.10	4127	1.2208	1.683	1.5915

			Atmosphere - 90% N_2 + 10% CH_4, Trajectory I				
140	0.3812E-3	0.2942	17.78	6953	0.8586	6.437	0.0862
150	0.4687E-3	0.3449	17.49	6895	0.8731	6.523	0.1190
170	0.6712E-3	0.4355	16.75	6729	0.9111	6.242	0.2044
175	0.7052E-3	0.4413	16.58	6665	0.9201	6.061	0.2206
180	0.7213E-3	0.4350	16.39	6596	0.9300	5.747	0.2287
200	0.7855E-3	0.4081	15.63	6330	1.9723	4.589	0.2728

Table 14. (Concluded.)

(b)

TIME (s)	h_w (kJ/kg)	h_s (kJ/kg)	St	Re
		Atmosphere - 90% N_2 + 10% CH_4, Trajectory I		
40	2.877E+03	48.397E+03	0.9140E-01	0.1221E+04
50	2.877E+03	47.175E+03	0.5365E-01	0.3250E+04
60	2.877E+03	43.595E+03	0.2949E-01	0.9229E+04
70	2.877E+03	38.804E+03	0.1554E-01	0.2736E+05
78	2.877E+03	25.002E+03	0.1173E-01	0.4218E+05
90	2.877E+03	14.347E+03	0.1007E-01	0.4460E+05
100	2.877E+03	10.440E+03	0.1182E-01	0.3408E+05
		Atmosphere - 90% N_2 + 10% CH_4, Trajectory II		
140	2.877E+03	40.565E+03	0.4904E-01	0.3576E+04
150	2.877E+03	38.609E+03	0.4352E-01	0.4358E+04
170	2.877E+03	34.094E+03	0.3545E-01	0.6097E+04
175	2.877E+03	32.835E+03	0.3470E-01	0.6378E+04
180	2.877E+03	31.651E+03	0.3411E-01	0.6494E+04
200	2.877E+03	27.239E+03	0.3175E-01	0.6941E+04

Table 15. Stagnation results (sphere cone, R_N = 0.2 m, T_w = 2,000 K): atmosphere - 90% N_2 + 10% CH_4, Trajectory III.

(a)

TIME (s)	kg/m^3	P_s (atm)	ρ_s/ρ_∞	T_s (K)	n_s (cm)	$q_{c,w}$ (MW/m^2)	$q_{r,w}$ (MW/m^2)
90	0.6142E-03	0.1917	13.24	5159	1.1301	1.661	0.2419
100	0.1076E-02	0.3164	12.81	5210	1.1614	1.907	0.5142
110	0.2349E-02	0.6168	12.31	4974	1.19[illegible]3	2.915	1.3768
120	0.3859E-02	0.8309	12.16	4297	1.2120	1.864	1.8469
129	0.5318E-02	0.8997	11.59	3771	1.2780	1.330	1.0832
140	0.6079E-02	0.7416	10.51	3232	1.4083	0.643	0.2475
150	0.5643E-02	0.5286	9.74	2790	1.5168	0.258	0.0349
160	0.4666E-02	0.3564	9.40	2397	1.5725	0.085	0.0027
170	0.3693E-02	0.2433	9.39	2081	1.5811	0.001	0.0001

Table 15. (Concluded.)

(b)

TIME (s)	h_w (kJ/kg)	h_s (kJ/kg)	St	Re
90	2.877E+03	16.307E+03	0.3417E-01	0.5213E+04
100	2.877E+03	15.366E+03	0.2477E-01	0.8998E+04
110	2.8774+03	13.694E+03	0.1590E-01	0.1949E+05
120	2.877E+03	11.116E+03	0.1190E-01	0.3311E+05
129	2.877E+03	8.627E+03	0.9913E-02	0.4579E+05
140	2.877E+03	6.099E+03	0.8725E-02	0.5154E+05
150	2.877E+03	4.564E+03	0.8114E-02	0.4779E+05
160	2.877E+03	3.611E+03	0.7989E-02	0.4040E+05
170	2.877E+03	3.022E+03	0.7906E-03	0.3311E+05

Table 16. Stagnation results (sphere cone, R_N = 0.2 m, T_w = 2,000 K): atmosphere - 90% N_2 + 10% CH_4, Trajectory IV.

(a)

TIME (s)	h_w (kg/m^3)	P_s (atm)	ρ_s/ρ_∞	T_s (K)	n_s (cm)	$q_{c,w}$ (MW/m^2)	$q_{r,w}$ (MW/m^2)
60	0.2927E-03	0.1689	16.81	6233	0.9092	3.458	0.0704
70	0.7469E-03	0.4199	16.06	6469	0.9482	5.197	0.2430
80	0.1689E-02	0.8356	14.92	6468	1.0130	6.096	0.7787
90	0.3726E-02	1.4447	13.37	6172	1.1155	5.753	2.4460
97	0.5162E-02	1.5660	12.33	5601	1.1946	4.219	3.8516
110	0.5786E-02	1.0828	11.83	4002	1.2498	1.647	1.7776
120	0.4621E-02	0.6529	11.09	3431	1.3387	0.780	0.4077
130	0.3414E-02	0.3972	10.53	3089	1.4118	0.389	0.1017
150	0.1473E-02	0.1381	10.03	2692	1.4921	0.107	0.0093

Table 16. (Concluded.)

(b)

TIME (s)	h_w (kJ/kg)	h_s (kJ/kg)	St	Re
60	2.877E+03	30.243E+03	0.5420E-01	0.2709E+04
70	2.877E+03	29.538E+03	0.3331E-01	0.6663E+04
80	2.8774+03	26.032E+03	0.2113E-01	0.1443E+05
90	2.877E+03	20.401E+03	0.1341E-01	0.3034E+05
97	2.877E+03	15.934E+03	0.1072E-01	0.4140E+05
110	2.877E+03	9.632E+03	0.9168E-02	0.4950E+05
120	2.877E+03	7.124E+03	0.9871E-02	0.3974E+05
130	2.877E+03	5.776E+03	0.1068E-01	0.2932E+05
150	2.877E+03	4.574E+03	0.1308E-01	0.1277E+05

Table 17. Stagnation results (sphere cone, R_N = 0.2 m, T_w = 2,000 K): atmosphere - 90% N_2 + 10% CH_4, Trajectory V.

(a)

TIME (s)	h_w (kg/m^3)	P_s (atm)	ρ_s/ρ_∞	T_s (K)	n_s (cm)	$q_{c,w}$ (MW/m^2)	$q_{r,w}$ (MW/m^2)
30	0.1143E-03	0.1765	16.68	11326	0.8531	11.458	0.3785
40	0.4165E-03	0.6177	15.73	11869	0.9243	19.458	2.2628
50	0.1863E-02	2.3770	14.93	11542	0.9876	31.222	6.2089
60	0.5092E-02	4.1260	15.96	8162	0.9483	23.683	4.0362
61	0.5339E-02	4.0730	15.81	7973	0.9569	21.928	4.3607
70	0.5357E-02	2.4360	13.89	6650	1.0772	9.004	3.8994
80	0.3401E-02	1.0810	12.63	5650	1.1720	3.642	2.3153
100	0.1345E-02	0.3159	12.46	4468	1.1865	1.228	0.6681
120	0.3488E-03	0.1075	12.67	3949	1.1793	0.724	0.3268

Table 17. (Concluded.)

(b)

TIME (s)	h_w (kJ/kg)	h_s (kJ/kg)	St	Re
30	2.877E+03	82.095E+03	0.9763E-01	0.1349E+04
40	2.877E+03	79.105E+03	0.4812E-01	0.4394E+04
50	2.877E+03	68.198E+03	0.2166E-01	0.1616E+05
60	2.877E+03	42.896E+03	0.1235E-01	0.4308E+05
61	2.877E+03	40.331E+03	0.1199E-01	0.4505E+05
70	2.877E+03	24.007E+03	0.1121E-01	0.4358E+05
80	2.877E+03	16.682E+03	0.1300E-01	0.2756E+05
100	2.877E+03	12.170E+03	0.1917E-01	0.1158E+05
120	2.877E+03	10.607E+03	0.2299E-01	0.7620E+04

Table 18. Stagnation results (sphere cone, R_N = 0.2 m, T_w = 2,000 m): atmosphere - 90% N_2 + 10% CH_4, Trajectory VI.

(a)

TIME (s)	kg/m^3	p_s (atm)	ρ_s/ρ_∞	T_s (K)	n_s (cm)	$q_{c,w}$ (MW/m^2)	$q_{r,w}$ (MW/m^2)
60	0.4396E-03	0.5542	16.32	11512	0.8800	16.170	1.1565
70	0.1019E-02	1.1605	15.91	11160	0.8993	20.085	1.5266
73	0.1227E-02	1.3348	15.96	10799	0.8994	20.276	1.2076
77	0.1483E-02	1.5028	16.24	10099	0.8904	19.715	0.6897
81	0.1672E-02	1.5648	16.80	9241	0.8722	18.288	0.3535
90	0.1715E-02	1.3340	17.34	8059	0.8666	14.078	0.2340
100	0.1341E-02	0.8811	17.20	7422	0.8843	9.543	0.1415
110	0.1109E-02	0.6433	16.87	7036	0.9055	7.171	0.1001
120	0.1012E-02	0.5296	16.47	6835	0.9286	5.798	0.0866
130	0.9926E-03	0.4630	16.00	6664	0.9557	4.929	0.0813

Table 18. (Concluded.)

(b)

TIME (s)	h_w (kJ/kg)	h_s (kJ/kg)	St	Re
60	2.173E+03	67.396E+03	0.4813E-01	0.4097E+04
70	2.173E+03	60.923E+03	0.3007E-01	0.8400E+04
73	2.173E+03	58.343E+03	0.2707E-01	0.9861E+04
77	2.173E+03	54.056E+03	0.2434E-01	0.1167E+05
81	2.173E+03	49.834E+03	0.2272E-01	0.1327E+05
90	2.173E+03	41.342E+03	0.2282E-01	0.1396E+05
100	2.173E+03	34.823E+03	0.2576E-01	0.1097E+05
110	2.173E+03	30.710E+03	0.2845E-01	0.9019E+04
120	2.173E+03	27.840E+03	0.2962E-01	0.8154E+04
130	2.173E+03	25.520E+03	0.2975E-01	0.7894E+04

Table 19. Downstream results (sphere cone, R_N = 0.2 m, T_w = 2,000 K): atmosphere - 98% N_2 + 2% CH_4, Trajectory VI, Z = 196.3 km, ε = 0.029.

(a)

S/R_N	$q_{c,w}$ (MW/m^2)	N_s (cm)	Enthalpy (kJ/kg) wall	Enthalpy (kJ/kg) shock	T_s (K)	T_w (K)	ρ_s/ρ_∞	St
				NO SLIP				
0	22.14	0.9568	2177	58250	10799	2000	15.95	0.0295
0.1	21.17	0.9834	2177	57820	10724	2000	15.95	0.0282
0.2	20.91	0.9890	2177	56240	10440	2000	16.09	0.0279
0.3	20.11	1.0040	2177	53560	9904	2000	16.40	0.0268
0.4	18.70	1.0268	2177	50080	9161	2000	16.92	0.0249
				BODY AND SHOCK SLIP				
0	21.99	1.0001	2384	58250	10799	2149	15.95	0.0295
0.1	22.02	0.9743	2383	57940	10745	2149	15.91	0.0295
0.2	21.15	0.9963	2383	56410	10471	2157	16.04	0.0283
0.3	20.49	1.0181	2395	53780	9950	2159	16.33	0.0274
0.4	19.01	1.0455	2400	50370	9221	2167	16.83	0.0255

Table 19. (Concluded.)

(b)

S/R_N	$q_{c,w}$ (MW/m^2)	N_s (cm)	Enthalpy (kJ/kg) wall	Enthalpy (kJ/kg) shock	T_s (K)	T_w (K)	ρ_s/ρ_∞	St
				NO SLIP				
0	22.59	0.9386	2381	58330	10811	2151	15.93	0.0301
0.1	21.62	0.9616	2388	57720	10708	2152	15.98	0.0288
0.2	20.77	0.9793	2382	56200	10433	2149	16.09	0.0278
0.3	20.21	1.0060	2381	53580	9910	2150	16.40	0.0269
0.4	18.71	1.0430	2392	50250	9197	2152	16.89	0.0251
				BODY AND SHOCK SLIP				
0	22.32	0.9674	2177	58330	10812	2000	15.92	0.0298
0.1	21.84	0.9572	2177	57840	10782	2000	15.94	0.0291
0.2	20.93	0.9853	2177	56360	10462	2000	16.04	0.0279
0.3	20.04	1.0162	2177	53760	9946	2000	16.34	0.0267
0.4	18.86	1.0556	2177	50440	9236	2000	16.82	0.0251

Table 20. Downstream results (sphere cone, $R_N = 0.2$ m, $T_w = 2{,}000$ K): atmosphere - 98% N_2 + 2% CH_4, Trajectory VI, Z = 241.8 km, $\epsilon = 0.0515$.

(a)

S/R_N	$q_{c,w}$ (MW/m^2)	N_s (cm)	Enthalpy (kJ/kg) wall	Enthalpy (kJ/kg) shock	T_s (K)	T_w (K)	ρ_s/ρ_∞	St
				NO SLIP				
0	17.27	0.9126	2179	67540	11509	2000	16.33	0.0514
0.1	16.59	0.9357	2179	66860	11441	2000	16.33	0.0493
0.2	16.16	0.9567	2179	65070	11254	2000	16.33	0.0481
0.3	15.44	0.9909	2179	62240	10931	2000	16.33	0.0459
0.4	14.49	1.0374	2179	58320	10409	2000	16.46	0.0431
				BODY AND SHOCK SLIP				
0	18.35	0.9470	2564	67550	11509	2290	16.33	0.0546
0.1	18.16	0.9317	2570	67020	11456	2279	16.29	0.0540
0.2	17.70	0.9643	2567	65290	11276	2389	16.28	0.0526
0.3	16.95	1.0023	2577	62420	10952	2310	16.29	0.0504
0.4	16.26	1.0515	2590	58540	10440	2328	16.42	0.0484

Table 20. (Concluded.)

(b)

S/R_N	$q_{c,w}$ (MW/m^2)	N_s (cm)	Enthalpy (kJ/kg) wall	Enthalpy (kJ/kg) shock	T_s (K)	T_w (K)	ρ_s/ρ_∞	St
				NO SLIP				
0	18.52	0.9141	2570	67520	11506	2289	16.33	0.0511
0.1	17.82	0.9371	2570	66880	11443	2277	16.33	0.0530
0.2	16.03	0.9584	2572	65100	11258	2285	16.33	0.0480
0.3	15.44	0.9931	2577	62280	10936	2286	16.33	0.0462
0.4	14.39	1.0399	2586	58370	10416	2291	16.46	0.0431
				BODY AND SHOCK SLIP				
0	17.03	0.9467	2179	67510	11506	2000	16.33	0.0506
0.1	17.54	0.9313	2179	67020	11456	2000	16.29	0.0522
0.2	16.73	0.9638	2179	65290	11276	2000	16.28	0.0498
0.3	15.97	1.0016	2179	62410	10951	2000	16.29	0.0475
0.4	15.01	1.0507	2179	58530	10438	2000	16.42	0.0446

Table 21. Downstream results (sphere cone, R_N = 0.2 m, T_w = 2,000 K): atmosphere - 98% N_2 + 2% CH_4, Trajectory VI, Z = 402.6 km, ε = 0.286.

(a)

S/R_N	$q_{c,w}$ (MW/m^2)	N_s (cm)	Enthalpy (kJ/kg) wall	Enthalpy (kJ/kg) shock	T_s (K)	T_w (K)	ρ_s/ρ_∞	St
				NO SLIP				
0	4.47	0.6685	2195	71540	10080	2000	18.79	0.360
0.1	4.38	0.6783	2195	70750	10040	2000	18.80	0.353
0.2	4.27	0.6921	2195	68880	9931	2000	18.71	0.344
0.3	4.07	0.7145	2195	65650	9723	2000	18.60	0.328
0.4	3.80	0.7470	2195	61460	9412	2000	18.45	0.306
				BODY AND SHOCK SLIP				
0	3.80	0.7457	5636	69810	9999	3749	19.18	0.322
0.1	3.92	0.7235	5702	69670	9988	3785	19.08	0.333
0.2	3.57	0.7736	5743	67910	9879	3803	19.00	0.303
0.3	3.26	0.8195	5916	65010	9686	3884	18.87	0.278
0.4	2.28	0.8725	6065	60860	9371	3945	18.79	0.245

Table 21. (Concluded.)

(b)

S/R_N	$q_{c,w}$ (MW/m^2)	N_s (cm)	Enthalpy (kJ/kg) wall	Enthalpy (kJ/kg) shock	T_s (K)	T_w (K)	ρ_s/ρ_∞	St
				NO SLIP				
0	3.98	0.6702	6147	71490	10086	2994	18.80	0.340
0.1	3.95	0.6764	6144	70840	10048	3989	18.78	0.337
0.2	3.83	0.6897	6164	68680	9919	3997	18.70	0.327
0.3	3.62	0.7123	6215	65210	9692	4012	18.57	0.309
0.4	3.43	0.7554	6177	61470	9413	3962	18.45	0.292
				BODY AND SHOCK SLIP				
0	3.98	0.7417	2195	69730	9995	2000	19.21	0.321
0.1	4.18	0.7203	2195	69630	9986	2000	19.09	0.337
0.2	3.84	0.7669	2195	67870	9876	2000	19.02	0.310
0.3	3.55	0.8098	2195	64930	9680	2000	18.89	0.287
0.4	3.19	0.8598	2195	60710	9359	2000	18.81	0.258

Table 22. Downstream results (sphere cone, R_N = 0.2 m, T_w = 2,000 K): atmosphere - 98% N_2 + 2% CH_4, Trajectory VI, Z = 465.1 km, ϵ = 0.524.

(a)

S/R_N	$q_{c,w}$ (MW/m^2)	N_s (cm)	Enthalpy (kJ/kg) wall	Enthalpy (kJ/kg) shock	T_3 (K)	T_w (K)	ρ_s/ρ_∞	St
				NO SLIP				
0	3.45	0.6042	2208	71530	9545	2000	19.74	0.934
0.1	3.39	0.6113	2208	70830	9510	2000	19.70	0.918
0.2	3.32	0.6217	2208	68860	9407	2000	19.62	0.896
0.3	3.17	0.6396	2208	65650	9226	2000	19.46	0.857
0.4	2.96	0.6654	2208	61320	8947	2000	19.27	0.801
				BODY AND SHOCK SLIP				
0	1.76	0.6294	8970	53530	8347	4532	23.72	0.527
0.1	2.05	0.6039	9955	58030	8768	4647	23.53	0.624
0.2	1.72	0.7023	9583	57220	8697	4600	23.36	0.519
0.3	1.55	0.7676	9225	55800	8556	4551	22.98	0.465
0.4	1.35	0.8398	8631	53000	8249	4462	22.76	0.401

Table 22. (Concluded.)

(b)

S/R_N	$q_{c,w}$ (MW/m^2)	N_s (cm)	Enthalpy (kJ/kg) wall	Enthalpy (kJ/kg) shock	T_s (K)	T_w (K)	ρ_s/ρ_∞	St
				NO SLIP				
0	2.64	0.6162	12760	71530	9545	4877	19.74	0.841
0.1	2.60	0.6239	12720	70830	9510	4868	19.70	0.827
0.2	2.52	0.6353	12740	68870	9408	4864	19.62	0.803
0.3	2.38	0.6545	12820	65680	9229	4683	19.46	0.761
				BODY AND SHOCK SLIP				
0	2.30	0.6458	2208	55050	8508	2000	24.97	0.621
0.1	2.61	0.5882	2208	56450	8636	2000	24.18	0.705
0.2	2.33	0.6824	2208	56000	8588	2000	23.87	0.628
0.3	2.07	0.7411	2208	54470	8428	2000	23.58	0.561
0.4	1.80	0.8150	2208	52520	8191	2000	23.06	0.485

Table 23. Downstream results (sphere cone, R_N = 0.2 m, T_w = 2,000 K): atmosphere - 98% N_2 + 2% CH_4, Trajectory VI, Z = 497.6 km, ϵ = 0.719.

S/R_N	$q_{c,w}$ (MW/m^2)	N_s (cm)	Enthalpy (kJ/kg) wall	Enthalpy (kJ/kg) shock	T_s (K)	T_w (K)	ρ_s/ρ_∞	St
				NO SLIP				
0	22.49	0.9386	2381	58330	10811	2151	15.93	0.0301
0.1	21.62	0.9616	2388	57720	10708	2152	15.98	0.0288
0.2	20.77	0.9793	2383	56200	10433	2149	16.09	0.0278
0.3	20.21	1.0060	2381	53580	9910	2150	16.40	0.0269
0.4	18.71	1.0430	2392	50250	9197	2152	16.89	0.0251
				BODY AND SHOCK SLIP				
0	22.32	0.9674	2177	58330	10812	2000	15.92	0.0298
0.1	21.84	0.9572	2177	57840	10728	2000	15.94	0.0291
0.2	20.93	0.9853	2177	56360	10462	2000	16.04	0.0279
0.3	20.04	1.0162	2177	53760	9946	2000	16.34	0.0267
0.4	18.86	1.0556	2177	50440	9236	2000	16.82	0.0251

Table 24. Downstream results (sphere cone, R_N = 0.2 m, T_w = 2,000 K): atmosphere - 98% N_2 + 2% CH_4, Trajectory VI, Z = 530.8 km, ϵ = 0.976.

S/R_N	$\dot{q}_{c,w}$ (MW/m^2)	N_s (cm)	Enthalpy (kJ/kg) wall	Enthalpy (kJ/kg) shock	T_s (K)	T_w (K)	ρ_s/ρ_∞	St
				NO SLIP				
0	3.10	0.5704	2240	71490	9032	2000	20.70	2.908
0.1	3.05	0.5755	2240	70760	9000	2000	20.67	2.859
0.2	2.97	0.5849	2240	68770	8909	2000	20.56	2.792
0.3	2.85	0.6004	2240	65590	8752	2000	20.37	2 675
0.4	2.67	0.6237	2240	61250	8508	2000	20.11	2.507
				BODY AND SHOCK SLIP				
0	2.19	0.5937	31590	71490	9032	5383	20.70	3.561
0.1	2.13	0.6007	31470	70770	9001	5373	20.67	3.448
0.2	1.98	0.6167	31360	68880	8914	5366	20.56	3.212
0.3	1.77	0.6435	31220	66060	8776	5344	20.40	2.855
0.4	1.49	0.6767	31000	62300	8571	5322	20.21	2.392